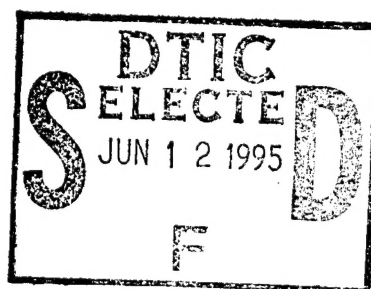


Stream Breakup by Waves

Dr. G. S. Samuelsen
Arash Ateshkadi

UCI Combustion Laboratory
Institute for Combustion and Propulsion
University of California
Irvine CA 92717

April 1995



*Original contains color
plates: All DTIC reproductions
will be in black and
white*

Final Report

APPROVED FOR PUBLIC RELEASE; DISTRIBUTION UNLIMITED.

19950607 046



PHILLIPS LABORATORY
Propulsion Directorate
AIR FORCE MATERIEL COMMAND
EDWARDS AIR FORCE BASE CA 93524-7001

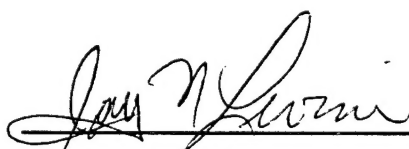
NOTICE

When U.S. Government drawings, specifications, or other data are used for any purpose other than a definitely related Government procurement operation, the fact that the Government may have formulated, furnished, or in any way supplied the said drawings, specifications, or other data, is not to be regarded by implication or otherwise, or in any way licensing the holder or any other person or corporation, or conveying any rights or permission to manufacture, use or sell any patented invention that may be related thereto.

FOREWORD

The work reported in this final report was performed by the UCI Combustion Laboratory, Institute of Combustion and Propulsion, University of California, Irvine, CA under contract with the OLAC PL/RKFE Branch at the Phillips Laboratory, Edwards AFB CA 93524-7680. OLAC PL Project Manager was Jay N. Levine.

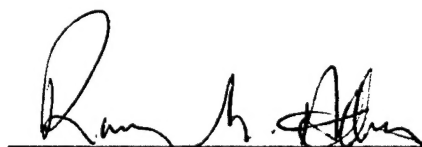
This report has been reviewed and is approved for release and distribution in accordance with the distribution statement on the cover and on the SF Form 298.



JAY N. LEVINE
Project Manager

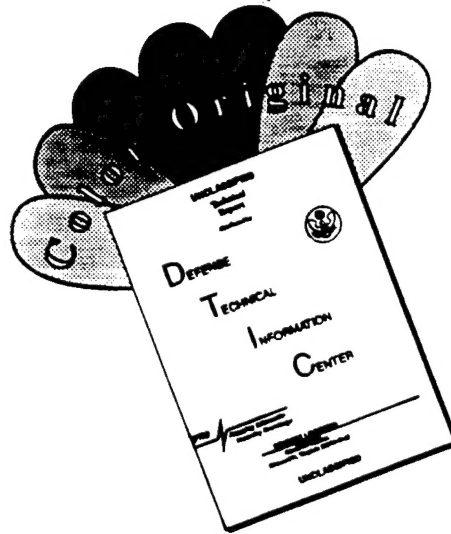


STEPHEN L. RODGERS
Acting Director,
Fundamental Technologies Division



RANNEY G. ADAMS
Public Affairs Director

DISCLAIMER NOTICE



THIS DOCUMENT IS BEST QUALITY AVAILABLE. THE COPY FURNISHED TO DTIC CONTAINED A SIGNIFICANT NUMBER OF COLOR PAGES WHICH DO NOT REPRODUCE LEGIBLY ON BLACK AND WHITE MICROFICHE.

REPORT DOCUMENTATION PAGE			Form Approved OMB No 0704-0188	
Public reporting burden for this collection of information is estimated to average 1 hour per response, including the time for reviewing instructions searching existing data sources gathering and maintaining the data needed, and completing and reviewing the collection of information. Send comments regarding this burden estimate or any other aspect of this collection of information, including suggestions for reducing this burden to Washington Headquarters Services, Directorate for Information Operations and Reports, 1215 Jefferson Davis Highway, Suite 1204, Arlington, VA 22202-4302, and to the Office of Management and Budget, Paperwork Reduction Project (0740-0188), Washington DC 20503.				
1. AGENCY USE ONLY (LEAVE BLANK)		2. REPORT DATE April 1995		3. REPORT TYPE AND DATES COVERED Final Report
4. TITLE AND SUBTITLE Stream Breakup By Waves			5. FUNDING NUMBERS C: F04611-91-K-0127 PE: 62302F PR: 3058 TA: 00CZ	
6. AUTHOR(S) Dr. G. S. Samuelson and A. Ateshkadi				
7. PERFORMING ORGANIZATION NAME(S) AND ADDRESS(ES) UCI Combustion Laboratory Institute for Combustion and Propulsion University of California Irvine CA 92717			8. PERFORMING ORGANIZATION REPORT NUMBER UCI-ARTR-93-2	
9. SPONSORING/MONITORING AGENCY NAME(S) AND ADDRESS(ES) Phillips Laboratory OLAC PL/RKFA 9 Antares Drive Edwards AFB CA 93524-7660			10. SPONSORING/MONITORING AGENCY REPORT NUMBER PL-TR-93-3028	
11. SUPPLEMENTARY NOTES COSATI CODE(S): 21/02				
12a. DISTRIBUTION/AVAILABILITY STATEMENT Approved for Public Release; Distribution is Unlimited			12b. DISTRIBUTION CODE A	
13. ABSTRACT (MAXIMUM 200 WORDS) <p>An imaging technique is used to investigate the fluid dynamics associated with the breakup of a liquid jet by a passing transverse shock wave. This mechanism is believed to be a potential source of combustion instability in liquid propellant rocket engines. Combustion instability is caused by the release of heat in phase with a passing pressure disturbance. The jet/wave interaction causes rapid stomization and propellant redistribution, and enhances mixing, vaporization, and reaction rates. Knowledge of the breakup process aids in prediction of local heat release with respect to the passing wave and provides insight on its viability as a potential instability mechanism.</p> <p>The present shock tube study applies high-speed, high-resolution photography to explore the jet/wave interaction that might be experienced in a large scale liquid oxygen/hydrogen (LOX/H₂) engine similar to the Space Shuttle Main Engine (SSME) or other such engines being considered for the next generation of launch systems. Fluid parameters deemed important were simulated as well as possible. Two types of wave induced breakup were examined: a constant velocity flow field (square wave) and an exponentially decaying velocity field (N-wave). Time-resolved images of the jet/wave interaction indicate very rapid and fine stomization within 500μs of impingement.</p> <p>Shock interaction with the primary stomization process produces a substantial change to the breakup mechanism and serves as a principal candidate for the promotion and acceleration of rocket engine instability. Results of the qualitative and quantitative study reveal that the step wave produces a longer duration tangential and normal stress on the liquid column as compared to the N-wave. As a result, N-waves decelerate jet displacement and extend the jet breakup time. A faster stomization rate and jet displacement occurs behind higher strength square waves impinging on smaller diameter jets. The average drop size formed in this stomization process decreases with air stream velocity and increases with jet diameter. Jet breakup occurs at the trough of surface waves on the liquid column, and the amplitude of the surface waves decreases with increasing liquid/gas momentum ratios.</p>				
14. SUBJECT TERMS Breakup; simulants; wave-perturbation; cinematography; primary atomization; combustion instability; shock tube			15. NUMBER OF PAGES 105	
			16. PRICE CODE .	
17. SECURITY CLASSIFICATION OF REPORT Unclassified	18. SECURITY CLASSIFICATION OF THIS PAGE Unclassified	19. SECURITY CLASSIFICATION OF ABSTRACT Unclassified	20. LIMITATION OF ABSTRACT SAR	

TABLE OF CONTENTS

1.0:	INTRODUCTION.....	1
1.1	Impetus.....	1
1.2	Goals and Objectives.....	1
2.0	BACKGROUND.....	2
2.1	Combustion Instability and Its Evolution.....	2
2.2	Prevention of Combustion Instability: The Motivation.....	3
2.3	Candidates for Instability Mechanisms.....	3
2.4	Primary Atomization.....	4
2.5	Jet Breakup and Penetration.....	4
2.6	Summary of Relevant Research.....	7
3.0	APPROACH.....	9
4.0	EXPERIMENT.....	10
4.1	Overview.....	10
4.2	Stream Injector.....	12
4.3	Liquid Simulant.....	12
4.4	Facility.....	15
4.5	Diagnostics.....	15
4.6	Data Acquisition System.....	18
4.7	Test Matrix.....	20
5.0	RESULTS.....	21
5.1	Overview.....	21
5.2	Square Wave Perturbation.....	27
5.2.1	Jet Displacement.....	27
5.2.2	Jet Breakup Time.....	28
5.3	N-Wave Perturbation.....	28
5.3.1	Jet Displacement.....	34
5.3.2	Ligament and Drop Formation.....	43
5.4	Parametric Studies.....	56
5.4.1	Effect of Shock Strength.....	56
5.4.2	Effect of Jet Diameter.....	62
5.5	Surface Wave Formation.....	62
6.0	SUMMARY, CONCLUSIONS, AND RECOMMENDATIONS.....	70
6.1	Summary.....	70
6.1.1	Square Wave Induced Breakup.....	71
6.1.2	N-Wave Induced Breakup.....	72
6.1.3	Drop Size Measurements.....	73
6.2	Conclusions.....	73
6.3	Recommendations for Future Work.....	73
7.0	References.....	75
	Appendix A: Test Matrix Calculations.....	76
	Appendix B: Jet Displacement Plots.....	83
	Appendix C: Weber and Reynolds Number Time History.....	88

List of Figures

Figure	
1	Pressure Coefficient Distribution Around a Solid Cylinder 5
2	Primary Mechanism of Liquid Jet Breakup 6
3	Pressure and Temperature as a Function of x 12
4	Shock Tube Set-Up..... 13
5	Typical Pressure vs. Time Profile..... 14
6	Flow Facility 16
7	Diagnostic Set-Up..... 17
8	Timing Sequence for High Speed Cinematography 19
9	Weber and Reynolds Number Distribution..... 24
10	Dynamic Pressure Ratio (q) vs. Viscosity Ratio Distribution..... 25
11	Jet breakup sequence for Test 6..... 29
12	Jet breakup sequence for Test 7..... 30
13	Jet breakup sequence for Test 8..... 31
14	Jet breakup sequence for Test 9..... 32
15	Dimensionless downstream displacement of a liquid jet under the influence of a square wave..... 33
16	Still Images of Different Stages of Jet Breakup for Test 1..... 35
17	Still Images of Different Stages of Jet Breakup for Test 2..... 37
18	Jet breakup sequence for Test 3..... 39
19	Jet breakup sequence for Test 4..... 40
20	Jet breakup sequence for Test 5..... 41
21	Dimensionless downstream displacement of a liquid jet under the influence of an N-wave..... 42
22	Pressure Time History for Test 3..... 44
23	Pressure Time History for Test 8..... 45
24	Dimensionless downstream displacement of a liquid jet for Test 3 and Test 8..... 46
25	Dimensionless downstream displacement of a liquid jet for Test 4 and Test 6..... 47
26	Pressure Time History for Test 4..... 48
27	Pressure Time History for Test 6..... 49
28	Pressure Time History for Test 5..... 50
29	Pressure Time History for Test 7..... 51
30	Dimensionless downstream displacement of a liquid jet for Test 5 and Test 7..... 52
31	Pressure Time History for Test 1..... 54
32	Pressure Time History for Test 2..... 55
33	Influence of Airstream Velocity Upon Spray Dropsize..... 57
34	Influence of Liquid Orifice Diameter Upon Spray Dropsize 57
35	Dimensionless downstream displacement of a liquid jet for Test 1 and Test 2..... 59
36	Pressure Time History for Test 4..... 60
37	Pressure Time History for Test 5..... 61
38	Dimensionless downstream displacement of a liquid jet for Test 4 and Test 5..... 63
39	Pressure Time History for Test 7..... 64
40	Dimensionless downstream displacement of a liquid jet for Test 4 and Test 7..... 65
41	Pressure Time History for Test 8..... 66

42	Pressure Time History for Test 9	67
43	Dimensionless downstream displacement of a liquid jet for Test 8 and Test 9.....	68
44	Dimensionless downstream displacement of a liquid jet for Test 3 and Test 4.....	69
45	Jet surface wave amplitude vs. liquid/gas dynamic pressure ratio	70
B.1	Dimensionless Downstream Displacement of a Liquid Jet for Test 1	83
B.2	Dimensionless Downstream Displacement of a Liquid Jet for Test 2	83
B.3	Dimensionless Downstream Displacement of a Liquid Jet for Test 3	84
B.4	Dimensionless Downstream Displacement of a Liquid Jet for Test 4	84
B.5	Dimensionless Downstream Displacement of a Liquid Jet for Test 5	85
B.6	Dimensionless Downstream Displacement of a Liquid Jet for Test 6	85
B.7	Dimensionless Downstream Displacement of a Liquid Jet for Test 7	86
B.8	Dimensionless Downstream Displacement of a Liquid Jet for Test 8	86
B.9	Dimensionless Downstream Displacement of a Liquid Jet for Test 9	87
C.1	Gaseous Weber and Reynolds Number Time History	89
C.2	Gaseous Weber and Reynolds Number Time History	90
C.3	Gaseous Weber and Reynolds Number Time History	91
C.4	Gaseous Weber and Reynolds Number Time History	92
C.5	Gaseous Weber and Reynolds Number Time History	93
C.6	Gaseous Weber and Reynolds Number Time History	94
C.7	Gaseous Weber and Reynolds Number Time History	95
C.8	Gaseous Weber and Reynolds Number Time History	96
C.9	Gaseous Weber and Reynolds Number Time History	97

Accession For	
NTIS CRA&I	<input checked="" type="checkbox"/>
DTIC TAB	<input type="checkbox"/>
Unannounced	<input type="checkbox"/>
Justification	
By	
Distribution /	
Availability Codes	
Dist	Avail and/or Special
A-1	

List of Tables

Table		
1	Subcritical Simulant Liquids.....	14
2	Supercritical Simulant Liquids.....	14
3	SSME LOX/H ₂ Injectable LOX - Combustion Products	22
4	Test Conditions and Summary of Jet Column Waves Data	26
5	Mean Measured Drop Diameters.....	56
A.1	Test Matrix Spreadsheet for Methanol	79
A.2	Methanol Test Matrix Spreadsheet for Variable Jet Diameters.....	80
A.3	Test Matrix Spreadsheet for Freon-22.....	81
A.4	Freon-22 Test Matrix Spreadsheet for Various Jet Diameters.....	82

Table of Symbols

English Symbols

a	Speed of sound
D	Jet diameter (m)
d_p	Drop diameter
q	Dynamic pressure ratio
L	Length of injection element
L_c	Liquid core length
M_s	Shock Mach number
P	Pressure (Psig)
R	Gas constant
R_o	Universal gas constant
Re_l	Liquid jet Reynolds number
S_w	Shock strength, p_2/p_1
t	time
T	Dimensionless breakup time
V	Flow Velocity (m/s)
We_g	Aerodynamic Weber number
x	Transverse distance from injector orifice
X	Dimensionless displacement from the injector

Greek Symbols

γ	Specific heat ratio
μ_l	Dynamic viscosity of liquid phase (kg/m s)
μ_g	Dynamic viscosity of gas phase (kg/m s)
ν_l	Kinematic viscosity of liquid phase (m ² /s)
ν_g	Kinematic viscosity of gas phase (m ² /s)
ρ_l	Density of liquid phase (kg/m ³)
ρ_g	Density of gas phase (kg/m ³)
σ	Surface tension (kg/s ²)

Subscripts

1	Shock tube driven section
2	Fluid properties behind the shock wave
4	Shock tube driver section
c	Gas chamber
g	Gas phase
j	Jet
l	Liquid phase
o	Initial condition

1.0 INTRODUCTION

1.1 Impetus

Combustion instability in liquid propellant rocket engines has historically been a major concern in engine development programs. Although the general aspects of the combustion process in liquid propellant rocket combustion chamber are known, knowledge of details (e.g., the rates of reactions or the mechanisms of unstable burning) is incomplete. Today combustion instability can occur and produce excessive vibration forces or heat transfer which will result in failure or corrosion of engine parts, respectively. The aim is to prevent occurrence of this instability and to maintain reliable operation. To meet this aim, knowledge of the details governing the fundamental processes is required.

1.2 Goals and Objectives

Five possible physical processes associated with combustion instability are: primary atomization, secondary atomization, vaporization, chemical kinetics, and mixing. Primary atomization was selected for the present study. Strong pressure/velocity disturbances have been shown to affect the atomization process by accelerating the rate of jet breakup, thereby changing the droplet size distribution and injector spray pattern. The altered propellant spray may vaporize at a different rate than in the undisturbed spray. Changes in droplet size, vaporization rate and propellant mixture distribution can lead to changes in spatial energy release rate. As a result, fundamental information is required regarding the breakup of liquid jets immediately behind a pressure wave.

The goal of this study was to provide insights associated with the initial breakup of a liquid stream (primary atomization) as a result of a propagating pulse. To meet this goal, the objectives of the study were to:

1. Modify an existing shock tube to meet the requirements of the present study.
2. Identify the test liquids and establish the test conditions that simulate engine operating conditions.
3. Conduct the experiments.
4. Analyze the results.

Highly time-resolved images were employed to delineate the breakup process. The results provide the understanding needed to facilitate the development of improved atomization models, and improved steady-state performance.

2.0 BACKGROUND

2.1 Combustion Instability and Its Evolution

Combustion in a liquid rocket engine is never perfectly smooth; some fluctuations of pressure, temperature, and velocity are always present. When these fluctuations interact with the natural frequencies of the propellant feed system or the chamber acoustics, periodic superimposed oscillations occur. In liquid rocket engines it is desirable to minimize the occurrence and magnitude of chamber pressure oscillations to avoid catastrophic damage and corrosion of the combustion chamber due to large amplitude pressure waves and excessive heat transfer rates, respectively.

Unstable combustion, *combustion instability*, displays organized oscillations occurring at well-defined intervals with a pressure peak that may be maintained, increase, or die out. The three principle types of combustion instability are described as follows: low frequency {chugging} or system instability (10-200 Hz); intermediate frequency {acoustical or buzzing} (200-1000 Hz); and high frequency {screaming, or screeching} (above 1000 Hz). High frequency is the most perplexing and most common in the development of new engines. Since energy content increases with frequency, this type is the most destructive, capable of rapidly destroying an engine.

High frequency instability occurs in at least two modes, *longitudinal* and *transverse*. The *longitudinal mode* propagates along axial planes of the combustion chamber and the pressure waves are reflected at the injector face and the converging nozzle cone. The *transverse modes* propagate along planes perpendicular to the chamber axis and can be broken down into *radial* and *tangential modes*. Transverse mode instability predominates in large liquid rockets, particularly in the vicinity of the injector. Thus it is one of the most important modes. Transverse modes often have a very nonlinear characteristic and are driven predominantly by combustion. Once triggered such instabilities can rapidly reach destructive amplitudes that result in heat-transfer rate increases of an order of magnitude, much as with detonation, causing metal melting and wall burn-throughs, on a millisecond time scale.

The stable combustion field in a liquid rocket engine consists of liquid streams impinging or shearing due to high speed co-flowing gas to form ligaments and blobs and finally into a dense cloud of droplets. All of this liquid burns on its surface at a rate controlled by its surface area and turbulent heat and mass transfer. When high frequency instability occurs the most dramatic change takes place in the poorly atomized and mixed region as envisioned by Levine (1965). The high transverse gas velocity shatters the liquid, and particle displacement causes gas-liquid mixing, both resulting in intense gas generation.

An understanding of the origins of combustion instability could ultimately permit the design of inherently stable, high performance liquid rocket engines and substantially reduce the costly trial-and-error development which is now necessary. Analysis of data

could assist investigators in developing analytical models which provide a good theoretical understanding of instability mechanisms and in improving rocket engine design methods and procedures. Thus, current instrumentation and diagnostic capabilities enable a new approach to the control of combustion instability: investigation and eventual control of the basic combustion instability mechanisms.

2.2 Prevention of Combustion Instability: The Motivation

Despite advances in understanding and modeling combustion instability processes, conducting stability rating programs, and designing injectors and combustion systems to avoid instability, unstable operation is still encountered. Combustion instability thus continues to be a concern, particularly now that a new round of liquid rocket engine development is imminent.

Current approaches for passive control of combustion instability rely on damping out pressure oscillations by the use of baffles, resonators, or acoustic liners. Active control of combustion instabilities involves the control of energy addition/extraction of combustion/flow processes. Advances in fast-response, nonintrusive instrumentation, measurement, and diagnostic techniques now make possible the investigation of many combustion processes which could participate in liquid rocket engine instability, and thereby (1) create the possibility of understanding the origins of combustion instability, and (2) permit ultimately the design of inherently stable, high performance liquid rocket engines.

2.3 Candidates for Instability Mechanisms

Continual effort over the past several decades has identified numerous candidates for instability mechanisms. A JANNAF sponsored workshop on Liquid Rocket Engine Combustion Driven Instability Mechanisms resulted in identification of key mechanisms and prioritization of research needs associated with these mechanisms. Five categories of basic combustion physics associated with combustion instabilities were identified (Jensen, 1989):

- Primary atomization
- Secondary atomization
- Vaporization
- Chemical kinetics
- Mixing

Of these five, the category assessed to have a great potential for participation in an instability, and therefore selected for investigation, is the effect of transverse mode instability on primary atomization of the liquid jet. The committee concluded that experimental studies of both atomization and spray characteristics in steady and simulated

instability conditions should be emphasized. Complementary cold-flow simulations along with limited combustion testing should be considered to facilitate extrapolation of models based on more extensive cold flow data. Objectives are detailed atomization rates and drop sizes and gas phase parameters to anchor mechanism models. Sub and supercritical conditions were also recommended for consideration. The subsequent discussion explains the selection of primary atomization.

Three fundamental multi-phase conditions exist within the combustion chamber: 1.) liquid core/ligament regime, 2.) dense spray regime, and 3.) dilute spray regime. There exists multiple-processes within each regime. Dominant processes vary from regime to regime and form distinct zones within each regime. The transient nature of the dispersed interfacial boundary between dense and dilute spray regimes is a critical factor in terms of flame-stabilization.

Each process has a characteristic time. Variation in pressure, temperature, and velocity will affect the atomization process and the characteristic times and rates associated with those processes. If one of the characteristic times is substantially longer than the others, that particular process can be rate-controlling. This can introduce dynamic or frequency-dependent behavior which will amplify the pressure and velocity waves to considerable strength. Since these pressure/velocity fluctuations have been shown to accelerate the breakup mechanism, the atomization process will tend to be a dynamic feedback behavior.

2.4 Primary Atomization

Primary atomization in a liquid rocket engine arises from the breakup of liquid jets or sheets, depending on the type of injection element employed. In this atomization mechanism initial separation of large drops and ligaments from the main body of the liquid occurs under very high inertial forces. At the high injection velocities used, Rayleigh breakup is not relevant, and the Kelvin-Helmholtz liquid instability is of greater interest. In this process, surface waves form and grow, causing distortion and eventual breakup of the fluid surface.

2.5 Jet Breakup and Penetration

In the breakup of a liquid jet, the jet is suddenly subjected to large aerodynamic forces that result in jet breakup. Investigations of liquid jet breakup by a shock wave have demonstrated that the jet is broken by the high velocity gas flow behind the shock front (Morrell, 1963). The flow behind the shock wave, moving transverse to the liquid jet, causes disintegration to occur simultaneously at all points along its length.

In the present study, the initial response of the liquid to the high speed gas flow occurs due to the external pressure distribution around the cylindrical liquid jet. The flow around the jet acts like flow around a solid cylinder. For example, Figure 1 illustrates the pressure coefficient distribution around a solid cylinder. A similar pressure distribution

creates an adverse pressure gradient within the liquid, resulting in flattening of the liquid jet transverse to the flow of gas. At the outer edges of this flattened sheet, drops and ligaments are torn off when the tangential shear stress overcomes the surface tension of the fluid. The rate of breakup is assumed to be controlled by the distortion rate of the liquid cross section. The model in Figure 2 illustrates the proposed primary mechanism of breakup of a liquid jet in a cross flow of gas. High viscosity may retard the distortion, but the controlling step should remain the same. In the present study, the time required for complete breakup to occur was judged visually from still frames and high speed photographs.

Experimental observations of jet behavior after shock passage have included the time t_j for the jet to shatter, its drag-induced displacement x from the initial location, the height h of jet penetration, and the coordinates x, y of the jet (Reinecke, 1977; Kush, and Schetz, 1972; Reichenback, and Horn, 1971). These quantities generally have been nondimensionalized by the diameter D_j and density ρ_j of the jet and by the air density ρ_g and speed V_g behind the shock wave resulting in the dimensionless quantity,

$$X = x / D_j \quad (2-1)$$

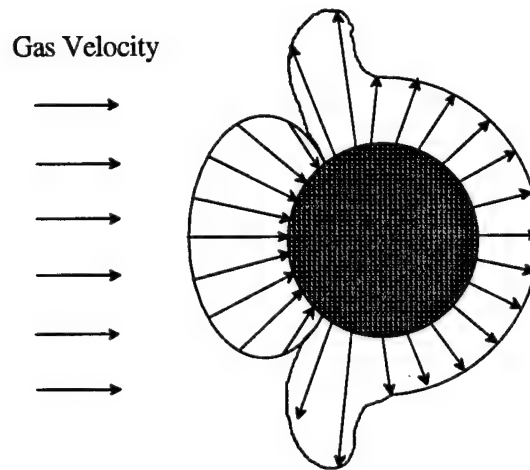


Figure 1. Pressure Coefficient Distribution Around a Solid Cylinder

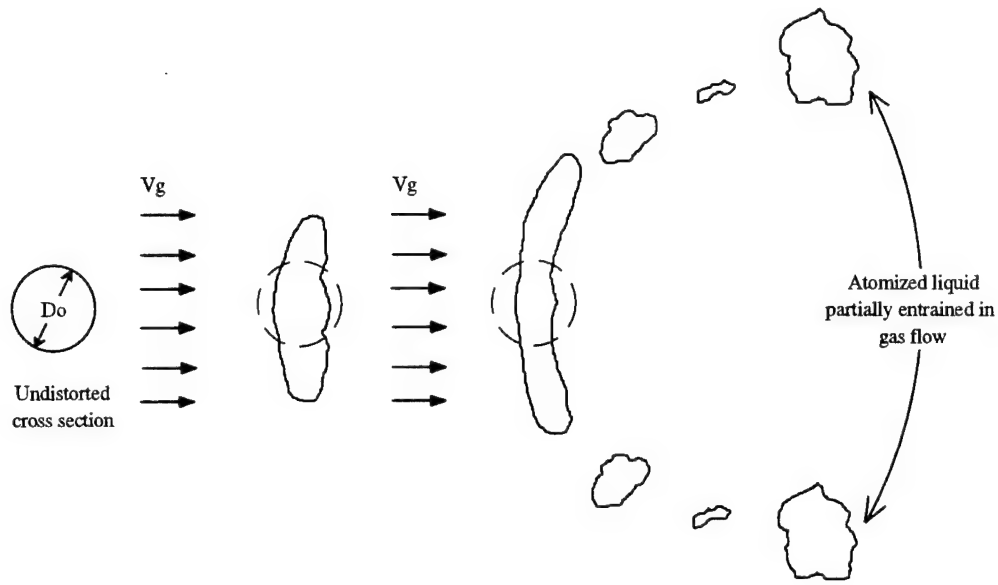


Figure 2. Primary Mechanism of Liquid Jet Breakup

The penetration commonly is nondimensionalized and correlates as (Reinecke, 1977):

$$\frac{hM}{D} = K \sqrt{\frac{p_j^0}{p}} \quad (2-2)$$

where D is the jet initial diameter, M and p are the freestream Mach number and static pressure, and p_j^0 is the jet plenum pressure. Since the liquid jet is usually underexpanded, Eq. (2-2) can also be written as:

$$h / D_j = K \sqrt{\frac{\gamma p_j V_j^2}{2 \rho_g V_g^2}} \quad (2-3)$$

where $\rho_j V_j^2$ and $\rho_g V_g^2$ are the jet and airstream dynamic pressure, respectively, and γ is the specific heat ratio of the air. Typical values for K are about 7.0 in experiments where the Weber number was generally above 500.

Assuming that the jet element moves normal to the air velocity at constant speed V_j , the distance h that the jet penetrates into the flow is the product of the time t_j required to shatter the jet element times the speed of the jet, that is $h=t_j V_j$. From this relation and from Equation (2-3), the dimensionless time for breakup is derived:

$$T_j = \frac{t_j V_g}{D_j} \sqrt{\frac{\rho_g}{\rho_j}} \quad (\text{for } \gamma=1.4, K=7.0) \quad (2-4)$$

The downstream displacement of the jet can also be calculated. Values of the downstream displacement of the jet element as a function of its time after injection y/V_j , where x and y are the coordinates of the jet, were determined from each frame captured at 33 μ s intervals. A plot of these data in the nondimensional form of $X = x/D_j$ as a function of $T = \frac{t V_g}{D_j} \sqrt{\frac{\rho_g}{\rho_j}}$ was generated to compare the results for correlation and agreement of the empirical coefficients.

2.6 Summary of Relevant Research

Combustion instability in liquid propellant rocket engines has historically been a major concern in engine development programs and was the subject of extensive research during the 60's and early 70's (Harrje and Reardon, 1972). Despite advances in modeling, stability rating techniques, stability aids, and injector design, unstable operation is still encountered. Combustion instability continues to be a concern, particularly now that a new round of liquid rocket engine development is imminent.

Current approaches for passive control of combustion instability rely on stability aids such as baffles and acoustic cavities, and injector design, although active control of combustion instabilities has also been recently proposed. This "band-aid" approach is necessitated by a lack of fundamental understanding of how combustion instabilities arise, grow, and sustain. An understanding of the origins of combustion instability could ultimately permit the design of inherently stable, high performance liquid rocket engines without much of the costly trial-and-error development which is now necessary.

Experimental analysis of basic instability mechanisms could assist investigators in developing analytical models to provide a good theoretical understanding of how these mechanisms cause instability and ultimately provide a design tool for improving rocket engine design. Recent advances in fast-response, non-intrusive diagnostic techniques now make possible the investigation of many combustion processes which could participate in liquid rocket engine combustion instability.

Over the past several decades candidates for instability mechanisms have been identified by researchers (primary atomization, secondary atomization, vaporization, chemical kinetics, and mixing). Of these five, secondary atomization is the subject of one Air Force program (Cox, 1990). The current effort, also Air Force sponsored, is designed to assess the effect of transverse mode instability on primary atomization of the liquid jet common to most rocket engine injection systems. The aforementioned JANNAF sponsored committee concluded that experimental studies of both atomization and spray characteristics in steady and simulated instability conditions should be emphasized and that complementary cold-flow simulations along with limited combustion testing should be

considered to facilitate extrapolation of models based on more extensive cold flow data. Targeted data included detailed atomization rates and drop sizes and gas phase parameters to anchor mechanism models.

In a liquid rocket engine, primary atomization is obtained by impinging liquid streams or shearing a liquid stream with a high speed co-flowing gas. In a transverse spinning mode instability, wave induced primary atomization of the propellant streams causes greatly increased generation of droplets and thus surface area available for vaporization. The convective flow associated with the wave passing enhances the evaporation rate, gas phase mixing, and reaction rates. Additionally, reduced penetration of the spray into the combustion chamber occurs, increasing the concentration of reactive components near the injector and increasing the energy release rate in that vicinity. If the expanding gases created during energy release increase the pressure amplitude of the passing wave or the amplitude of an ensuing wave and overcome damping processes, an instability can occur.

When high frequency instability occurs, the most dramatic change probably takes place in the poorly atomized and mixed region. As envisioned by Levine (1965), the high transverse gas velocity shatters the liquid, and particle displacement causes gas-liquid mixing, both resulting in intense gas generation. At low amplitudes these effects may damp as well as drive, but at high amplitude the net effect occurs at the proper phase relationship to sustain the high frequency instability.

Considerable attention has been given to the physical process of injection and its role in the control of the rate and/or completeness of combustion [Clark (1964); Heideman (1968); Buffam (1967); Huynh; (1992); Sitkei (1963)]. Most of the interest has been concentrated on the drop sizes produced by different types of injectors under various environmental conditions. Mass distribution and drop size measurements have been made for the breakup of fuel jets in a crosscurrent flow of gas (Clark, 1964). Others have studied the behavior of drops and sprays in the gas flow in a shock tube or blast gas or in different types of tunnels. An analysis of critical conditions for jet breakup indicates that there is a predictable velocity at which breakup commences and that this velocity is a function of the liquid dimensions and properties and the duration of the flow (Morrell, 1961). It appears that jet shattering may be a rate process that can account for the growth and propagation of a wave in a liquid-fuel combustion system that is vaporization limited. In oscillatory combustion, Clark (1960) identified a possible mechanism for amplifying the instability through the increase in energy release rate caused by more rapid atomization in the wake of the pressure wave.

Missing are high-resolution, high-speed photography to delineate the processes associated with the breakup of a liquid stream by a transverse shock wave. Previous images of jet breakup in a crossflow have been limited to low time resolutions on the order of milliseconds. However, the different regimes the jet undergoes before complete breakup occur much before 1 millisecond in high speed gas flows. In the present study, a

cylindrical liquid jet formed by a simple orifice acted upon by a transverse shock wave was investigated experimentally by capturing images at a 33 μ s time interval.

In past studies, the liquid jet was subjected to a constant gas flow velocity. Based on the literature review, no studies have been conducted to study the behavior of a liquid jet in an exponentially decaying velocity field (N-wave). The behavior of drops have been studied in an accelerating and decelerating flowfield, and it was shown that drops do respond to the deceleration forces. It was with this intent that the behavior of liquid jet in such an environment was studied.

In addition, past experiments which utilized photographic images to delineate the atomization were limited to large liquid to gas momentum ratios ($q > 1$). And it was shown that the jet first deforms before any breakup occurs. However, this behavior was only studied at high momentum ratios. In this study, the simulation of a liquid rocket engine operating condition was of paramount concern. In order to do so, low value of momentum ratios had to be obtained ($q \ll 1$) to accurately delineate the breakup process.

Insight into this mechanism is sought to assess its potential for causing combustion instability in a liquid rocket engine. Atomization and breakup rate for any point in the jet can be calculated from the experimental data.

3.0 APPROACH

Task 1. Preparation of Hardware to Simulate Transverse Wave

This task addresses the modification of an existing shock tube to allow the presentation of a liquid jet. The shock tube should repeatably produce a pressure pulse of the correct amplitude, duration, and character. In addition, the shock tube should include: (1) a pressurized injector housing to deliver the liquid simulant into the bore of the shock tube at both atmospheric and high pressure conditions, (2) a fluid delivery system consisting of a pulsation- and vibration-free pressure feed system for atmospheric test section conditions, and a gear-pump feed system for high pressure experiments, and (3) stream injectors to deliver a laminar liquid jet column into the shock tube. Finally a selection of proper liquid simulants of liquid oxygen (LOX) is required to establish of test conditions that simulate rocket engine jet breakup. Surface tension and viscosity properties of the simulants need to be matched with LOX properties in order to simulate the breakup phenomena as well as possible.

Task 2. Development of Diagnostics and Data Acquisition System

In order to investigate the shock-induced stream breakup, a fast-response imaging and diagnostic technique must be developed. High speed shadowgraph images (30,000 frames/sec) of the transient behavior of the liquid jet are required using a high intensity, short duration, back-light source. Pressure transducers are needed upstream of the liquid

jet to sense the approaching shock and initiate the cinematography sequence via a microprocessor controller.

A data acquisition system is also required to acquire, display, analyze, and store data from the pressure transducers signals. The resulting pressure plot histogram is needed to calculate many of the gas phase properties (i.e., velocity, density, temperature, and viscosity). This information can then be used to determine instantaneous values of nondimensional parameters that are deemed important in the breakup process.

Task 3. Development and Implementation of a Test Matrix

Experimental modeling of the atomization process inside a high pressure liquid rocket combustion chamber requires the matching of certain fluid properties and dimensionless parameters deemed important in this atomization process of the liquid oxygen. A test matrix is needed to identify initial shock tube and stream injector conditions, for a particular liquid simulant, that simultaneously matches most of the atomization parameters in a particular liquid rocket engine. The engine chosen to be studied is the LOX/H₂ Space Shuttle Main Engine (SSME).

Task 4. Data Analysis

The breakup mechanism and wave interaction must be analyzed and qualitative and quantitative data analysis employed in the investigation of liquid jet breakup. Captured images, for example, can provide information on distortion of the liquid round jet, the formation of axial surface waves, jet displacement, drop size, etc. Qualitative analysis consists of studying this general behavior of the jet at various operating conditions. Quantitative analysis consists of measurements extracted directly from the photographs and/or from digitally scanned images.

4.0 EXPERIMENT

4.1 Overview

To investigate the stream breakup a planar pressure wave was passed transversely through a round liquid jet. A shock tube was the vehicle used to simulate the passage of a transverse instability wave. The plane shock wave was produced by the sudden bursting of a diaphragm which separates a gas at high pressure from one at lower pressures. After the bursting of the diaphragm, a compression wave forms in the low-pressure gas, this rapidly steepening to form a shock front. At the same time a series of expansion waves propagate in the high-pressure gas. Curves of p versus x and T versus x shortly after rupture of the diaphragm are shown in Figure 3 (John, 1984).

The bursting of the diaphragm generates a shock wave, which propagates into the expansion chamber, and an expansion wave, which propagates into the compression

chamber, as shown in Figure 3. The condition of the fluid which is traversed by the shock is denoted by (2), and that of the fluid traversed by the expansion wave is denoted by (3). The interface between regions 2 and 3 is called the *contact surface*. It marks the boundary between the fluids which were initially on either side of the diaphragm. On either side of the contact surface, the temperatures, T_2 and T_3 , may be different (only if conduction is neglected), but it is necessary that the pressure and fluid velocity be the same, that is, $p_2 = p_3$. Therefore, the contact surface travels with the speed of the gas flow behind the shock. During the time that the images were captured (1 msec after the passage of the shock) the contact surface did not have enough time to reach the test section for the gas density variation to be an issue. In addition, the driven section following the test section was sufficiently long to not allow the reflected shock to reach the test section during the cinematography.

A double diaphragm high-pressure shock tube was used to provide the pulse required to perturb a liquid jet and induce the primary atomization instability mechanism (Figure 4). The shock tube is square in cross-section (2" x 2") and capable of holding pressures to 1000 psia in the driven section and 3000 psia in the driver section. The double diaphragm technique for pulse generation can repeatedly provide on-demand, individual pulses of the correct character, duration, and amplitude.

Three different driver section configurations were used. For generating step waves a 36" cylindrical driver was used. For generating N-waves, a conical driver section was used.

The technique used to produce N-waves is based on the spherical-balloon problem (Temkin, 1982). Here a pressurized, spherical region is allowed to expand suddenly. As was found (Lamb, 1925), the expansion produces an N-wave. By analogy, a long cone with a pressurized region near the vertex can also be used to produce such waves. For this reason a conical driver section was selected, while the driven section was of constant cross-sectional area. A 36" and an 11" conical driver section were used to produce two different gas flow duration. The 36" conical driver produced a wave 5.5 msec in duration, whereas the 11" driver produced a 2.5 msec wave duration. These times closely correspond to the acoustic limit $t_s = 2x_0/a$ where x_0 is the length of the pressurized cone, and a is the speed of sound in the low-pressure region.

Figures 5a and 5b show a typical pressure-amplitude-versus-time record for a step wave and an N-wave, respectively, obtained with the facility.

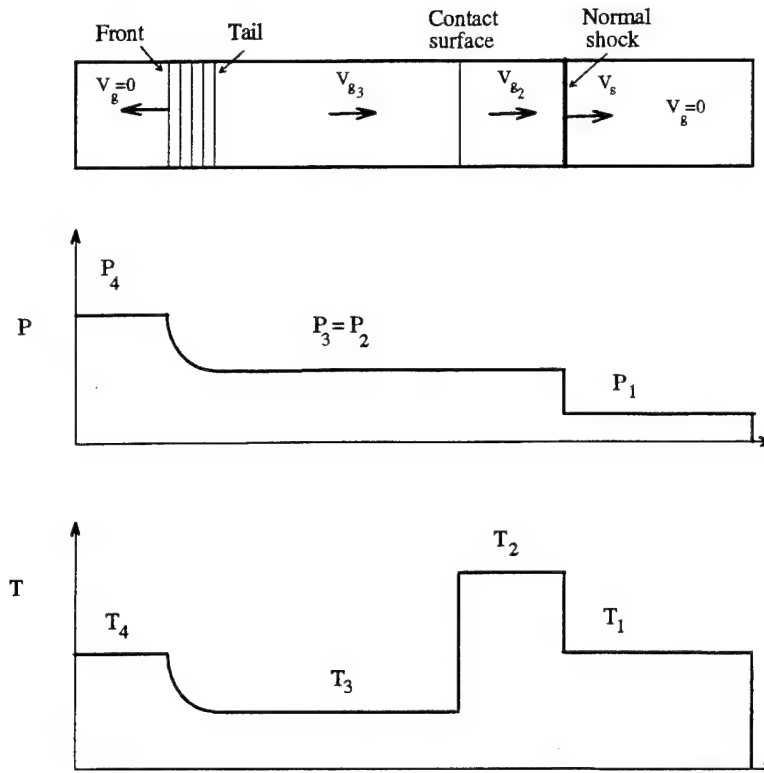


Figure 3. Pressure and Temperature as a Function of x

4.2 Stream Injector

The liquid is injected into the bore of the shock tube via a pressure feed or a pump system. This system of fluid delivery is pulsation and vibration free. A hypodermic needle and precision-hole stainless steel tubing were used as an injector orifice. Higher pressure testing requires the use of a gear pump to feed the liquid into the shock tube. The injector is placed inside a high pressure housing with an internal traverse system to vary the penetration length viewed from the side optical access.

4.3 Liquid Simulant

Most important to the establishment of the subcritical test conditions is the selection of the proper liquid simulants (Table 1). Since viscosity and surface tension need to be matched with the LOX properties, these are the variables which require the most scrutiny. Methanol was used for preliminary chamber checkout tests. Freon-22 was chosen as the simulant of choice for subcritical tests. For supercritical testing Freon 116 and Freon 503 have been identified to be the simulants of choice due to their low critical temperature and pressure (Table 2).

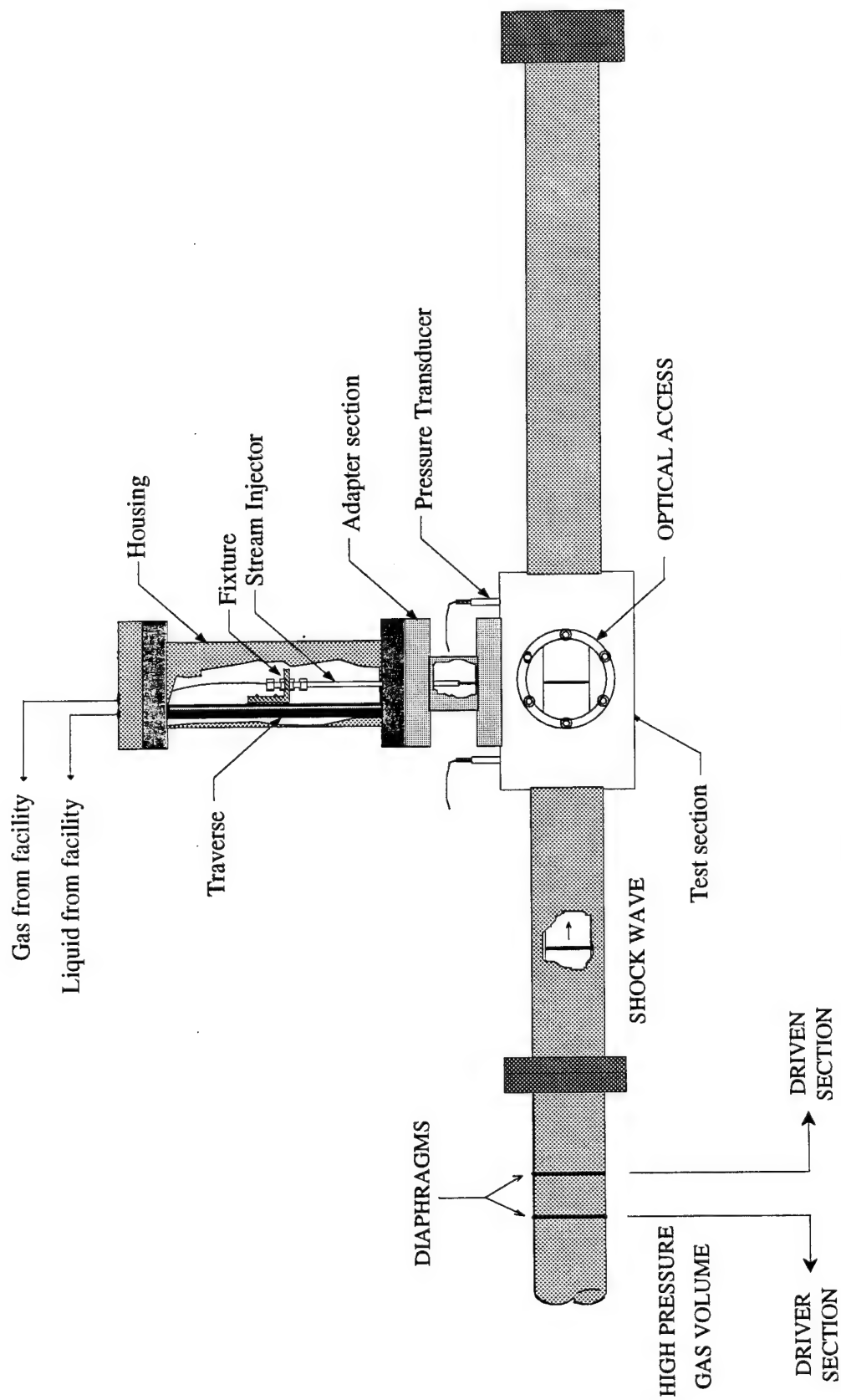


Figure 4. Shock Tube Set-Up

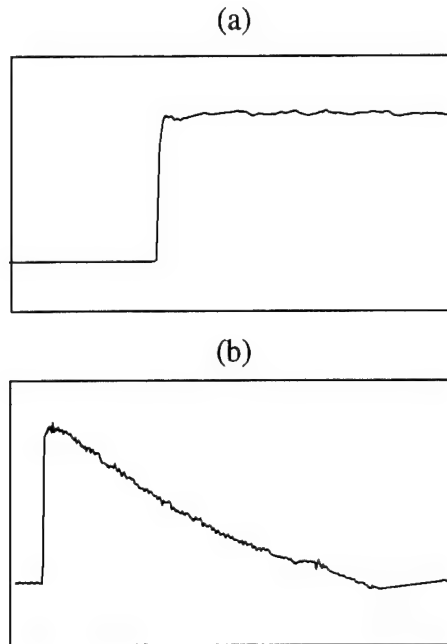


Figure 5. Typical Pressure-versus-Time profile (a) Step wave, (b) N-wave

Table 1. Subcritical Simulant Liquids

Liquid	ρ (kg/m ³)	σ (kg/s ²)	$\mu \times 10^4$ (kg/m.s)
Freon - 22 @ 25°C	1194	0.008	1.98
Methanol @ 25°C 1atm	791	0.0226	5.62
Water @ 5°C 1 atm	1000	0.0731	9.67
LOX @ 170°R	1153	0.0121	2.20

Table 2. Supercritical Simulant Liquids

Fluid	T _{cr} (°F)	P _{cr} (PSIA)	ρ - kg/m ³	σ - (kg/s ²)	$\mu \times 10^4$ - kg/ms
Freon 116	68	432	1587 @ -73°C	0.016 @ -73°C	3.00 @ -25°C
Freon 503	67	632	1223 @ -30°C	0.0061 @ -30°C	1.44 @ -30°C
LOX @ 170°R	-183	732	1153	0.0121	2.20

4.4 Facility

A schematic of the flow facility is shown in Figure 6. A control panel meters the flow into the shock tube via series of regulators and solenoid valves. The firing sequence of the shock wave is as follows. Solenoid valves S1, S2, S3 are opened and S4 closed. Volumes V1, V2, and V3 are filled to the desired pressure of V3. S3 is closed and V1, and V2 are filled up to the desired pressure of V2. S2 is then closed and V1 is filled to the desired pressure in the driver section and then S1 is closed. To initiate the shock S4 solenoid is opened to exhaust the gas in the intermediate section (V2) into the driven section (V3). This causes a high enough pressure differential across the first and the subsequent diaphragm to cause bursting. This method of shock initiation produces an on-demand repeatable shock wave of correct character, duration, and amplitude.

4.5 Diagnostics

In order to investigate the shock-induced stream breakup, a fast-response imaging and diagnostic technique has been utilized to investigate the fluid mechanics associated with the combustion processes which could participate in the evolution and development of combustion instability. Figure 7 illustrates the diagnostic set-up. A planar pressure wave passes transversely through a liquid round jet. Two high-frequency piezoelectric pressure transducers are positioned on either side of the injection port on the test section. These miniature dynamic transducers are specifically designed for shock tube measurements where very high frequency response is required. A digital delay / pulse generator (Stanford Research Systems Model DG535) was used to issue burst signals to the laser for still image photography and high speed cinematography.

High Speed Camera

Screening tests were conducted using a 35 mm Pentax camera to capture still images of jet breakup at different time intervals. Each image in the breakup sequence is a result of different tests conducted under the same shock tube condition. Results of pressure plots indicate very good shock repeatability to within 0.1 psi. High speed images of the transient breakup were captured with a Cordin (Model 321) rotating drum camera. The drum camera operates by the principle of a rotating drum with a 1 m length 35 mm film on the track. A camera controller is utilized to supply the proper current load to the drum motor. The drum can rotate at a maximum rate of 300 revolutions/sec (rps). As the film rotates with the drum the shutter is opened when the shock is initiated, thus allowing pulsating light to be directed through the camera optics onto the film. Each pulse of light will direct a discrete image on the film. An Infinity Model K2 long distance microscope was used to resolve the breakup phenomena accurately.

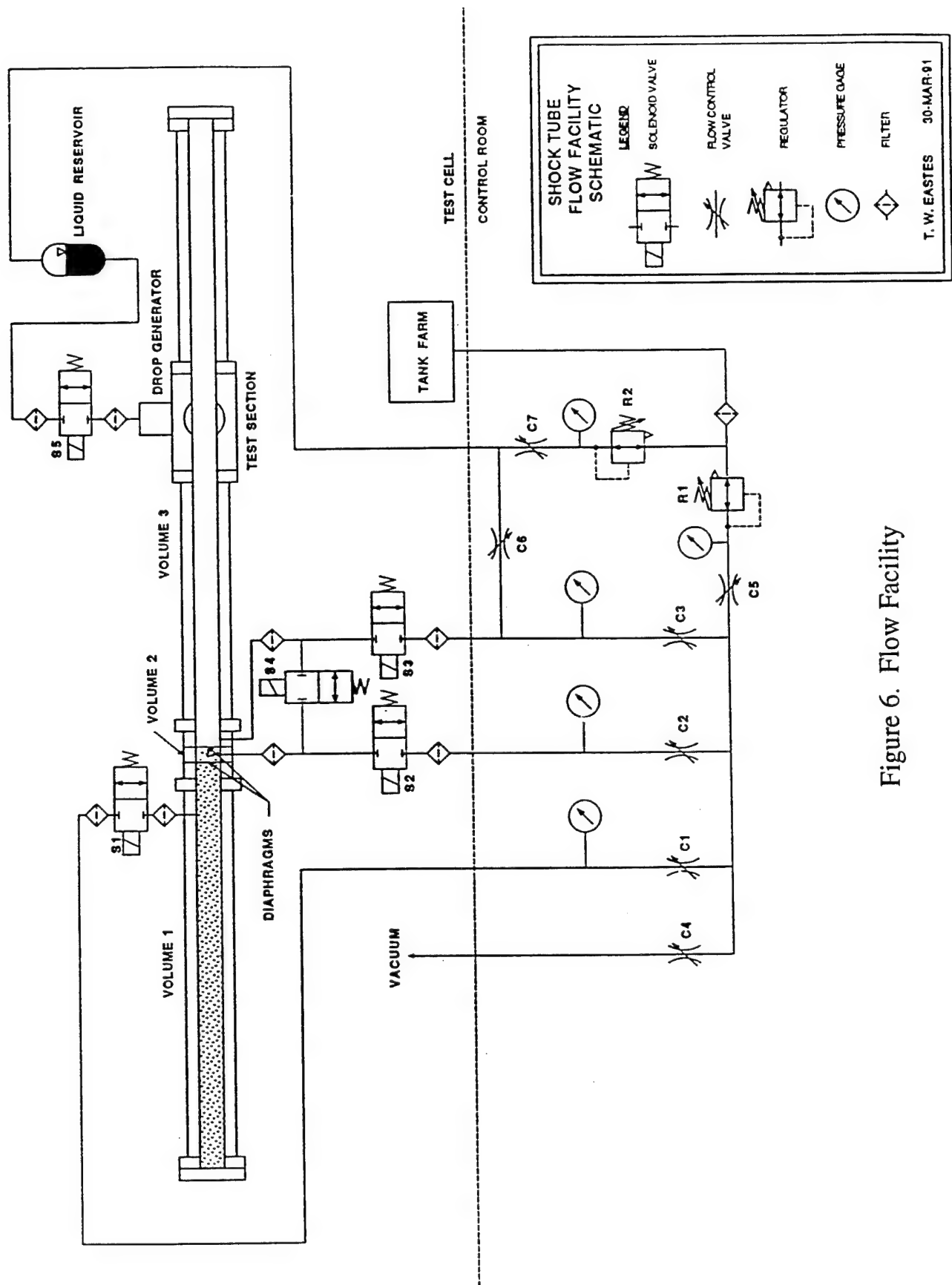


Figure 6. Flow Facility

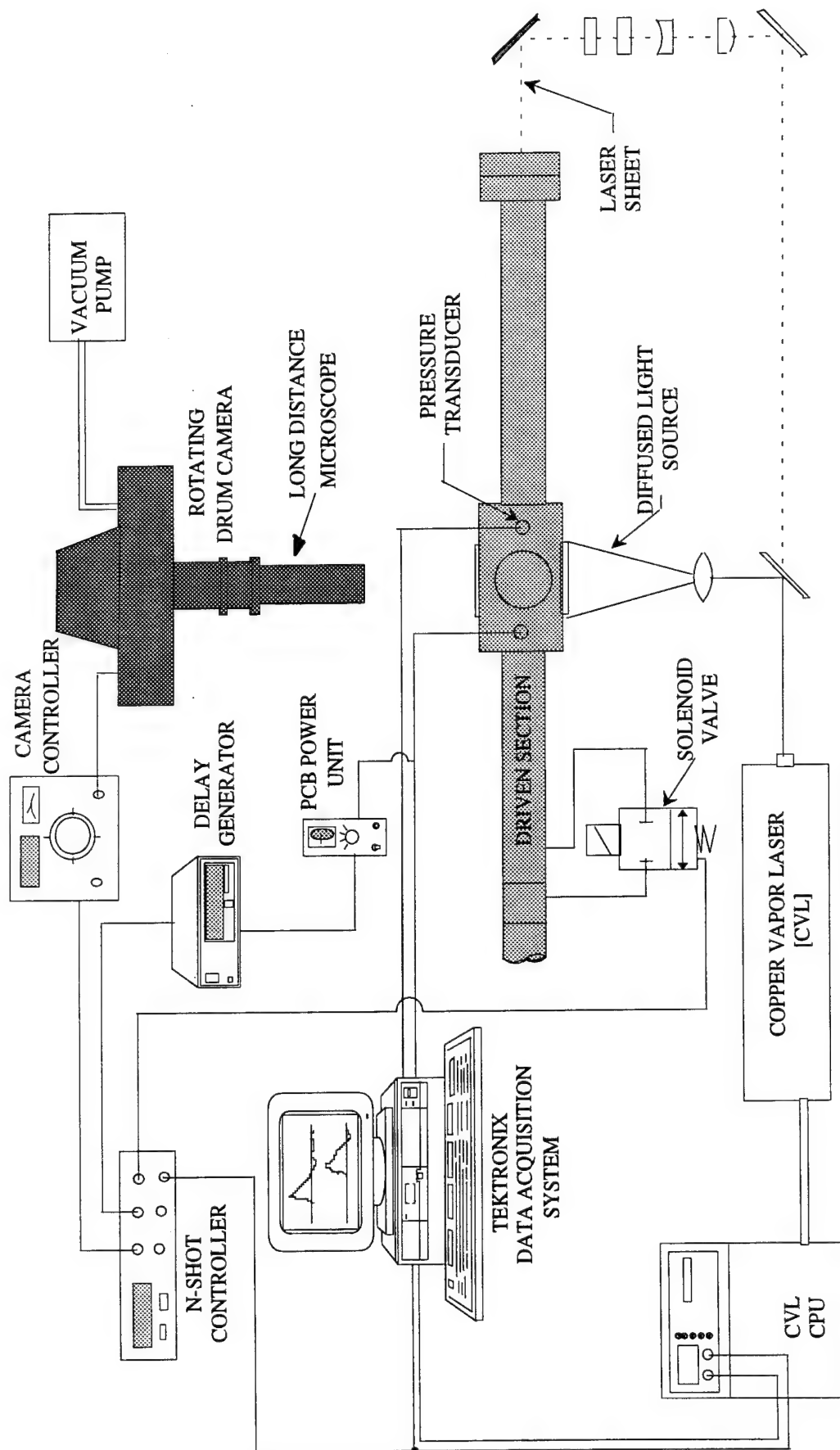


Figure 7. Diagnostic Set-Up

Copper Vapor Laser

The Copper Vapor Laser (CVL) high intensity visible light source offers many benefits in high speed liquid breakup visualization. The ultra short pulse width (20 ns) freezes the wave induced motion of the liquid jet. In the screening experiments the CVL was in the 'single' mode operation for still image photography. In high speed cinematography the "Multishot" operation was selected (30 kHz) and was synchronized to the Cordin camera via an 'n'-shot controller. The controller is a microprocessor based device which allows the laser to be operated in burst mode. The controller operates the laser at a free run frequency. The CVL is then switched off momentarily at which point a burst of 'n' pulses at a set burst frequency are fired. After a second time delay the controller continues to operate the laser at the free run frequency. A shadowgraph technique was implemented for capturing the images. The camera was positioned in front of the side viewport optic with the laser penetrating through the two test section viewports backlighting the liquid jet. The timing sequence is illustrated in Figure 8. The trigger signal from the shock-initiating solenoid valve initiates a sequence of events. The solenoid signal is sent to the 'n' shot controller where a signal is issued to the camera shutter, allowing it to open. At this time, a signal is also issued to the laser, turning it off momentarily, to prevent film exposure during the opening of the shutter. After the shock wave has propagated downstream, it triggers the first pressure transducer. The signal is sent to a delay generator where after a set delay, a TTL signal is sent to the laser signaling it to issue a burst of 'n' pulses. Each pulse places a discrete image onto the image plane. After the bursts are complete, the shutter is signaled to close. And after a set time delay, the laser reverts back to its normal free run frequency.

A Kodak EktaPro EM Motion Analyzer System (Model 1012) was also used with room light to capture high speed video images of the jet breakup as viewed from the side and end viewport.

4.6 Data Acquisition System

The TestLab multi-channel waveform analyzer (Model 2500) was used to acquire, display, analyze, and store data from the pressure transducers and the burst mode of the CVL. The TestLab provides spreadsheet-style management and set ups of data files which are transferable to an IBM PC. The transient pressure plots are plotted and are used to calculate the time variant gas flow velocity, We_g & Re_g , liquid/gas dynamic pressure ratio, and viscosity ratio. A photodiode is utilized to acquire signals from the laser pulses to coordinate the time each image was captured with its instantaneous pressure. This format of data translation is implemented to illustrate in each image, the instantaneous values of the parameters deemed important in the breakup process.

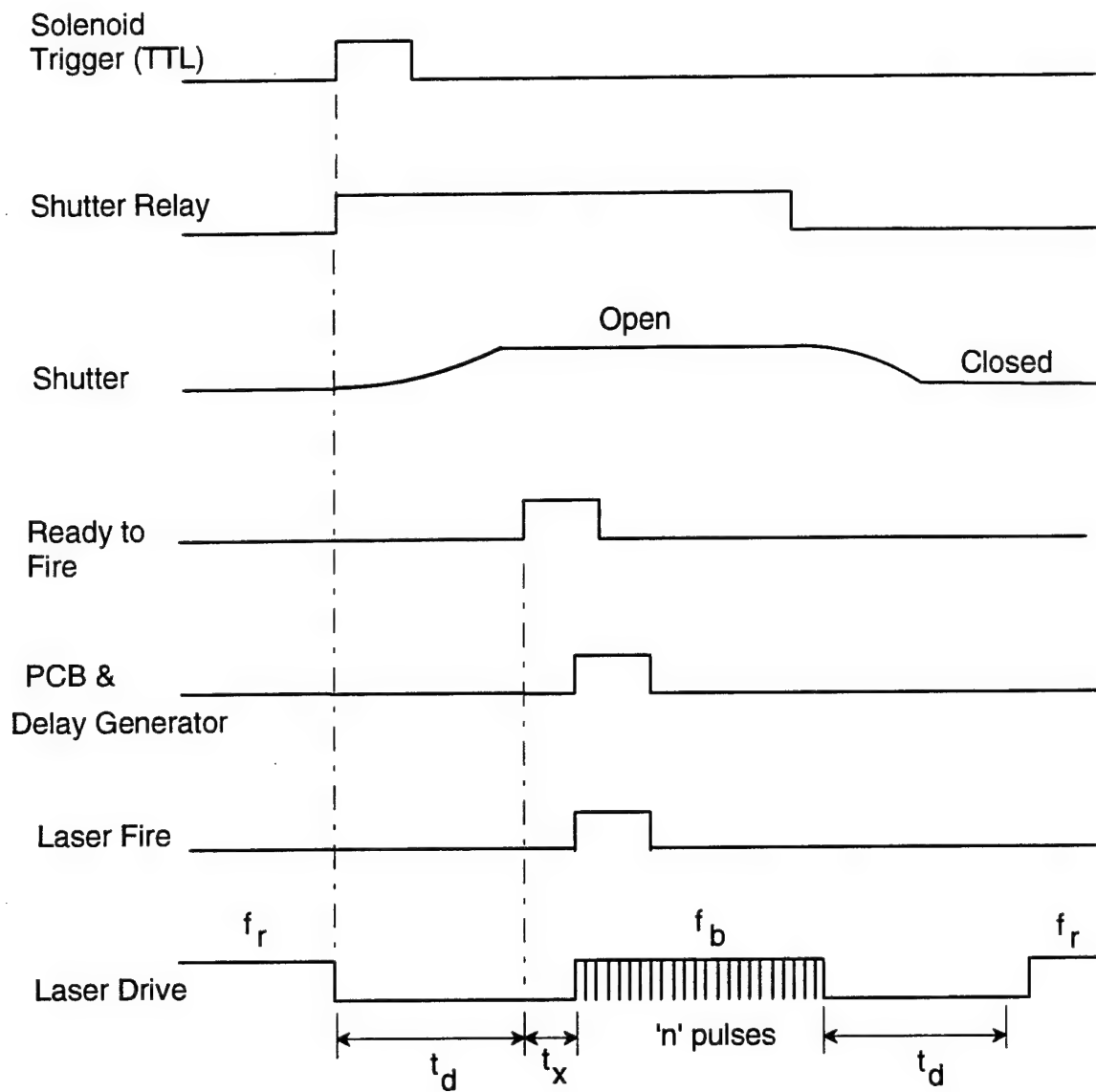


Figure 8. Timing Sequence for High Speed Cinematography

4.7 Test Matrix

Experimental modeling of the atomization process inside a high pressure liquid rocket combustion chamber is difficult due to the extreme temperature and turbulent conditions which exist. Under noncombustion conditions the best an experiment can do is match certain fluid properties and dimensionless parameters deemed important in the atomization process. For the simulant liquid study, the following parameters are chosen based on their importance and their ability to match hot-fire conditions:

1. Liquid surface tension (σ)
2. Liquid viscosity (ν_l)
3. Liquid to chamber-gas density ratio (ρ_l/ρ_{cg})
4. Aerodynamic Weber number ($\rho_g D V_g^2 / \sigma$)
5. Gaseous Reynolds number ($\rho_g D V_g / \mu_g$)
6. Liquid to gas dynamic pressure ratio ($\rho_l V_l^2 / \rho_g V_g^2$)
7. Liquid to gas kinematic viscosity ratio (ν_l / ν_g)
8. Liquid jet diameter (D)

A test matrix was developed to identify shock tube/injector operating conditions which simultaneously match most, if not all, of these parameters in the liquid rocket engine under study.

The liquid rocket engine (LRE) being simulated is the liquid oxygen/hydrogen (LOX/H₂) Space Shuttle Main Engine (SSME) with injectable LOX and the combustion products as the primary fluids. Table 3 lists fluid properties and dimensionless parameters present in this engine. The expected chamber properties have been defined so that proper cold flow studies are conceived. The cold flow properties are set up such that the injected conditions and the chamber conditions are chosen to match the parameters of the combustion products in the SSME as well as possible. To effectively do so, a certain range of shock strengths have initially been assumed. With this information all relevant gas properties have been obtained by using standard shock tube relations (Appendix A). For each liquid simulant its associated liquid properties (e.g. surface tension and viscosity) have been used to determine We_g , Re_g , liquid/gas viscosity, density, and dynamic pressure ratio for each shock tube condition. The parameter values obtained are then compared to the ones present in the engine under study. The parameter values in range of those found in the LOX/H₂ engine are then selected along with its associated initial gas pressure of the driver and the driven section. Thus, denoting operating conditions which will match the aforementioned parameters in this LOX/H₂ engine. Details of the test matrix calculations are included in Appendix A. Various wave strength and duration, jet velocity and diameter, and LOX simulants have been used in the delineation of the breakup mechanism at subcritical conditions.

A cylindrical driver section was used to produce a step wave of long gas flow duration, such that the pressure behind the wave was relatively constant until the reflected shock obstructed the flow. Thus, the liquid jet underwent positive acceleration

during the time that the images were taken. In addition, images of jet breakup undergoing both positive and negative accelerations were also taken. This type of motion is accomplished by exposing the liquid jet to N-waves (Temkin, 1982). In these, the fluid velocity decreases from some value immediately behind the leading shock, to a value of similar magnitude, but having the opposite direction, immediately ahead of the trailing the shock. Thus, owing to the passage of the wave, the liquid jet will first experience large positive accelerations which impart to the jet a velocity in the direction of the flow, producing initially a decrease of the relative fluid velocity. However, owing to the deceleration of the fluid velocity in the wave, the relative velocity will eventually increase in time.

5.0 RESULTS

5.1 Overview

Previous studies of jet breakup in a crossflow have been limited to low time resolution images on the order of milliseconds. Missing are the details of the breakup process, in general, and the incipient processes in particular. In addition, studies have not been conducted that study the breakup of a liquid jet in an exponentially decaying velocity crossflow (N-wave). In past studies, breakup has been addressed only in a constant gas velocity flow (step wave). Finally, in past experiments where photographic images of the atomization process have been taken, only large liquid to gas momentum ratios ($q > 1$) have been addressed. In this study, the simulation of a liquid rocket engine operating condition was of paramount concern. In order to do so, low value of momentum ratios were obtained ($q \ll 1$). This section presents the results of a qualitative and quantitative study that addressed the effect of shock wave type and strength, and jet diameter on jet breakup. Shadowgraph images of 33 microsecond (μs) time resolution and 20 nanosecond (ns) exposure time were acquired and used to obtain the necessary information.

A test matrix was developed and used to establish operating conditions that best match the parameters deemed important in the breakup process present in the SSME. In a liquid rocket engine, very high Weber and Reynolds numbers are present due to the highly turbulent flow conditions and the fluid properties of the liquid oxidizer (low surface tension). In the experiments conducted in the laboratory, very high speed gas flow velocities were difficult to obtain due to hardware limitations. In addition, low surface tension simulants were found to be challenging in their storage and their injection into the shock tube test section. As a result, the operating conditions selected encompassed a range of Weber and Reynolds numbers that is lower than the SSME value, but within one order of magnitude.

Table - 3 SSME LOX/H2 Injectable LOX - Combustion Products

LIQUID OXYGEN (LOX) PROPERTIES	
Injection velocity (m/s)	29.47
Injector diameter (mm)	4.78
Density (kg/m ³)	1153
Surface tension (kg/s ²)	0.0121
Dynamic viscosity (kg/ms)	0.00022
Injection Temperature (K)	111
GAS PROPERTIES	
Gas	Combustion Products
Shock strength	1.1 - 2.0
Gas flow velocity (m/s)	133 - 1000
Chamber density (kg/m ³)	14.7
Dynamic viscosity (kg/m s)	6.4×10^{-5}
Specific heat ratio	1.1481
Temperature (K)	1940
Molecular weight	13.589
Speed of sound (m/s)	1595.6
Density behind shock (kg/m ³)	16 - 26.75
Shock Mach number	1.05 - 1.40
FLUID PROPERTIES	
Liquid Reynolds number	7.383×10^5
Gaseous Reynolds number ($\rho_g DV_g / \mu_g$)	$1.16 \times 10^5 - 1.46 \times 10^6$
Aerodynamic Weber number ($\rho_g DV_g^2 / \sigma$)	$5.96 \times 10^4 - 5.64 \times 10^6$
Liquid/chamber gas density ratio ($\rho_l / \rho_{c,g}$)	78.44
Ohnesorge number ($\mu_l / (\rho_l D_i \sigma)^{1/2}$)	8.519×10^{-4}
Liquid/gas viscosity ratio	3.4375
Liquid/gas dynamic pressure ratio ($\rho_l V_l^2 / \rho_g V_g^2$)	0.07 - 6.64
Liquid/gas kinematic viscosity ratio (ν_l / ν_g)	0.0476 - 0.0797

Figure 9 is a summary of the maximum Weber - Reynolds number plot for all of the conditions tested. The Weber - Reynolds number time history for each individual test is illustrated in Appendix C. Figure 10 illustrates the minimum dynamic pressure ratio and maximum viscosity ratio distribution for the experiments. The shaded box denotes the range of those values present in the SSME. The liquid/gas dynamic pressure ratio obtained from these experiments ranged from the SSME value to one order of magnitude less. However, in all of the experiments conducted, the liquid/gas kinematic viscosity ratio was always within the range present in the SSME. A summary of the test conditions is presented in the Table 4.

Instantaneous pressure measurements were collected and used to determine properties of the gas flow, such as, velocity, density, and temperature dependent-viscosity. Values for the aforementioned parameters, for example, were calculated using the pressure plot from the pressure transducer upstream of the liquid injector. These values were obtained from normal-shock relations. The dynamic viscosity of the gas was calculated from temperature variations across the shock. From this the following dimensionless parameters were calculated:

$$\text{Weber Number:} \quad We = \frac{\rho_g V_g^2 D_j}{\sigma} \quad (5-1)$$

$$\text{Reynolds Number:} \quad Re = \frac{\rho_g V_g D_j}{\mu_g} \quad (5-2)$$

$$\text{Liquid/Gas Dynamic Pressure Ratio:} \quad \bar{q} = \frac{\rho_l V_l^2}{\rho_g V_g^2} \quad (5-3)$$

$$\text{Liquid/Gas Kinematic Viscosity Ratio:} \quad VR = \frac{\mu_l \rho_g}{\mu_g \rho_l} \quad (5-4)$$

The Weber number characterizes the surface-tension effect. It is the ratio of the dynamic force of the gas to the surface-tension of the liquid. The Reynolds number is the ratio of the inertial force to the viscous forces of the gas. An important parameter related to the behavior of the jet column is the dynamic pressure ratio which is simply the momentum flux ratios between the two fluids. Finally, the viscosity ratio, describes the viscous diffusivity between the two fluids, and is composed entirely of fluid properties, not geometric or flow parameters. The ratios are dimensionless fluid properties which give a measure of relative rate of diffusion.

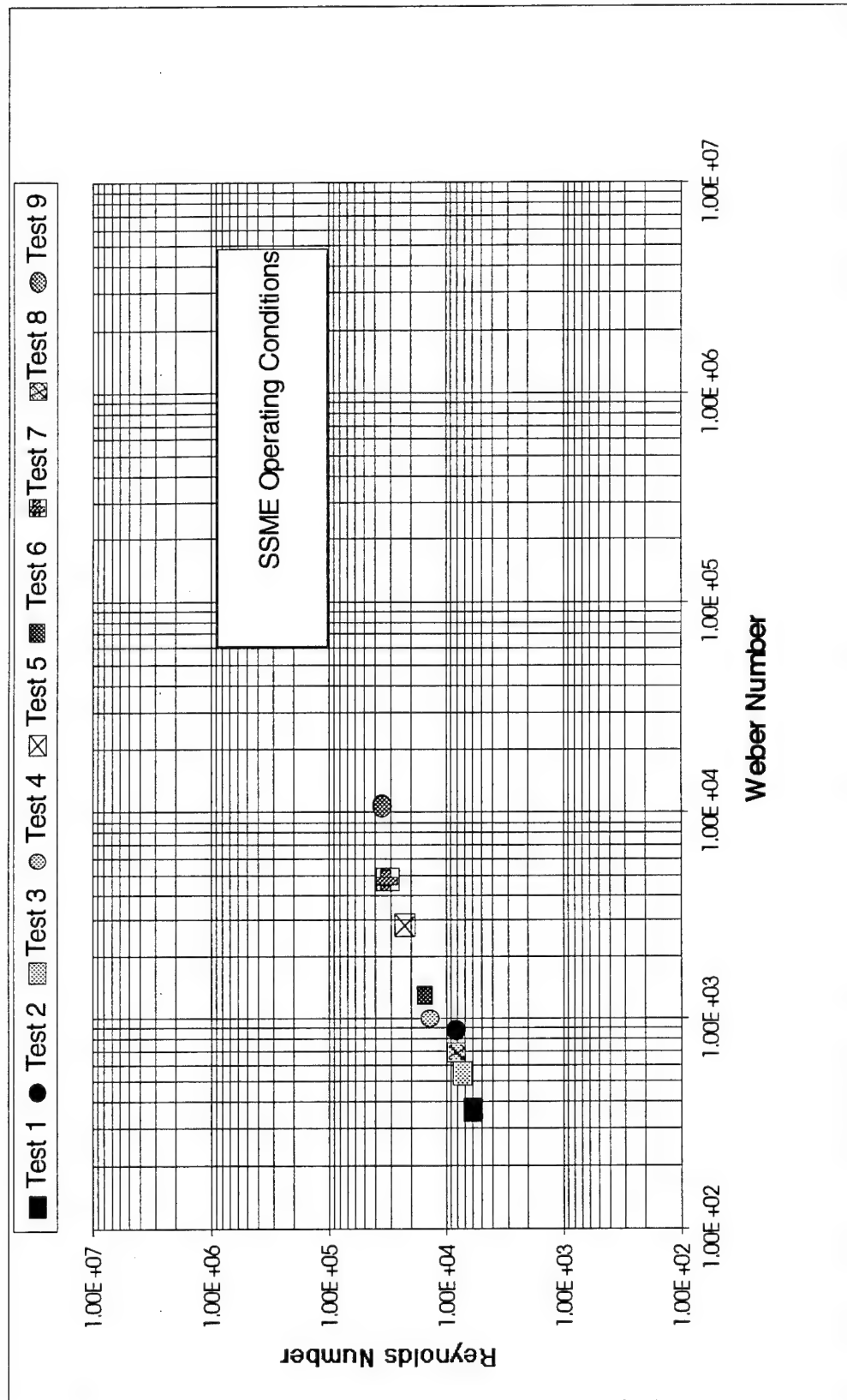


Figure 9. Weber and Reynolds Number Distribution

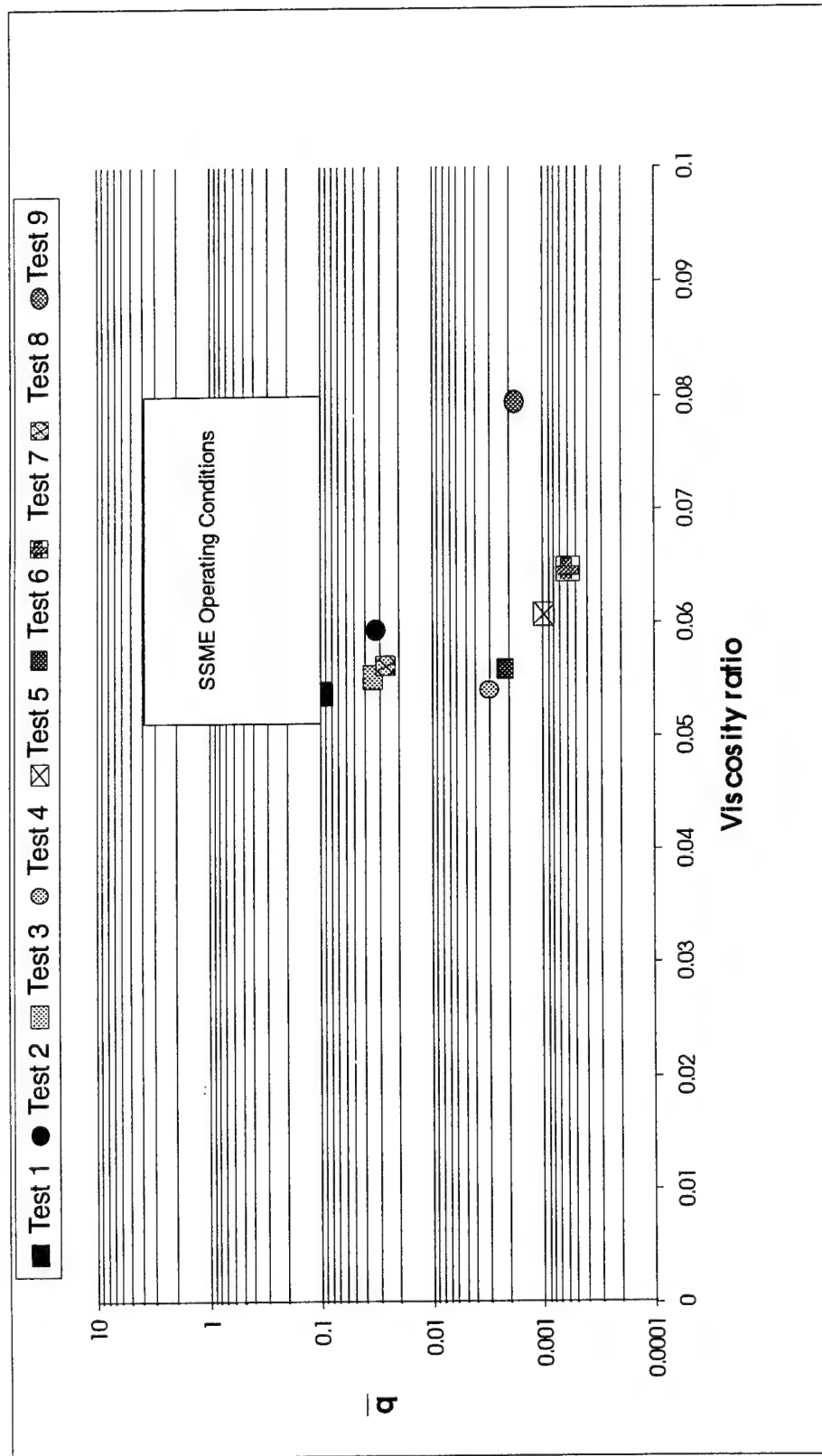


Figure 10. Dynamic Pressure Ratio (q) vs Viscosity Ratio Distribution

Table 4. Test Conditions and Summary of Jet Column Waves Data

Test Conditions: Liquid simulant - Methanol; temperature of simulant - room temperature										
Test Number	1	2	3	4	5	6	7	8	9	SSME Condition
Shock Wave Type	N	N	N	N	N	Step	Step	Step	Step	N
Shock Strength	1.33	1.56	1.39	1.37	1.63	1.43	1.81	1.44	2.64	1.1 - 2.0
Gas Flow Duration(ms)	5.5	5.5	2.3	2.3	2.3	∞	∞	∞	∞	1.0 - 5.0
Jet Diameter (mm)	0.8	1.0	1.04	1.41	1.41	1.41	1.41	1.04	1.04	4.78
Jet Velocity (m/s)	1.0	1.0	0.71	0.435	0.435	0.435	0.435	0.71	0.71	29.47
Gas Velocity (m/s)	75.78	122.0	88.74	84.60	135.11	96.93	168	98.95	300.30	133 - 1000
Shock Veloc. (m/s)	395	427	403	401	437	409	462	410	570	
Aero. Weber ^a	371	871	549	669	1950	907	3290	701	10400	59600 - 564000
Gaseous Reynolds ^a	5710	8100	7200	9160	16200	11000	21500	8150	35100	116000 - 1460000
Ohnesorge Number	0.0047	0.0042	0.00412	0.00354	0.00354	0.00354	0.00354	0.00412	0.00412	0.000852
Dyn. Pres. Ratio ^b	0.094	0.032	0.033	0.003	0.001	0.002	0.00284	0.0262	0.0017	0.07 - 6.64
Kin. Viscos. Ratio ^a	0.054	0.059	0.055	0.055	0.061	0.056	0.065	0.056	0.079	0.0476 - 0.0797
Wavelength (mm)			0.5	0.45	0.25	0.5	0.25	0.25	0.20	
Wave Speed (m/s)			1.9	1.9	5.0	1.0	3.0	4.15	3.79	
Wave Amp (mm)			0.35	0.2	0.3	0.2	0.8	1.15	0.25	

^a Maximum dimensionless value observed ^b Minimum dimensionless value observed

The behavior of the jet was examined under low liquid to gas momentum flows in both a constant and an exponentially decaying flow field. Highly time resolved images of the primary breakup of a liquid jet were obtained to provide information regarding the different regimes a jet undergoes before breakup. In addition, still images were obtained in Tests 1 and 2 and used to obtain drop size measurements. The rotating drum camera was used for Tests 3 - 9. The time duration between each frame was 33 μ s with an exposure time of 20 nanoseconds. Qualitative and quantitative data analyses were employed to investigate the following characteristics of the breakup:

- Distortion of liquid cylinder
- Jet displacement
- Ligament and drop formation
- Stripping of small drops
- Surface wave formation
- Spreading angle
- Jet breakup time
- Droplet size and mass distribution

The results are presented in the following sequence:

- Shock wave type (Square or N-wave)
- Shock strength (from 34% to 254%)
- Jet diameter (0.8 mm to 1.41 mm)
- Surface wave formation

5.2 Square Wave Perturbation

The square wave produced a relatively constant pressure. As a result, a relatively constant gas velocity was realized during the time frame in which the images were captured. Figures 11-14 illustrate the jet breakup sequence for square wave Tests 6-9, respectively. The results reveal that ligament formation occurs only after that jet has distorted to an elliptical shape. As the jet continues to deform, a liquid sheet is stripped away from the outer edge of the liquid core. Only after the jet is completely flattened to a liquid sheet does displacement from the injector occur. At high Weber numbers, this observation can be modified. Here, surface waves are formed along the sheet plane which induce more breakup further downstream. During the entire ligament/sheet formation process, drops are stripped away and are entrained in the gas flow. Average size of drops are 30 - 50 μ m.

5.2.1 Jet Displacement

A plot of the data obtained from experiments with a square wave in the nondimensional form of $X = x/D_j$ as a function of $T = \frac{t V_g}{D_j} \sqrt{\frac{\rho_g}{\rho_j}}$ is shown in Figure 15.

Experiments with square waves have a constant gas flow velocity immediately behind the

shock front. The displacement is a result of a normal stress acting on the jet column caused by the pressure drop immediately behind the wave. The values of the downstream displacement of the jet element as a function of its time after injection y/U_j , where x and y are the coordinates of the jet measured from the orifice parallel and normal to the freestream velocity, respectively, are discussed and compared with N-wave experiments in Section 5.3.1.

5.2.2 Jet Breakup Time

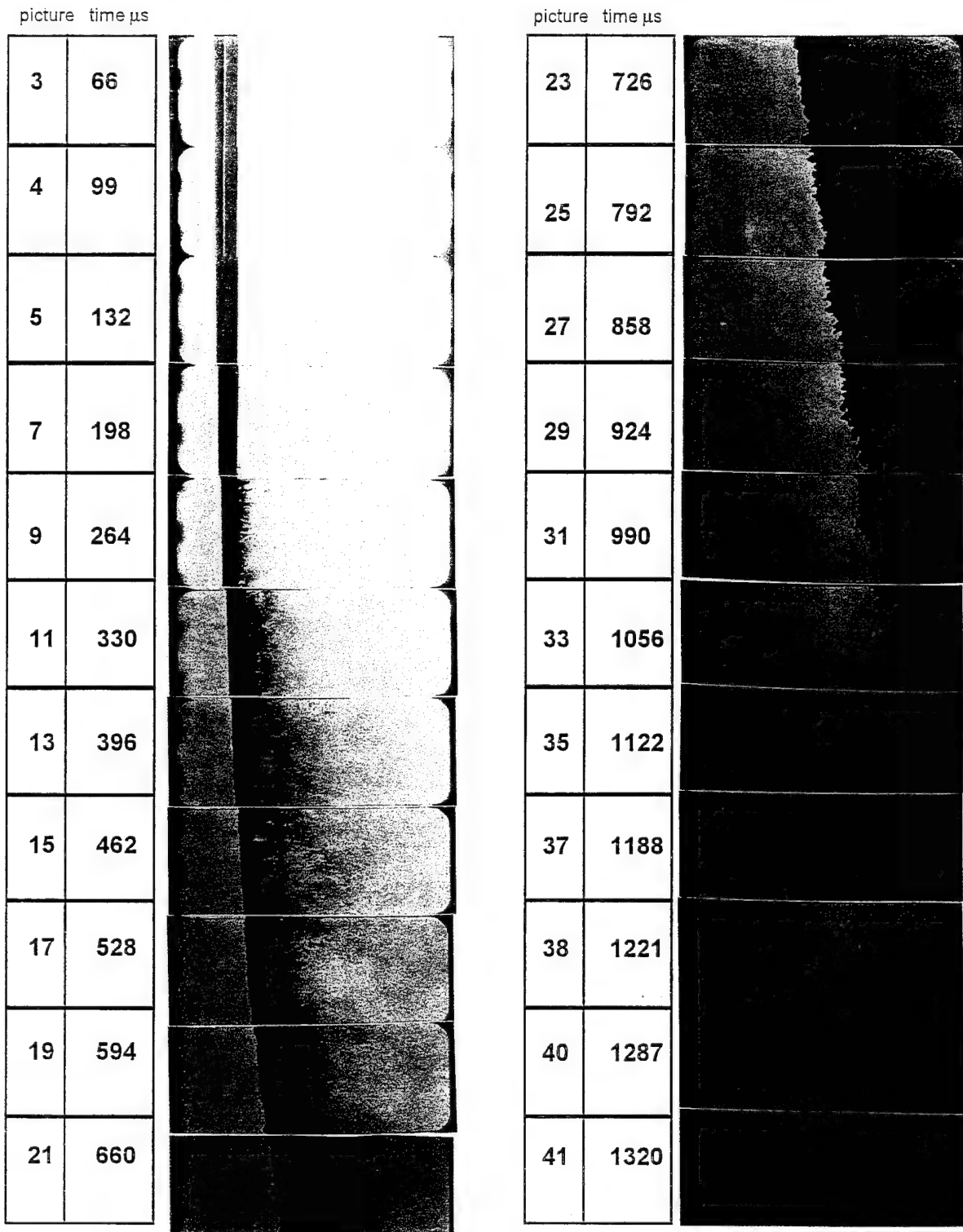
The dimensionless time for jet breakup was derived in Section 2.5 (Reinecke, 1978). The value of K was evaluated for experiments with Weber number over 600 and constant gas flow velocity. The value of K is derived from knowledge of gas flow velocity and density, time for jet shattering, and liquid jet diameter and density. The value of K could not be evaluated for experiments with a decaying gas flow velocity (N-waves), because K is no longer a constant. For the square-wave experiments the following observations were made:

Test	K	T _j	Weber Number
6	9.22	7.72	907
7	5.023	4.20	3290
8	4.50	3.76	701
9	7.035	5.89	10400

The average value of K and T_j were 6.44 and 5.40, respectively. Results from experiments conducted by Reinecke (1978) were similar ($K = 7.0$ and $T_j = 5.85$).

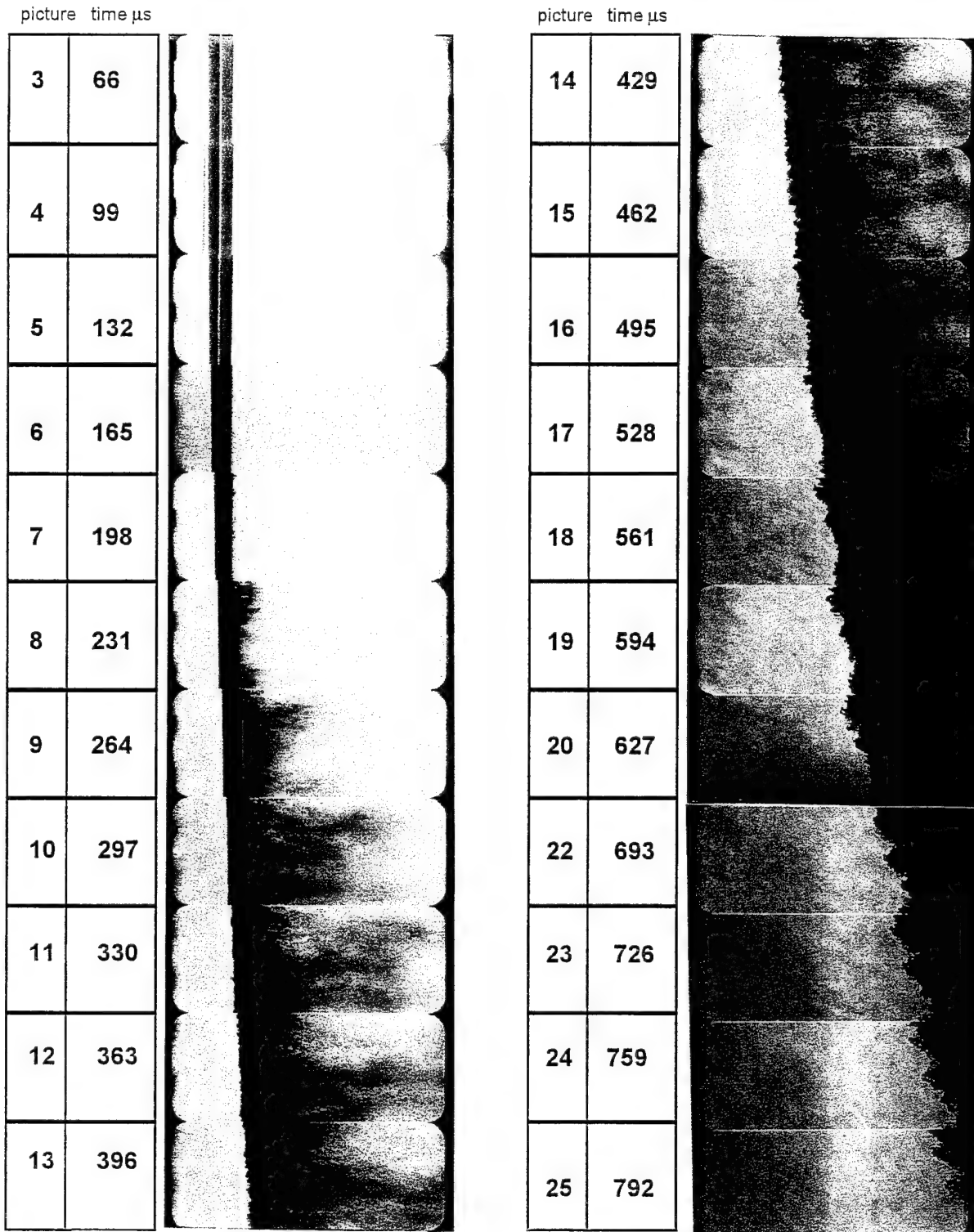
5.3 N-Wave Perturbation

A series of experiments were conducted using a conical driver section to produce a steep-fronted N-wave which was found to best represent an actual instability wave in a liquid rocket engine. A 36" long driver section was used to produce a 5.5 ms wave duration. A 10" driver was used to generate a 2.3 msec wave duration. For these experiments, a smaller mid-diaphragm holder had to be fabricated to enable the shock initiation. The conical driver section volume was considerably smaller compared with the cylindrical driver section. This reduced volume had no effect in rupturing the second diaphragm when the driver gas was exhausted into the intermediate section due to the reduction of pressure. Thus, a smaller mid-diaphragm holder increased the stored pressure and built a higher pressure differential across the second diaphragm causing it to burst.



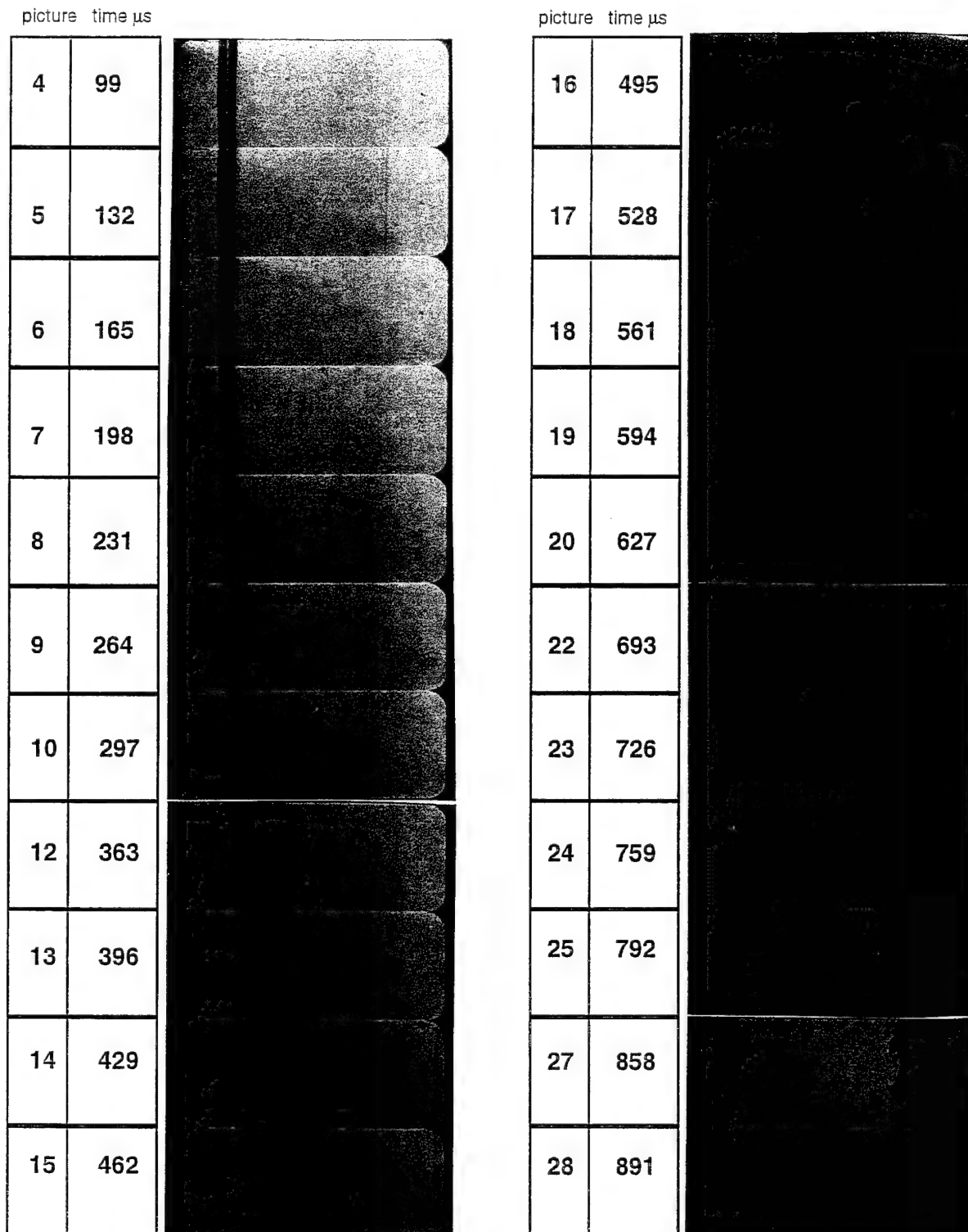
Wave Type	Shock Strength	Wave duration (ms)	D_i (mm)	V_g (m/s)	We_g	q	Re_g	v_l/v_z
Step	1.43	∞	1.41	96.93	907	0.002	11000	0.056

Figure 11. Jet breakup sequence for Test 6



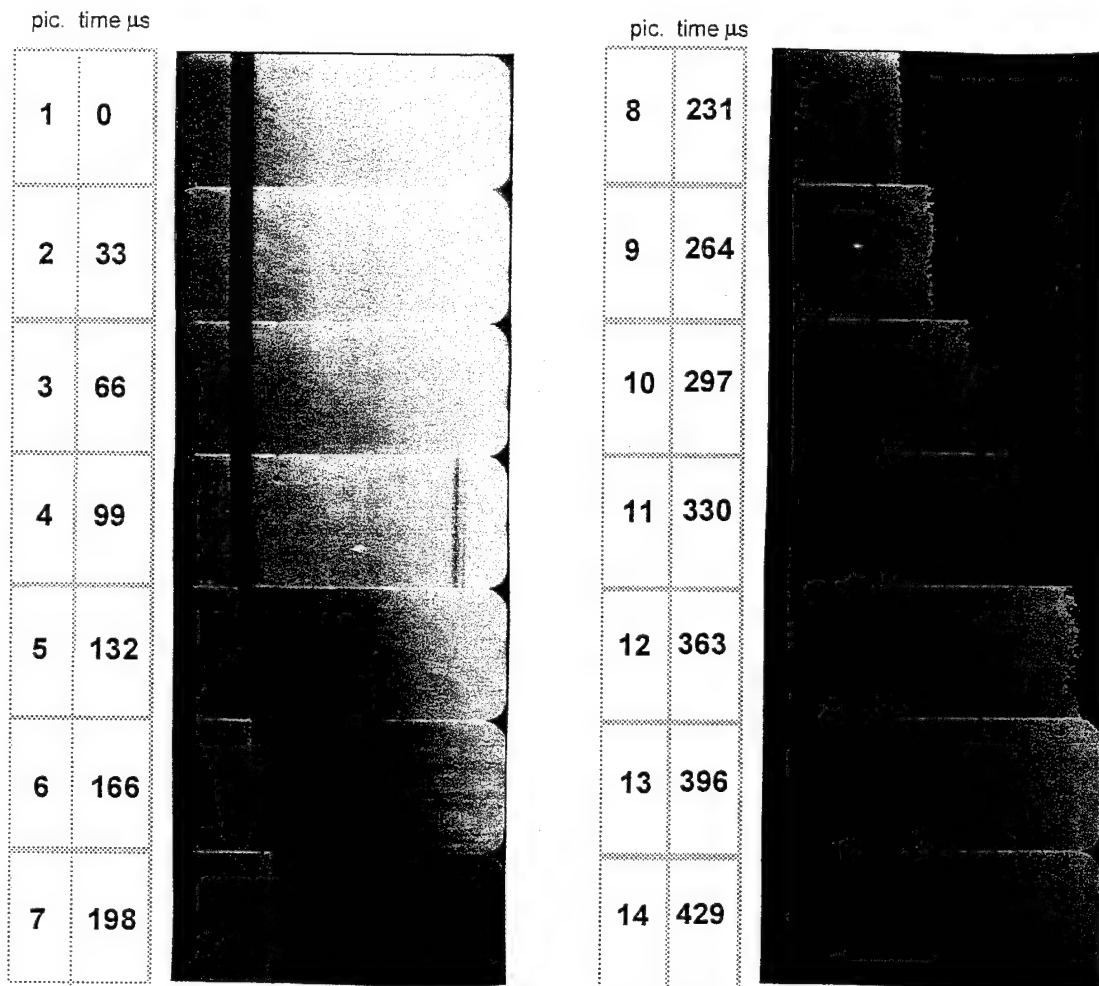
Wave Type	Shock Strength	Wave duration (ms)	D_i (mm)	V_g (m/s)	We_g	q	Re_g	v_l/v_g
Step	1.81	∞	1.41	168	3290	0.003	21500	0.065

Figure 12. Jet breakup sequence for Test 7



Wave Type	Shock Strength	Wave duration (ms)	D_i (mm)	V_g (m/s)	We_g	q	Re_g	v_l/v_g
Step	1.44	∞	1.04	98.95	701	0.026	8150	0.056

Figure 13. Jet breakup sequence for Test 8



Wave Type	Shock Strength	Wave duration (ms)	D_i (mm)	V_∞ (m/s)	We_∞	q	Re_∞	v_i/v_∞
Step	2.64	∞	1.04	300	10400	0.0017	35100	0.079

Figure 14. Jet breakup sequence for Test 9

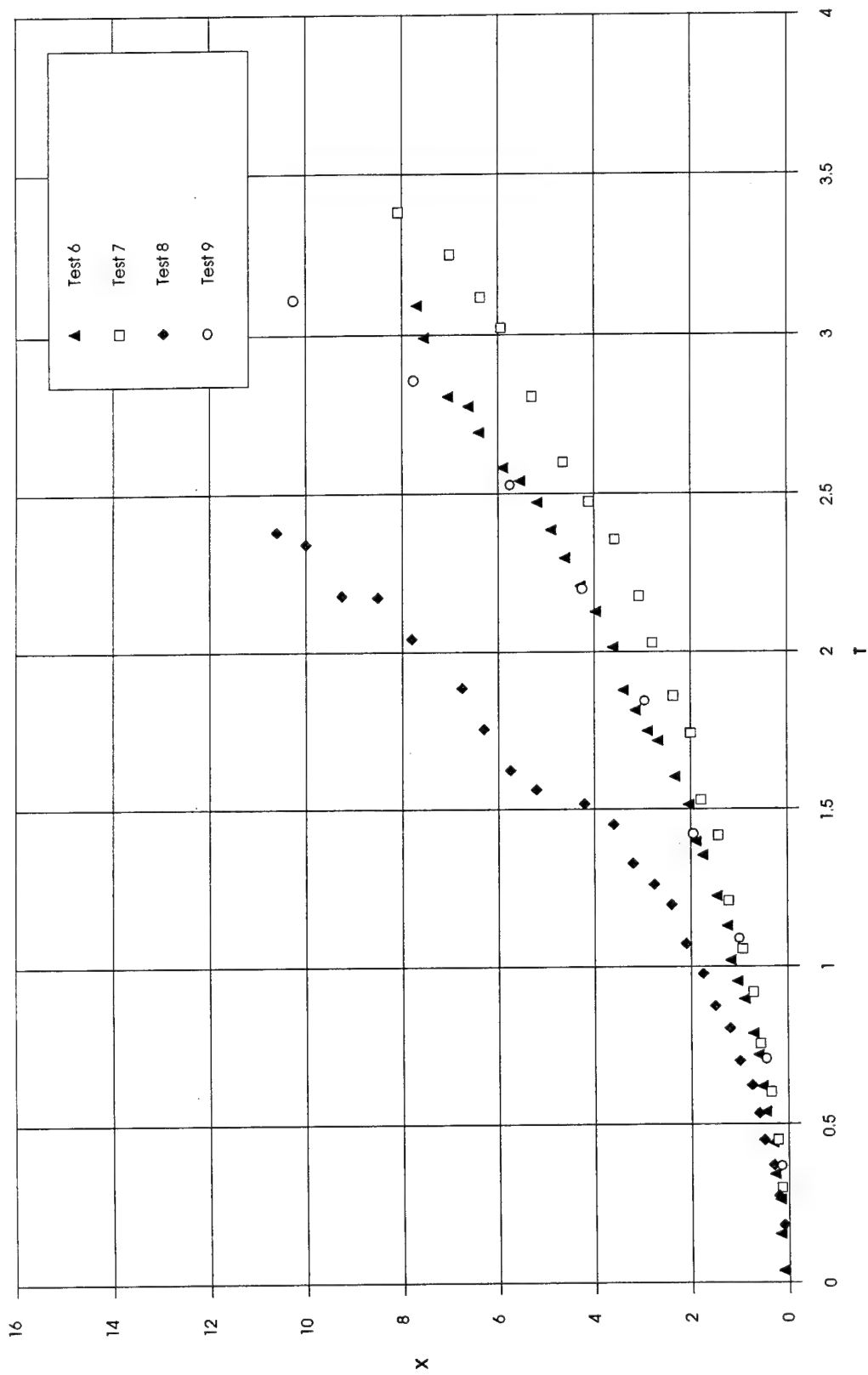


Figure 15. Dimensionless downstream displacement of a liquid jet under the influence of a square wave.

Figures 16-20 illustrate the jet breakup sequence for N-wave Tests 1-5, respectively. The results from these experiments indicate that the atomization controlling step is identical to that behind the square wave. The same physics, or breakup regime, applies to both square and N-wave induced breakup. This suggests that the breakup is controlled by the initial acceleration of the gas flow, not the rate of decay.

5.3.1 Jet Displacement

The values of the downstream displacement of the jet element as a function of its time after injection y/U_j , where x and y are the coordinates of the jet measured from the orifice parallel and normal to the freestream velocity, respectively, are available and discussed below for each experiment. A plot of the data obtained from experiments with an N-wave in the nondimensional form of $X = x/D_j$ as a function of $T = \frac{t V_g}{D_j} \sqrt{\frac{\rho_g}{\rho_j}}$ is

shown in Figure 21. Experiments with N-waves have a decaying gas flow velocity immediately behind the shock front. The liquid jet was shown to displace at a slower rate, as compared with its displacement behind a square wave. This is a result of a decaying normal stress acting on the jet column caused by the pressure drop immediately behind the wave.

In Tests 3 and 8, the same shock wave strength was generated (38%) for the same jet diameter (1.04 mm) but with a 2.3 ms duration N-wave and a long duration square wave, respectively. The percentage denotes the percent of pressure increase behind the shock front. In other words:

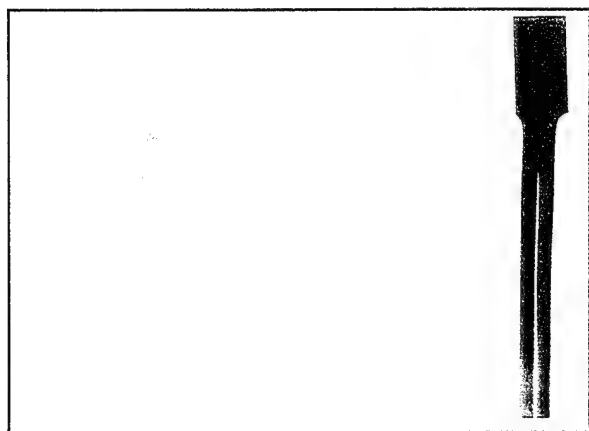
$$\text{Shock Strength (\%)} = \left(\frac{\Delta P}{P_1} \right) \times 100$$

or

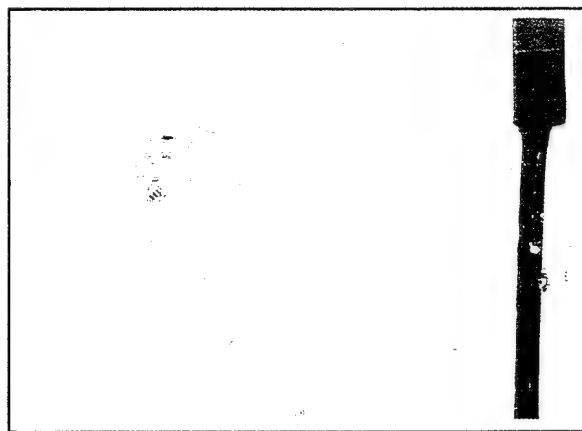
$$\text{Shock Strength (\%)} = \left(\frac{P_2}{P_1} - 1 \right) \times 100$$

where P_2/P_1 is the shock pressure ratio, and ΔP is the pressure difference across the shock.

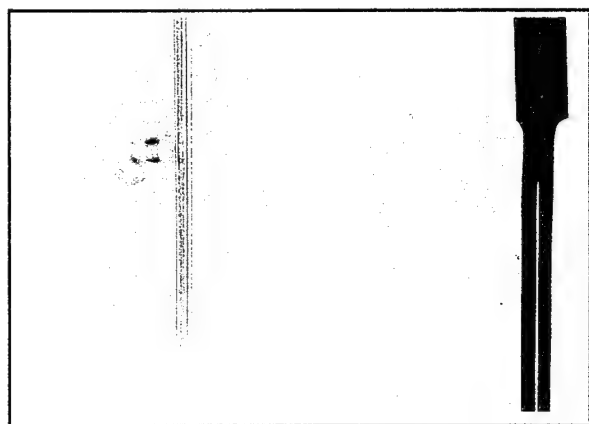
Pressure plots for these two waves are shown in Figures 22 and 23, respectively. The observation time for Test 3 and Test 8 was 1.1 ms. According to the jet breakup sequence of images in Figures 13 and 18 and the jet displacement plot in Figure 24, there is evidence that the jet responds differently to the N-wave. This is supported by the fact that, in the displacement plot, the jet displacement rate is less for the N-wave than it is for the constant flow induced by the square wave. A curve fit test was completed on the square wave plot and found that X varied with $T^{1.85}$ (Appendix B). With a constant gas



Initial Jet

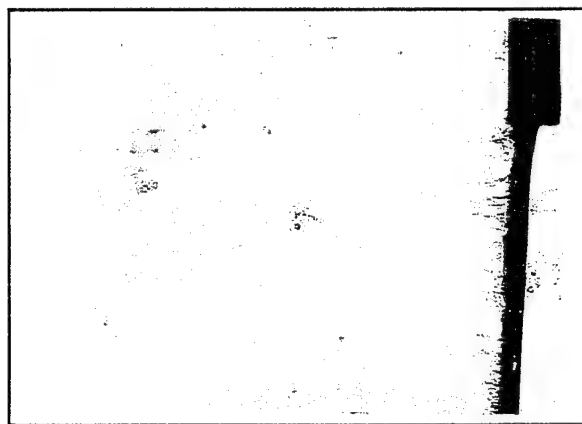


$t = 60 \mu s$

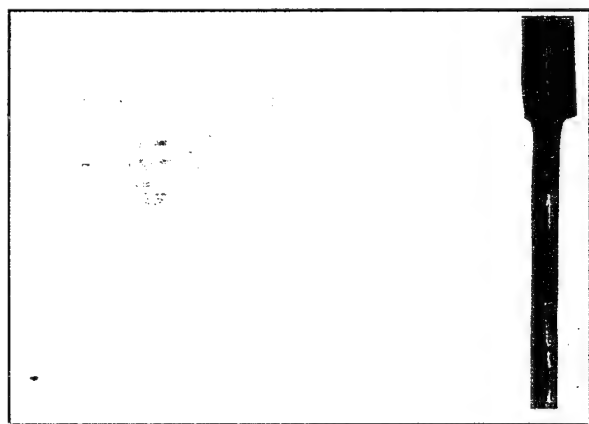


$t = 0 \mu s$

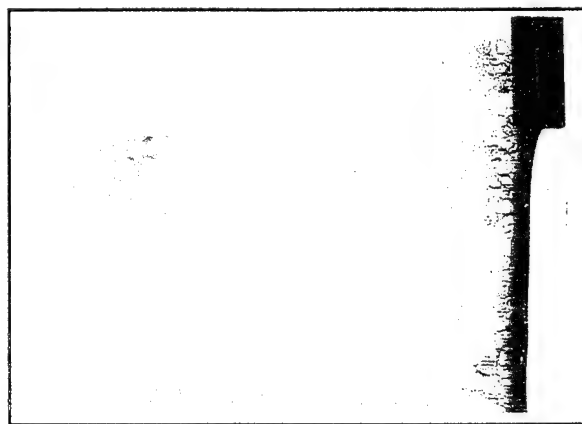
← shock



$t = 120 \mu s$



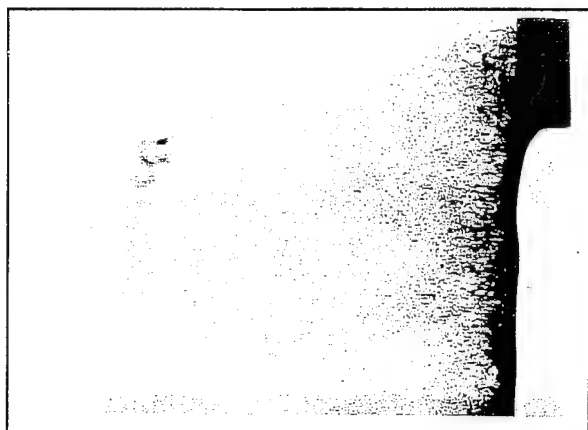
$t = 30 \mu s$



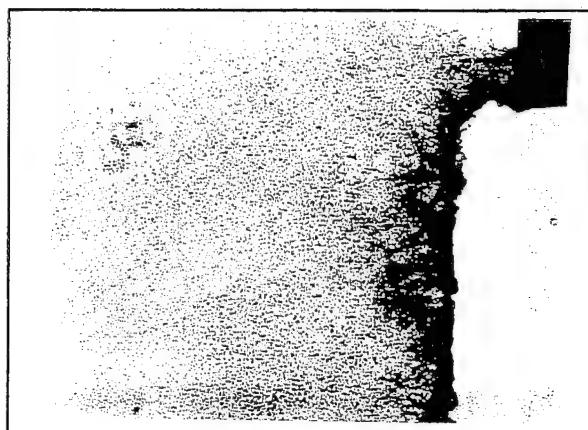
$t = 180 \mu s$

Wave Type	Shock Strength	Wave duration (ms)	D_i (mm)	V_g (m/s)	We_g	q	Re_g	v_i/v_g
N	1.33	5.5	0.8	75.78	371	0.094	5710	0.054

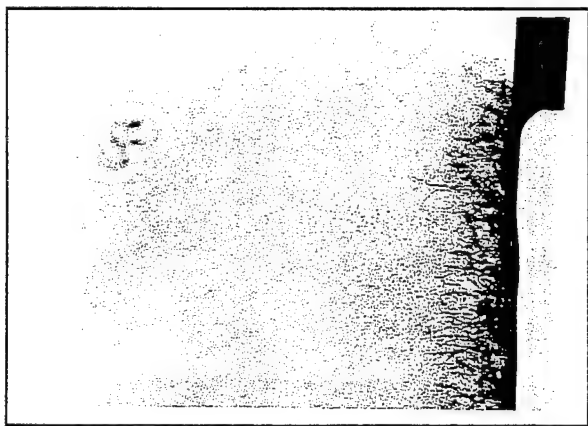
Figure 16a. Jet breakup sequence for Test 1



$t = 240 \mu s$



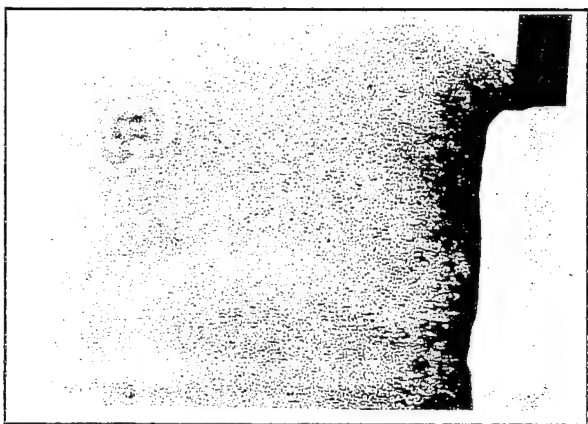
$t = 420 \mu s$



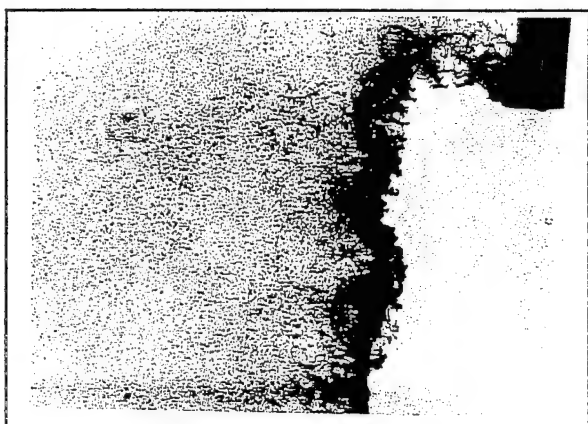
$t = 270 \mu s$



$t = 480 \mu s$

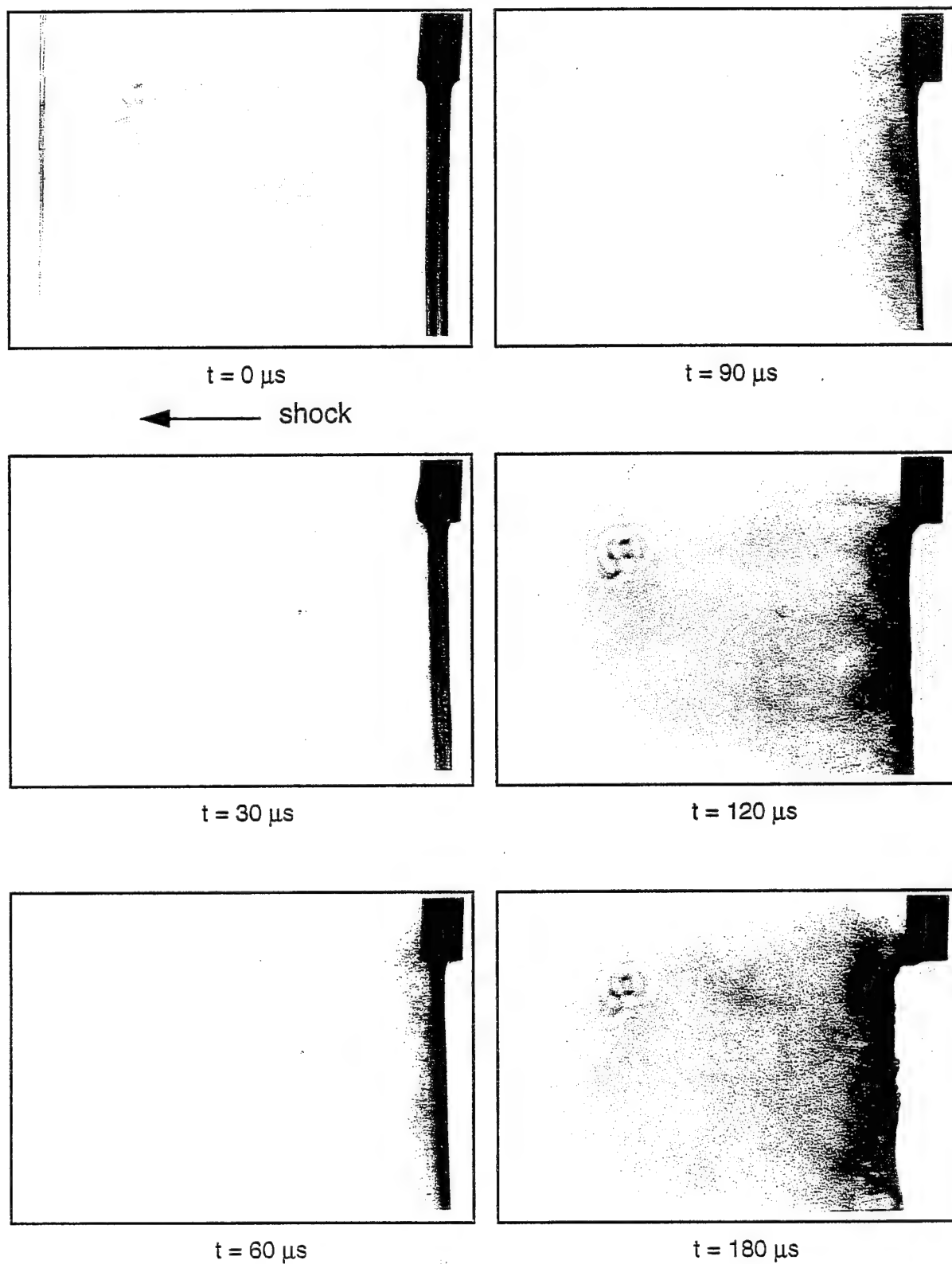


$t = 360 \mu s$



$t = 540 \mu s$

Figure 16B. Still images of different stages of jet breakup for Test 1

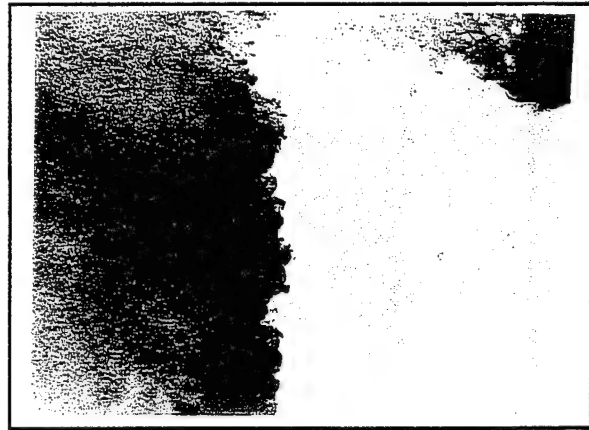


Wave Type	Shock Strength	Wave duration (ms)	D_1 (mm)	V_g (m/s)	We_g	q	Re_g	v_l/v_g
N	1.56	5.5	1.0	122	871	0.032	8100	0.059

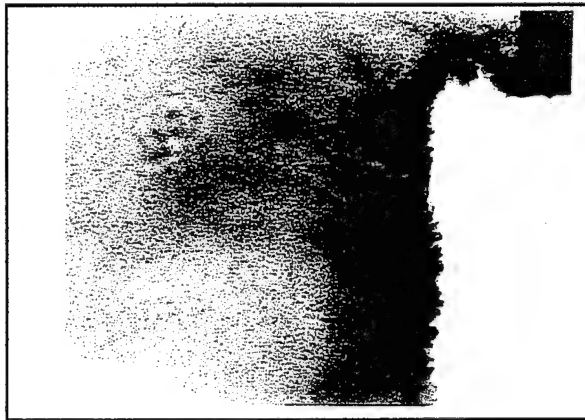
Figure 17a. Jet breakup sequence for Test 2



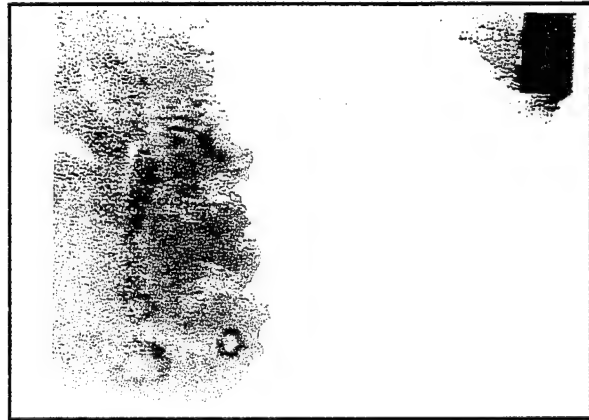
$t = 240 \mu s$



$t = 420 \mu s$



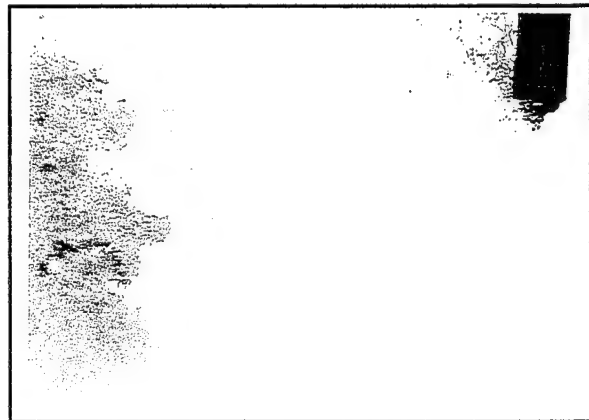
$t = 270 \mu s$



$t = 480 \mu s$

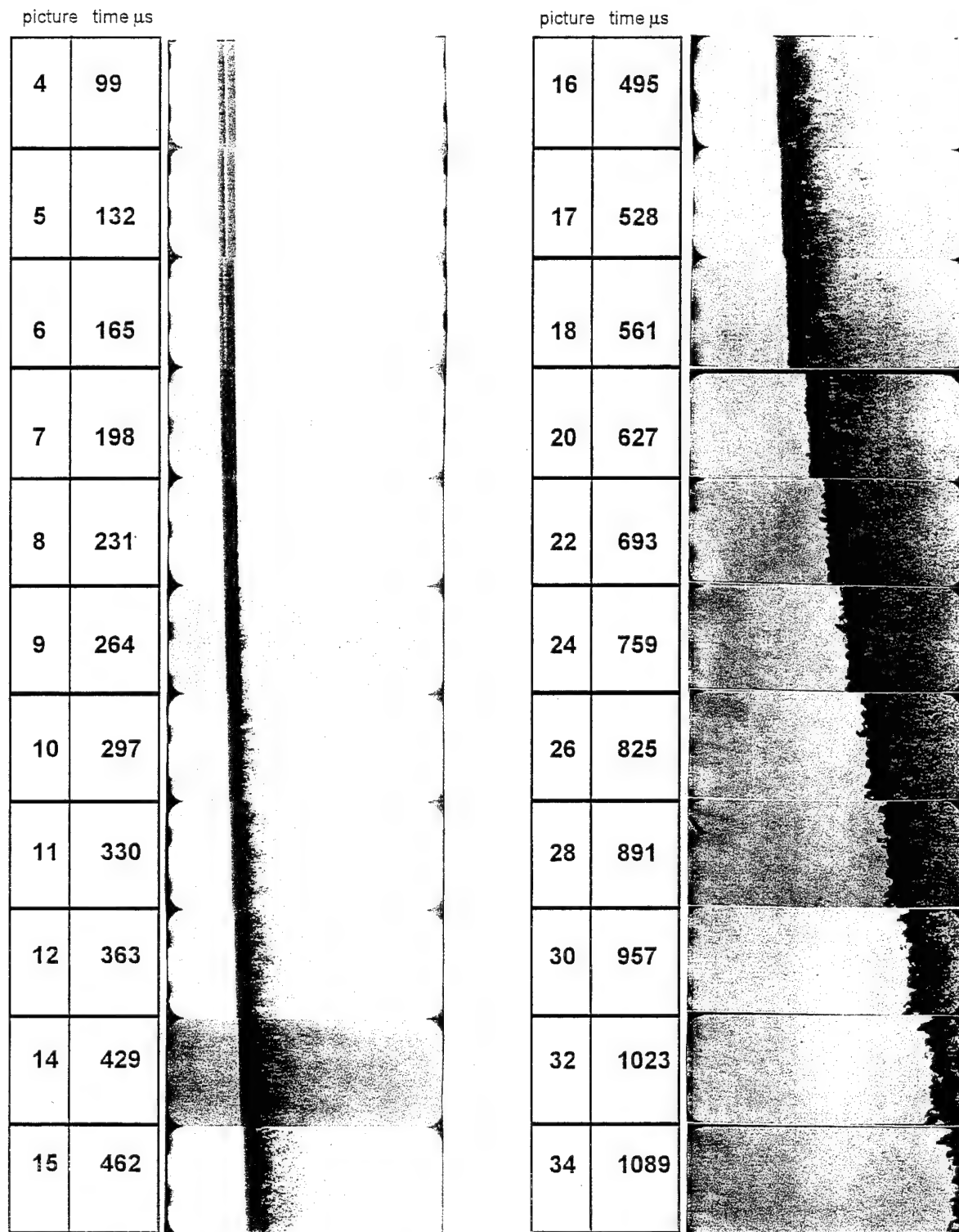


$t = 360 \mu s$



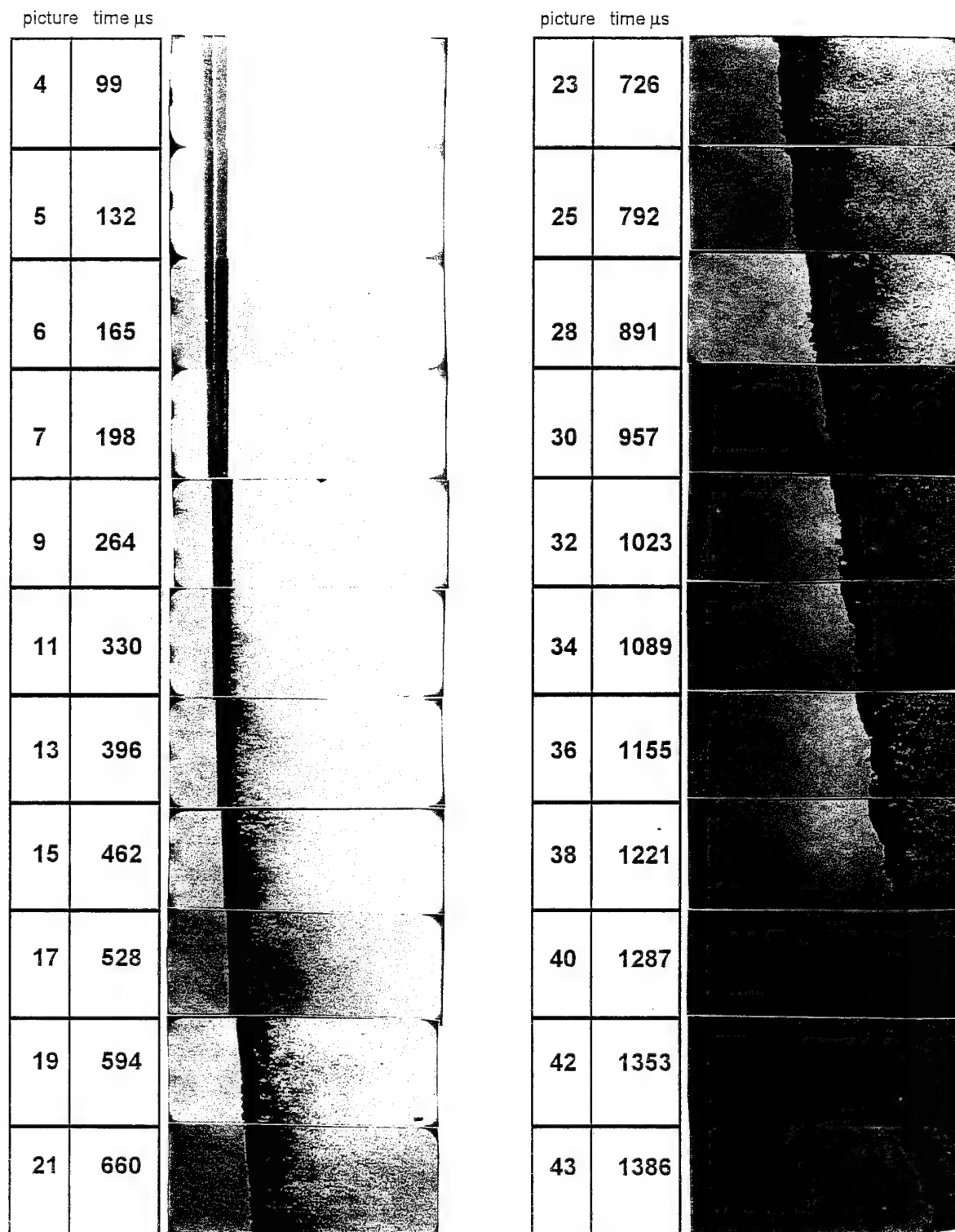
$t = 540 \mu s$

Figure 17B. Still images of different stages of jet breakup for Test 2



Wave Type	Shock Strength	Wave duration (ms)	D_i (mm)	V_g (m/s)	We_g	q	Re_g	v_l/v_g
N	1.39	2.3	1.04	89	549	0.033	7200	0.055

Figure 18. Jet breakup sequence for Test 3



Wave Type	Shock Strength	Wave duration (ms)	D_i (mm)	V_g (m/s)	We_g	q	Re_g	v_i/v_g
N	1.37	2.3	1.41	84.6	669	0.003	9160	0.055

Figure 19. Jet breakup sequence for Test 4

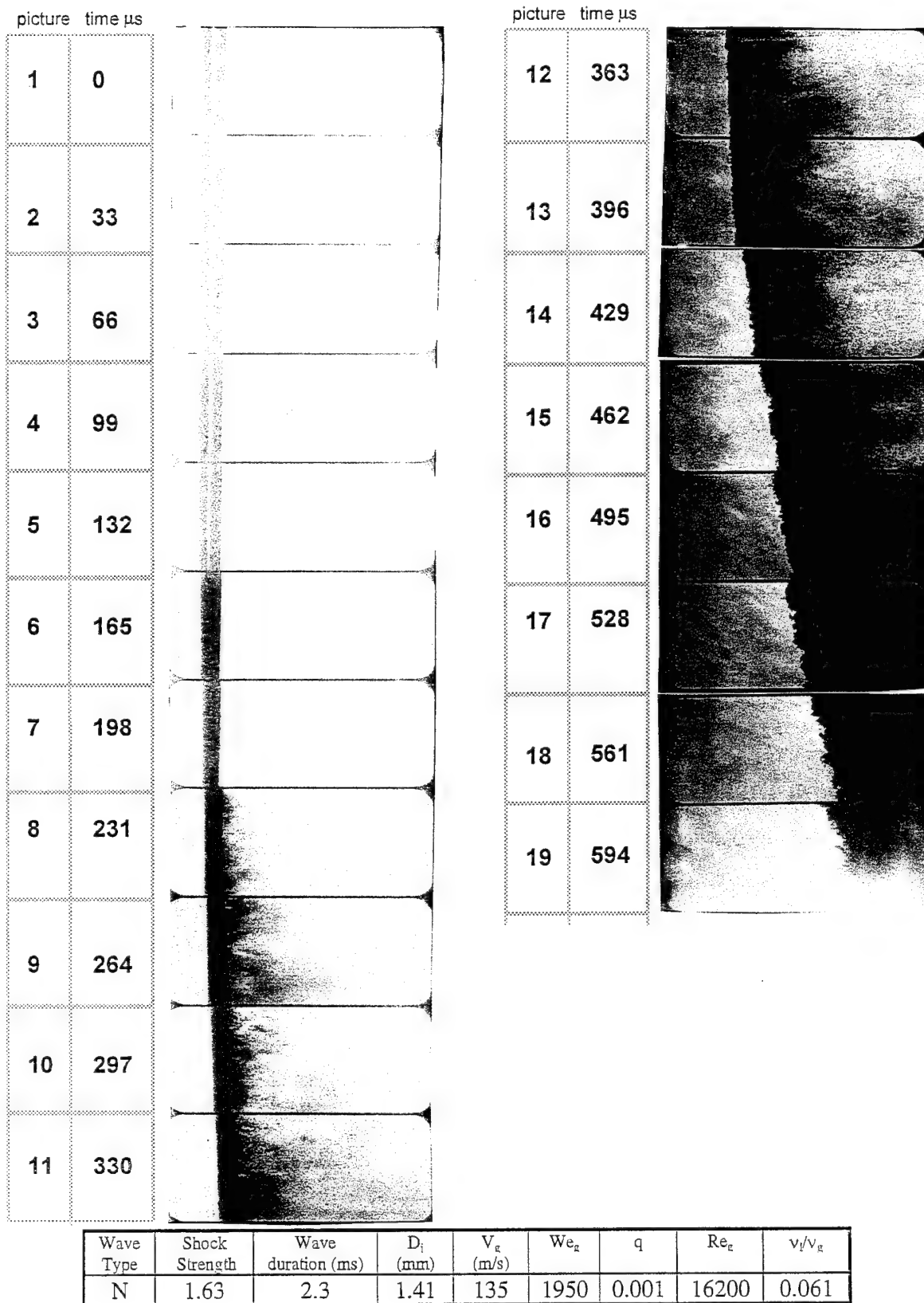


Figure 20. Jet breakup sequence for Test 5

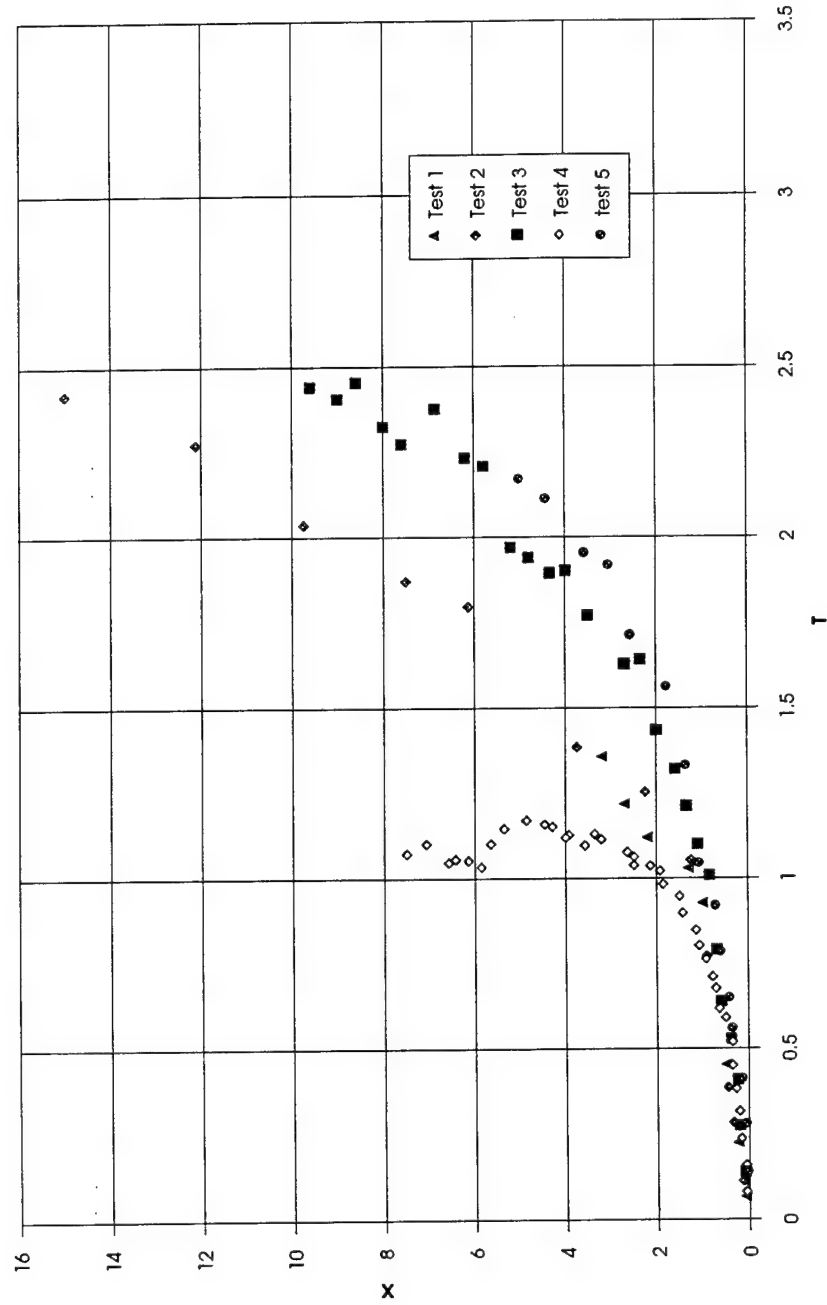


Figure 21. Dimensionless downstream displacement of a liquid jet under the influence of an N-wave.

flow velocity and density, the value of T will only increase with time at a constant rate. However, the value of X is changing more rapidly denoting that there is an acceleration of the jet into the freestream flow. A curve fit for Test 3 resulted in X varying with $T^{1.70}$. Therefore the jet accelerates with the gas flow behind an N-wave relative to the acceleration experienced with a square wave.

In Figure 25, the dimensionless displacement is plotted for another condition where the N-wave can be compared to the square wave (Tests 4 and 6). The pressure plots are shown in Figures 26 and 27. These two tests were similar to the one studied previously, however, a larger jet diameter was used (1.41 mm). The larger jet diameter appears to have slowed the jet displacement. It is more evident here that the N-wave decreased the value of T due to the sudden drop of gas flow velocity and density. In the

expression for $T = \frac{t V_g}{D_j} \sqrt{\frac{\rho_g}{\rho_j}}$, the value of the product of the gas velocity and the square

root of the gas density, $V_g \sqrt{\rho_g}$ decreases at a faster rate behind the decaying flowfield on an N-wave compared to the rate of increase of t . Meanwhile, the jet continues to get displaced. As a result, dX/dT , in Figure 25, will initially have a positive slope and then have a negative slope when the gas velocity behind the wave decays rapidly. A similar study was conducted between Tests 5 and 7 but at a higher shock strength (Figures 28 and 29, respectively). The profile of the displacement for the square wave is similar to that observed at the lower gas velocity (Figure 30). However, the N-wave profile differs. The gas flow behind the N-wave is higher than it was for Test 4. Therefore, the jet displaced quicker and limited the observation time. During this time the N-wave did not have a very strong effect in decelerating the jet displacement. Therefore, the gas flow velocity remained almost constant. This explains the reason the two profiles are rather similar to each other. In other words, during the observation time, Test 5 behaved similar to Test 7 since, during the limited observation time, the gas velocity did not significantly decline behind the N-wave.

5.3.2 Ligament and Drop Formation

A detailed analysis of ligament and drop formation was undertaken for Tests 1 and 2. These images were captured using high resolution still photographs, and were visually inspected for the different regimes of breakup (Figures 16 and 17). Table 4 illustrates the gas and liquid phase properties calculated for these tests. Test 1, with a peak pressure increase of 34%, had a shock Mach number of 1.14 with a peak gas flow velocity of 76 m/s. The pressure time history is shown in Figure 31. The pressure plots also represent the time and the instantaneous pressure value for each picture.

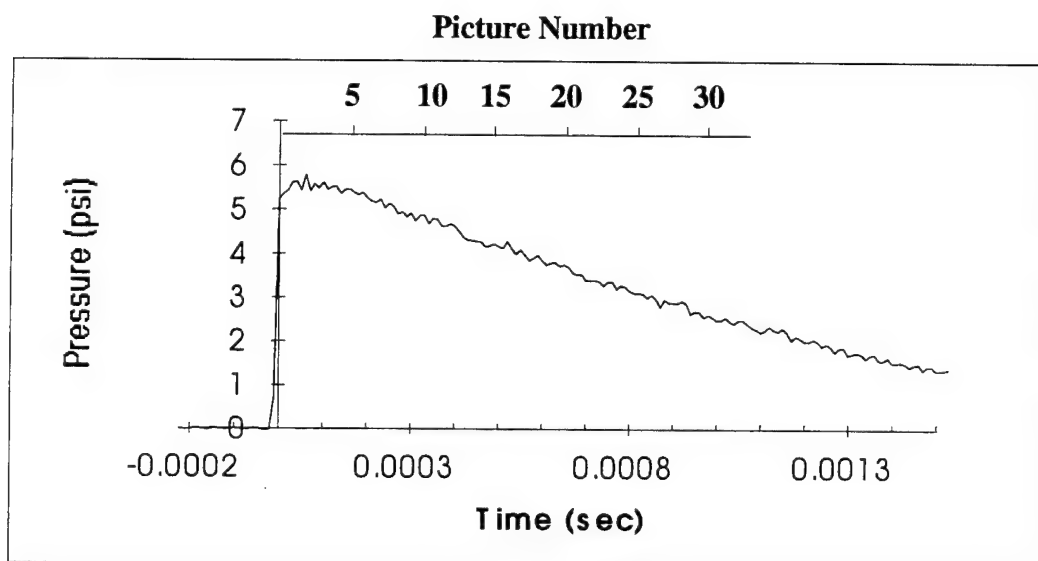
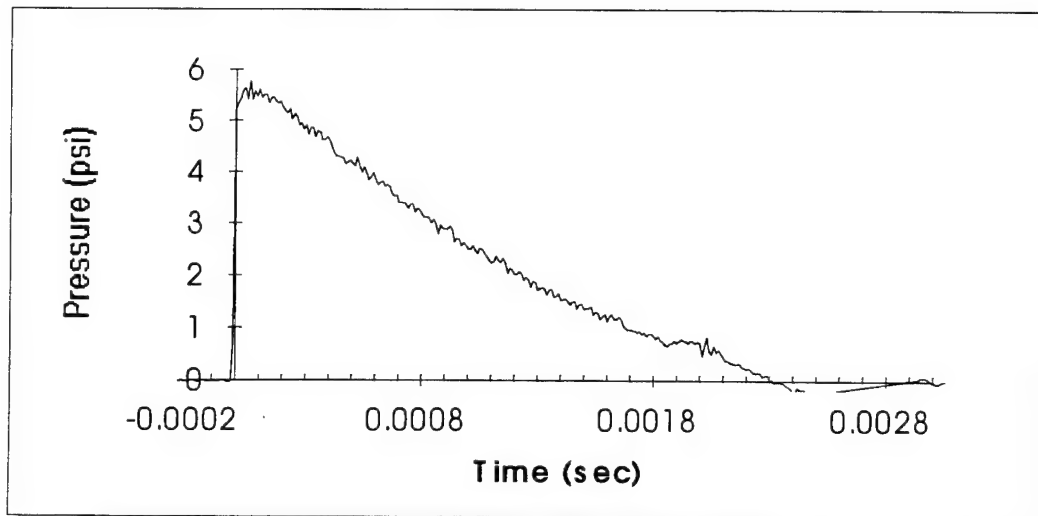


Figure 22. Pressure Time History for Test 3 (top) full duration (bottom) 1.5 msec duration

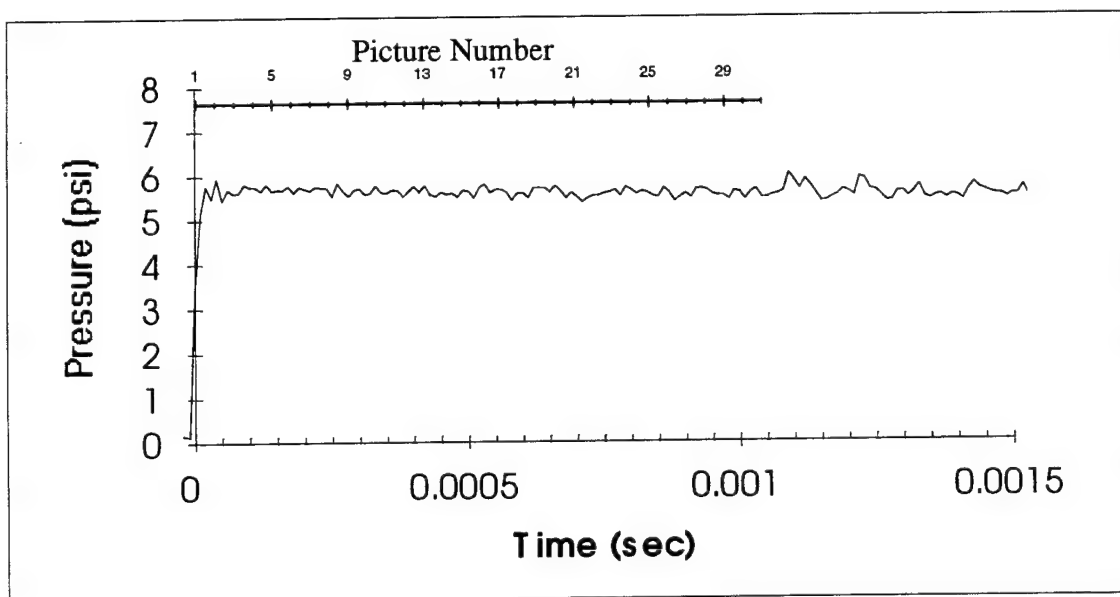
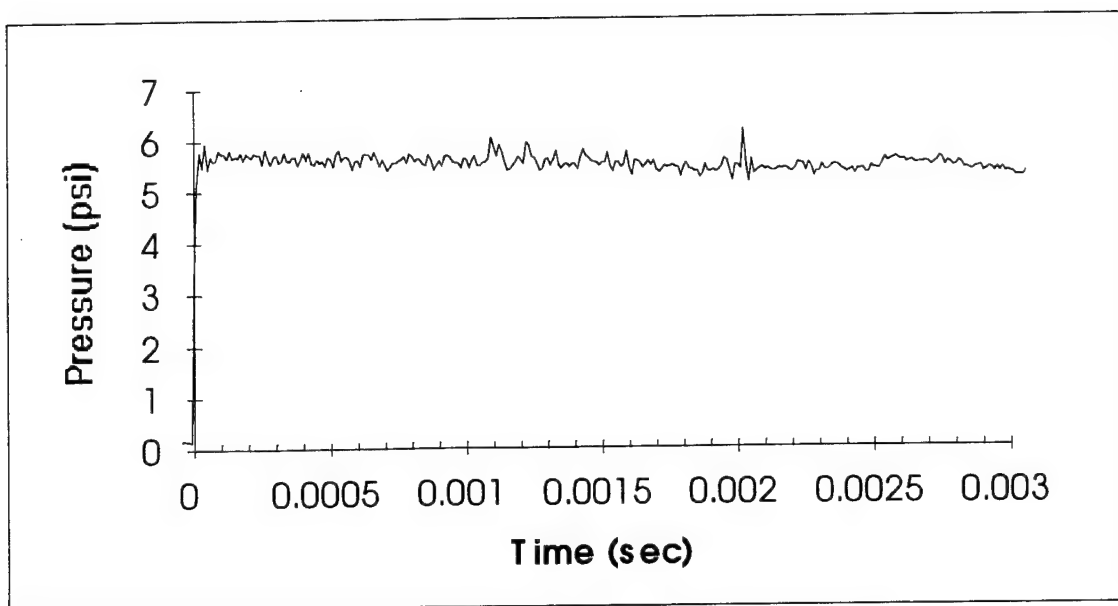
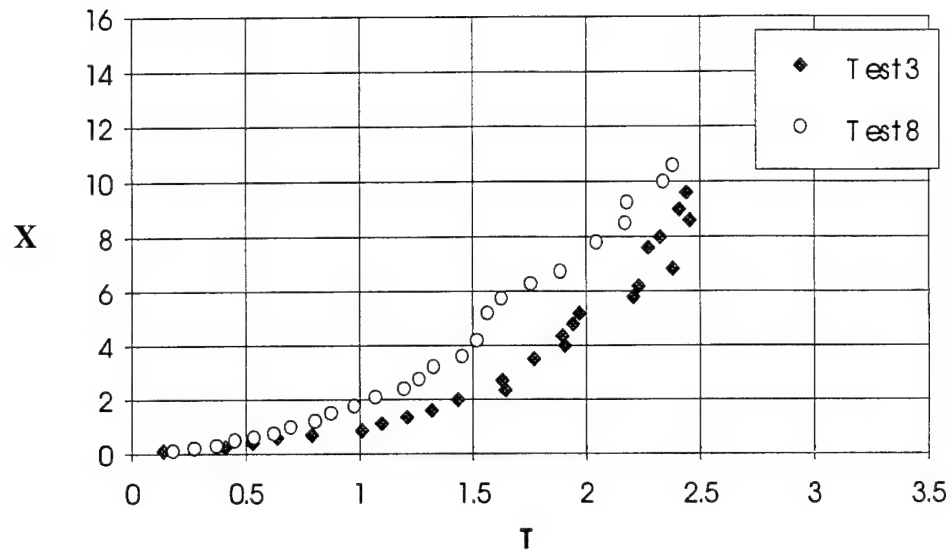
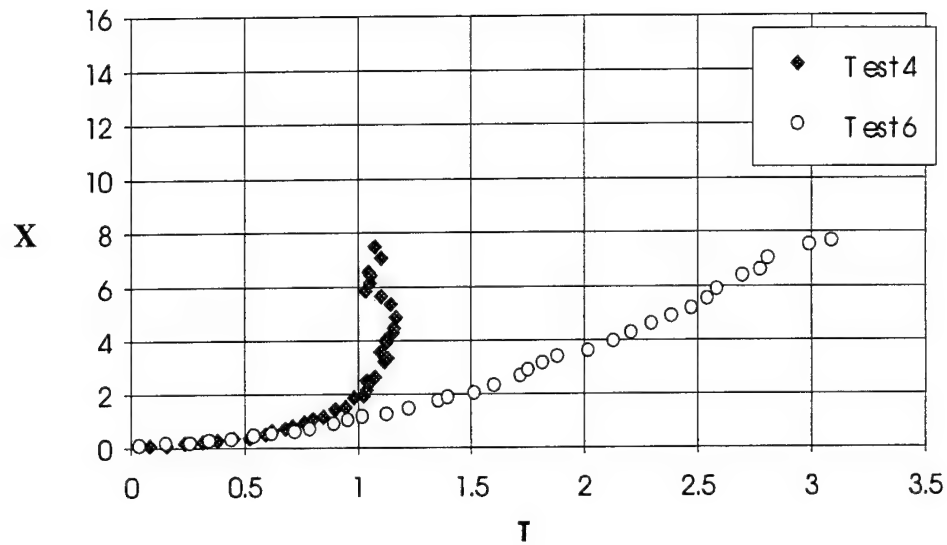


Figure 23. Pressure Time History for Test 8 (top) full duration (bottom) 1.5 msec duration



Test	Wave Type	Strength (%)	Duration (ms)	Diameter (mm)
3	N	38	2.3	1.04
8	S	38	infinite	1.04

Figure 24. Dimensionless downstream displacement of a liquid jet for Test 3 and Test 8.



Test	Wave Type	Strength (%)	Duration (ms)	Diameter (mm)
4	N	37	2.3	1.41
6	S	37	infinite	1.41

Figure 25. Dimensionless downstream displacement of a liquid jet for Test 4 and Test 6.

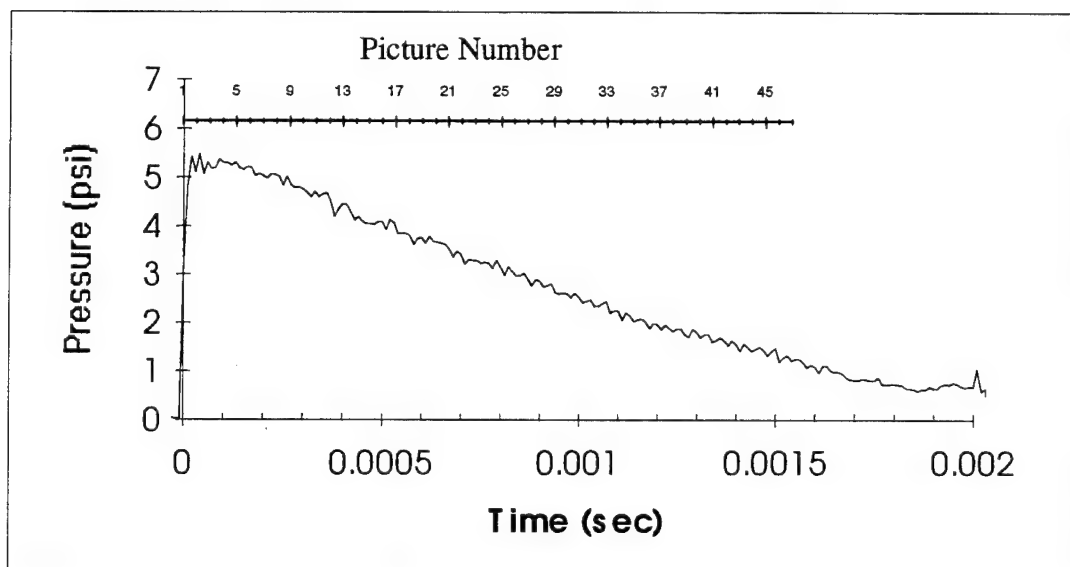
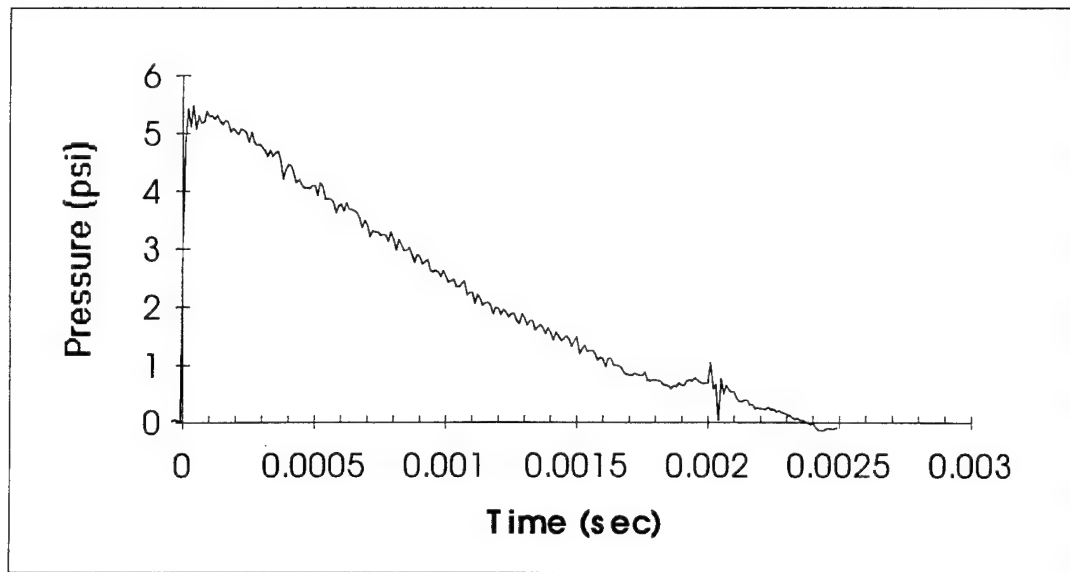


Figure 26. Pressure Time History for Test 4 (top) full duration (bottom) 2.0 msec duration

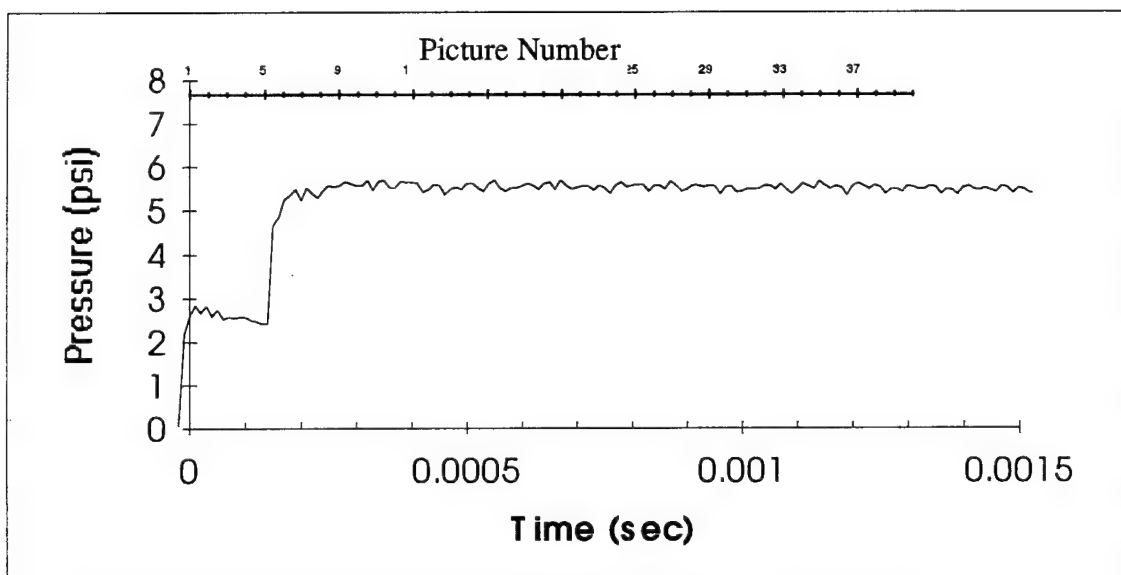
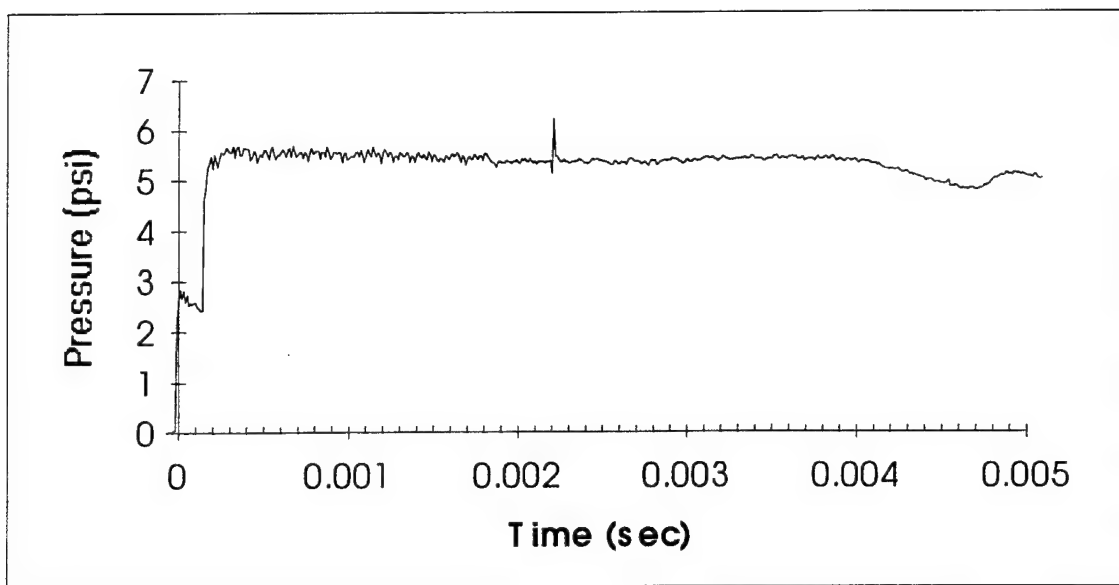


Figure 27. Pressure Time History for Test 6 (top) full duration (bottom) 1.5 msec duration

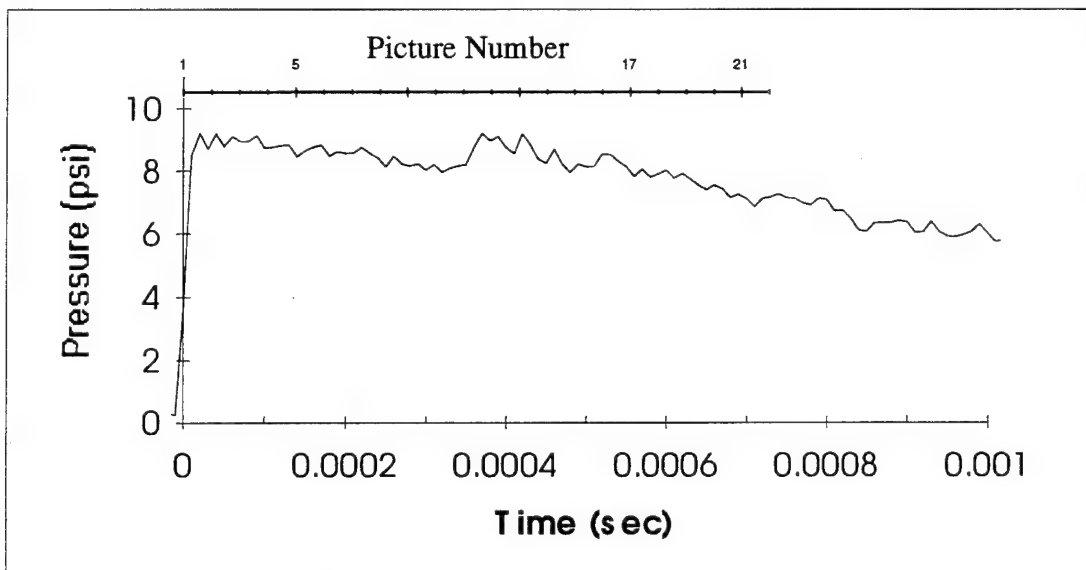
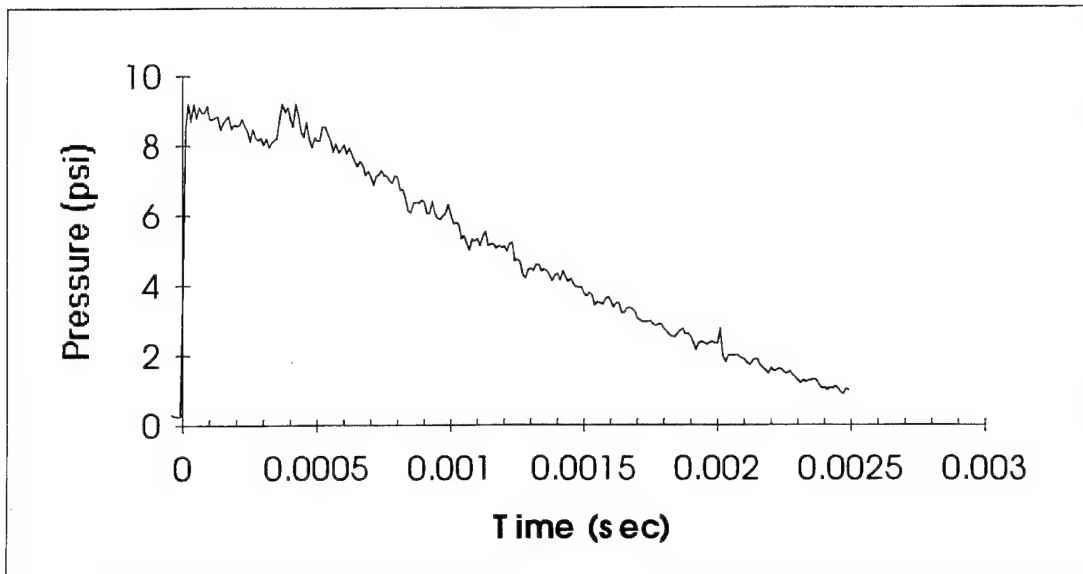


Figure 28. Pressure Time History for Test 5 (top) full duration (bottom) 1.0 msec duration

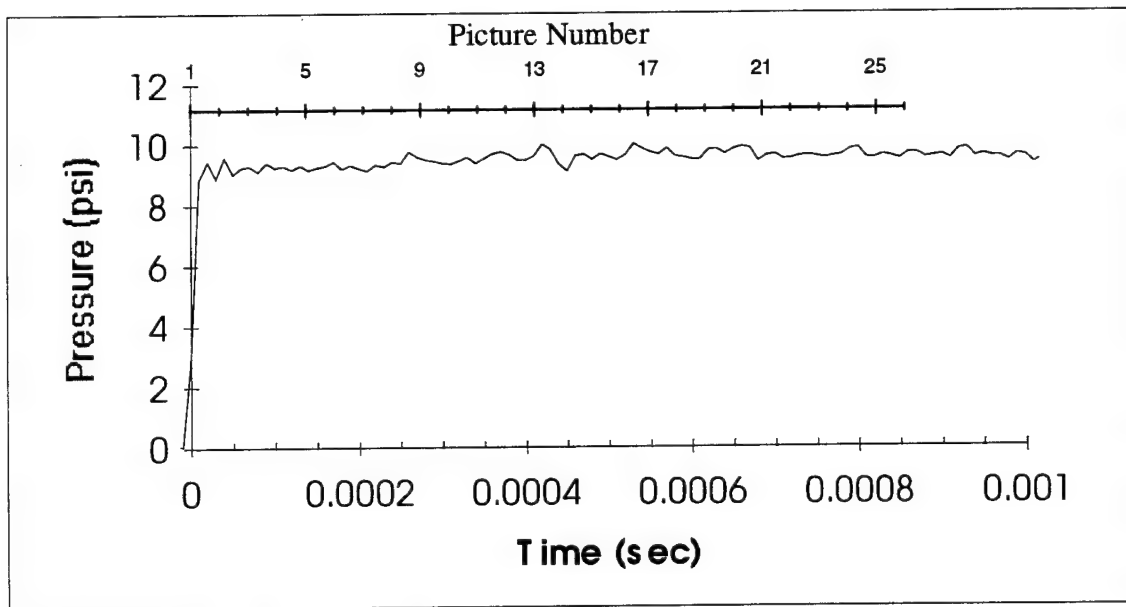
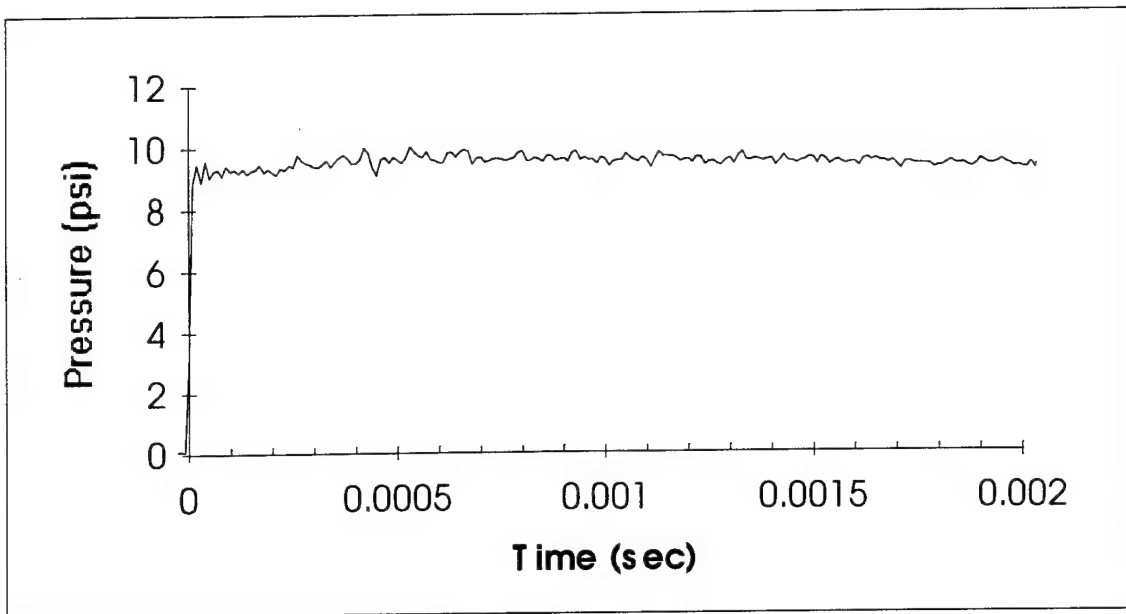
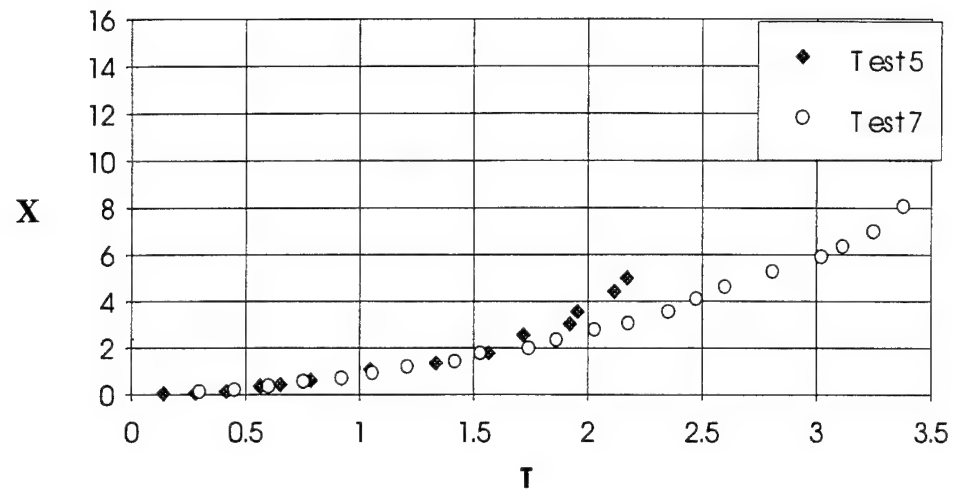


Figure 29. Pressure Time History for Test 7 (top) full duration (bottom) 1.0 msec duration



Test	Wave Type	Strength (%)	Duration (ms)	Diameter (mm)
5	N	62	2.3	1.41
7	S	65	infinite	1.41

Figure 30. Dimensionless downstream displacement of a liquid jet for Test 5 and Test 7.

The methanol jet diameter was 1.0 mm with a jet velocity of 1.0 m/s. Figures 16a and 16b illustrate still images of the breakup sequence for Test 1. Note, that each image for Test 1 and 2 is a result of a different experiment captured with a 35 mm Pentax camera at various stages of breakup. Each experiment produced repeatable shocks to within 0.1 psi.

In this subsonic crossflow, the jet expands uniformly and breaks off at the trough of a column wave. The images show that, with the passage of an N-wave, the jet undergoes distortion during the 0 - 60 μ s time frame. Ligament formation occurs at the outer edge of the ellipsoid liquid core at 120 μ s. Thin liquid sheets become visible at this time at which point 50 μ m drops are stripped away and entrained in the gas flow. After 360 μ s, surface waves appear on the liquid sheet surface due to the turbulent gas flow, and jet displacement is initiated. Clouds of drops are entrained in the gas flow as the surface wave amplitude increases. The remainder of the jet is entrained in the gas flow with 50 - 75 μ m droplets. The last image, taken at 540 μ s, did not encompass the complete breakup process and the behavior of the jet in a decaying gas flow velocity field. In fact, the gas velocity remained relatively constant during these times.

Test 2 was conducted with a higher initial diaphragm pressure ratio and resulted in a 57% peak pressure increase across the shock wave. The shock Mach number was 1.22 with peak gas flow velocity of 122 m/s. Figure 32 shows the pressure time history for the 57% wave. The jet breakup sequence is shown in Figure 17a and 17b. At 30 μ s after the passage of the shock wave, the jet initiates the distortion process and flattens into an ellipse shape. Thin ligaments form at the outer edge of the ellipsoid after 60 μ s. Drops begin to entrain in the gas flow at 90 μ s. After 120 μ s, the liquid core has completely flattened to a long liquid sheet. The average size of drops entrained in the gas flow is ~30 μ m. The jet displaces from the injector after 180 μ s and travels downstream of the shock tube at 16 m/s. Surface waves form on the sheet surface at this time. A cloud of fine droplets are stripped away from the liquid sheet and entrained in the gas flow. At 270 μ s, the liquid sheet has displaced 3 mm away from the injector centerline.

After 540 μ s, fresh liquid has emerged from the injector exit. This indicates that the gas flow behind the shock has no effect on jet recovery rate, which was approximately equal to the nominal jet velocity. The shock front may, however, produce an interruption of the liquid flow into the test section.

Droplet diameters were measured for a selected area of some of the jet photographs for Tests 3, 4, 5, 6, 7, 8, and 9. The droplets were measured by enlarging the selected area which results in a total magnification of 70, and measuring the diameters with a graduated scale. The droplet diameter determination obtained here has validity only as a determination of the sizes of initial droplets (i.e., droplets close to the point of injection as is the case for all of the particles in the photographs) for each test. The degree of jet breakup was not a consideration in these measurements, and may be very large or very small. Furthermore, the downstream droplet distribution would probably be quite different, due to secondary breakup and evaporation. The measurement was limited to

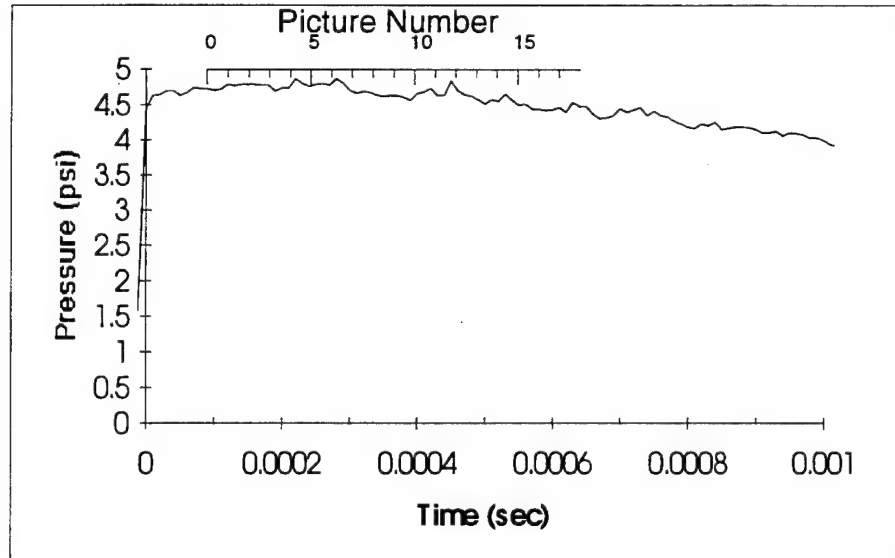
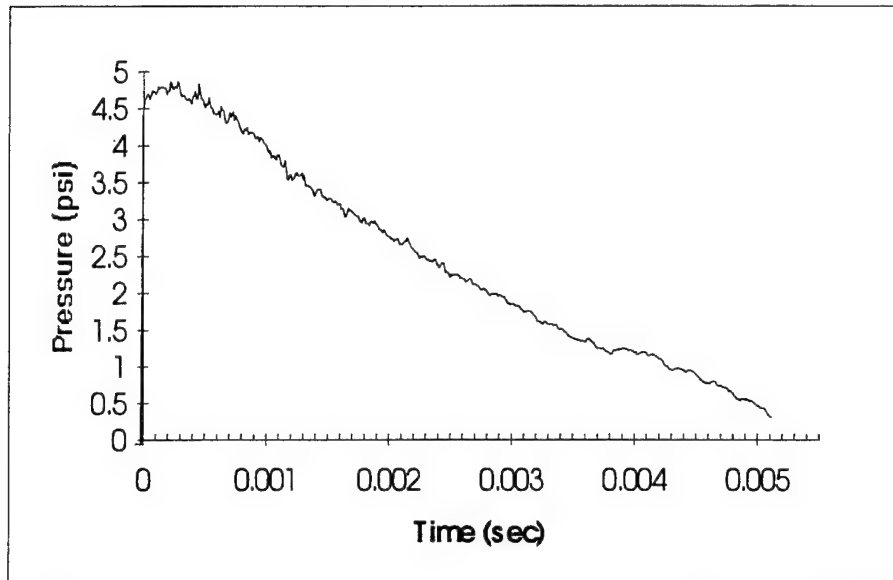


Figure 31. Pressure Time History for Test 1 (top) Full wave duration (bottom) 1 msec wave duration

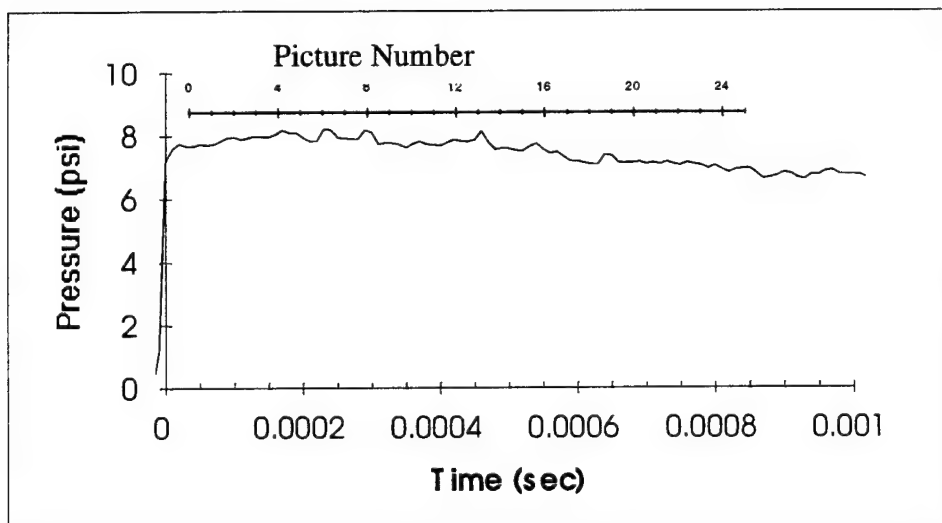
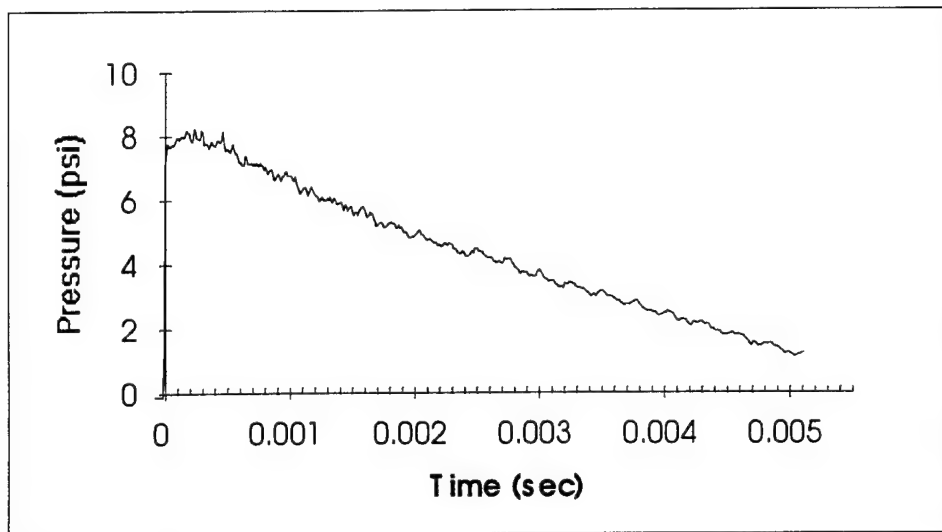


Figure 32. Pressure Time History for Test 2 a) Full wave duration
b) 1 msec wave duration

particles which approximate spheres. This was arbitrarily defined as particles for which the maximum diameter does not exceed the minimum diameter by more than two to one. For the nonspherical particles thus counted, the droplet diameter was defined by (max-diam + min-diam)/2. Furthermore, only those particles and droplets that were in good focus were counted.

Under the above restrictions, the mean droplet diameters were measured and tabulated in Table 5. Figure 33 illustrates the beneficial influence of increased levels of airstream velocity upon the spray drop size for two injector diameters. Figure 34 illustrates the influence that the diameter of the injection orifice has upon the spray quality. The average dropsize is observed to increase with an increase in orifice diameter.

Table 5. Mean measured droplet diameters

Test Number	Avg. Diam.(μm)	Jet Diam. (mm)	Jet Veloc.(m/s)	Gas Veloc.(m/s)
1	30	0.8	1.0	76
2	22	1.0	1.0	122
3	37	1.04	0.71	89
4	50	1.41	0.435	85
5	33	1.41	0.435	135
6	43	1.41	0.435	97
7	28	1.41	0.435	168
8	26	1.04	0.71	99
9	17	1.04	0.71	300

5.4 Parametric Studies

In addition to exploring two wave types, variations in the following parameters were explored:

- Shock wave strength
- Jet diameter

5.4.1 Effect of Shock Strength

a higher shock strength produces a more rapid breakup than the 34% wave. In addition, quantitative analysis was done by plotting the jet displacement data in nondimensional form of $X = x/D_j$ as a function of $T = \frac{t V_g}{D_j} \sqrt{\frac{\rho_g}{\rho_j}}$. Since the images were all captured

before the jet was influenced by the negative acceleration, (the last data point for Tests 1 and 2 were taken at $t=540 \mu\text{s}$) the assumption is made that the freestream velocity was relatively constant. Based on this assumption, the displacement plot for two conditions was expected to have a similar slope. However, the displacement of the jet behind a 57%

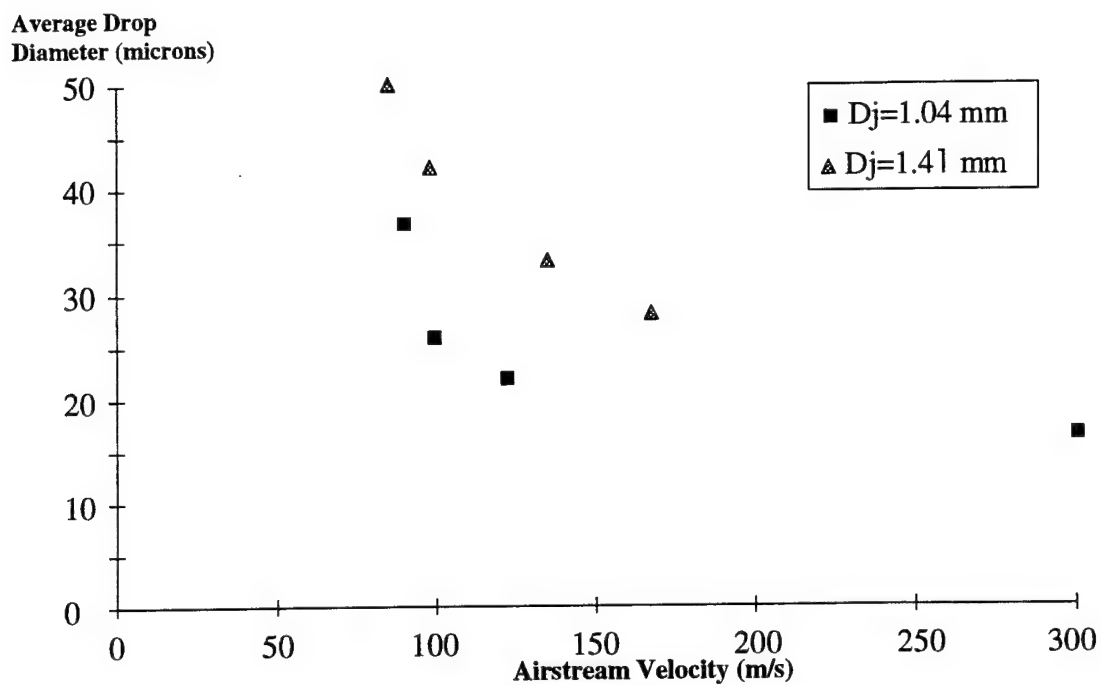


Figure 33. Influence of airstream velocity upon spray dropsize

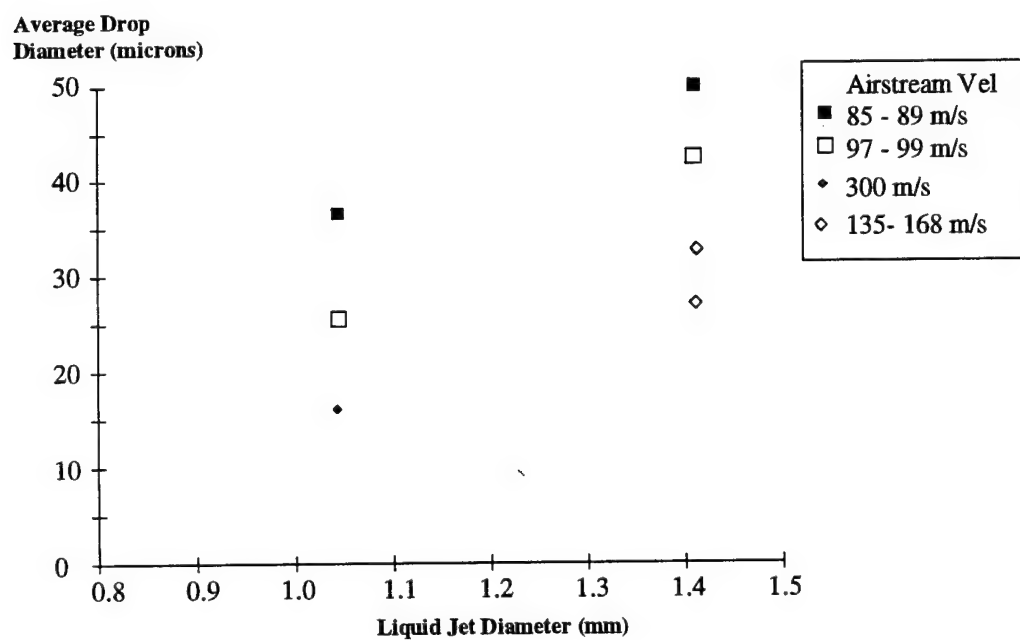


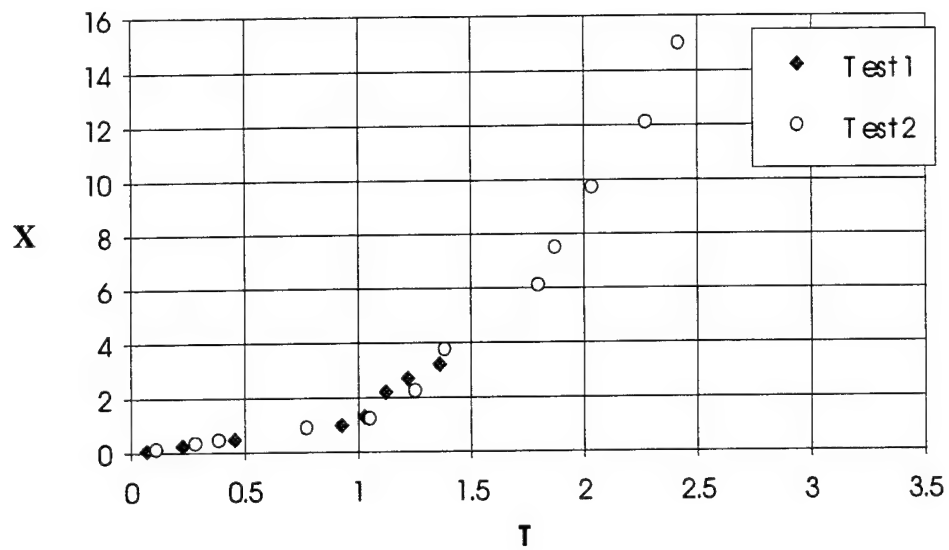
Figure 34. Influence of Liquid Orifice Diameter Upon Spray Dropsize

wave occurred much quicker. According to the displacement plot, the 57% wave produced a much higher displacement value, at the time the last picture was taken. This can be explained by the dynamic force of the gas flow which is much higher for the higher strength shock. And since the liquid jet dynamic pressure was the same for the two cases, the momentum transfer between the gas and liquid is much greater for the higher strength shock. Therefore, the liquid/gas dynamic pressure ratio (q) is much smaller for the 57% wave. Hence, displacement occurs much more rapidly. The maximum Weber numbers for Tests 1 and 2 were 370 and 870, respectively. However, the Weber number has shown to have greater effect on jet breakup and almost none on jet displacement.

The effect of wave strength on jet breakup was also studied for an N-wave, but for a different wave duration. Tests 4 and 5 generated a 2.3 millisecond (ms) wave duration with a 37% and 62% shock strength, respectively. The pressure plots are shown in Figures 36 and 37. Due to the short wave duration the pressure decrease behind this type of an N-wave is much more sudden. The diameter of the jet was 1.41 mm. From the images (Figures 19 and 20) and the displacement plot in Figure 38, it was shown that the rate of jet displacement was much higher for the 62% N-wave. Due to this faster displacement, the observation time of the jet was less than for the 37% wave (725 μ s vs 1500 μ s). Therefore, during this time the liquid jet did not have the opportunity to decelerate behind the N-wave. In fact, there was only a 20% reduction in static pressure of the gas flow at 725 μ s whereas, for the 37% N-wave, the pressure decreased by 75%, denoting a large deceleration of the jet by 1500 μ s. Due to this pressure drop, the gas velocity and density also experience a sudden decrease.

Since the dimensionless time T is dependent on this decreasing gas velocity and density, the value of T begins to decrease with time as the jet displacement continues but at a slower rate. In Figure 38, this behavior is clearly illustrated as a sudden increase of the slope of the plot for Test 4. In Test 5, the gas flow velocity remained relatively constant; therefore, with an increase in time the total value of T increased, even though the gas velocity and density may have decreased by a small value. Jet behavior was further illustrated in the comparison between Tests 4 and 7, where in Test 7 a 65% square wave was generated (Figure 39). The gas flow velocity behind the square wave was constant so that the value of T increased with time. This explains the reason why the slope of the dimensionless downstream displacement in Figure 40 is smaller for the constant velocity Test 7. The jet breakup sequence for Test 7 is shown in Figure 12.

The effect of liquid jet displacement behind a low and high strength square wave was also analyzed. In Test 8, a 39% square wave was generated (Figure 41). In Test 9 a 254% square wave was generated (Figure 42). The displacement plot for the 1.04 mm diameter jet for both tests is shown in Figure 43. Due to the very high gas flow velocity behind the 254% wave (300 m/s) jet displacement occurred very rapidly. Therefore the observation time was limited to 460 μ s before the image exited the view field of the camera. From the jet breakup sequence for Test 9 in Figure 14, it is clearly visible that the jet displaces more rapidly as compared with Test 8 (Figure 13).



Test	Wave Type	Strength (%)	Duration (ms)	Diameter (mm)
1	N	34	5.5	0.8
2	N	57	5.5	1.0

Figure 35. Dimensionless downstream displacement of a liquid jet for Test 1 and Test 2.

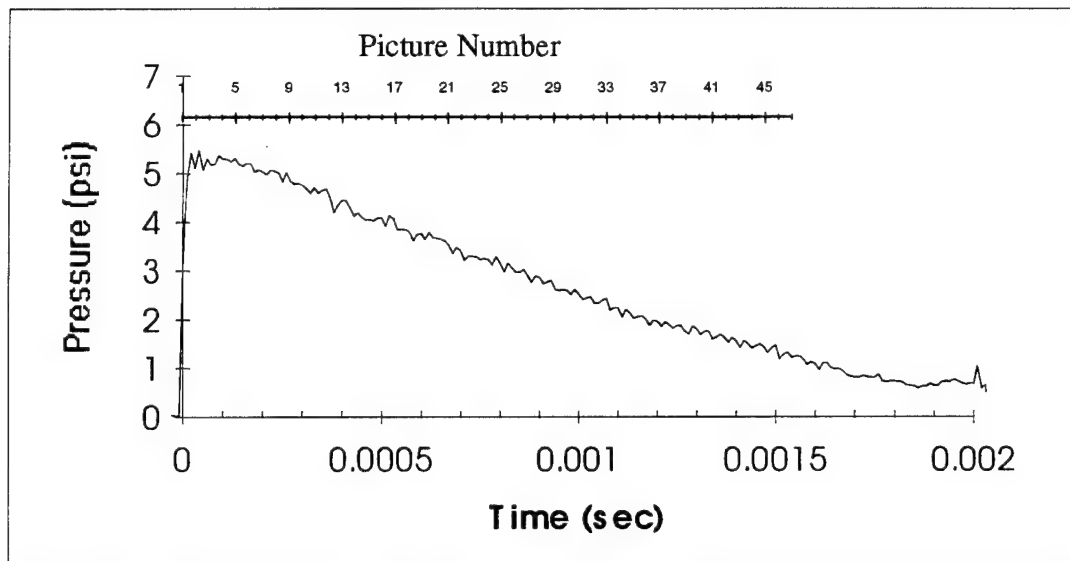
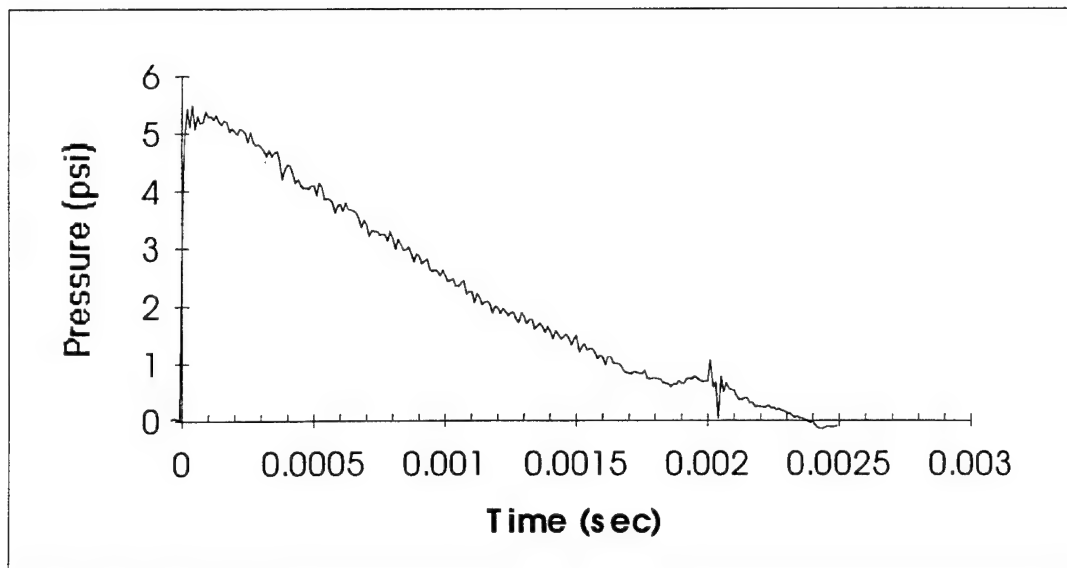


Figure 36. Pressure Time History for Test 4 (top) full duration (bottom) 2.0 msec duration

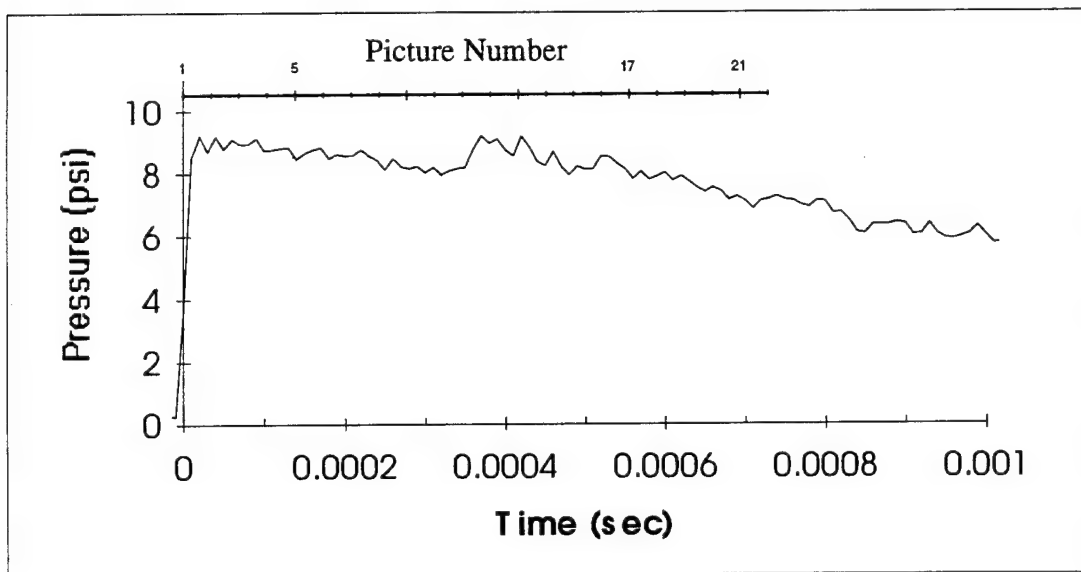
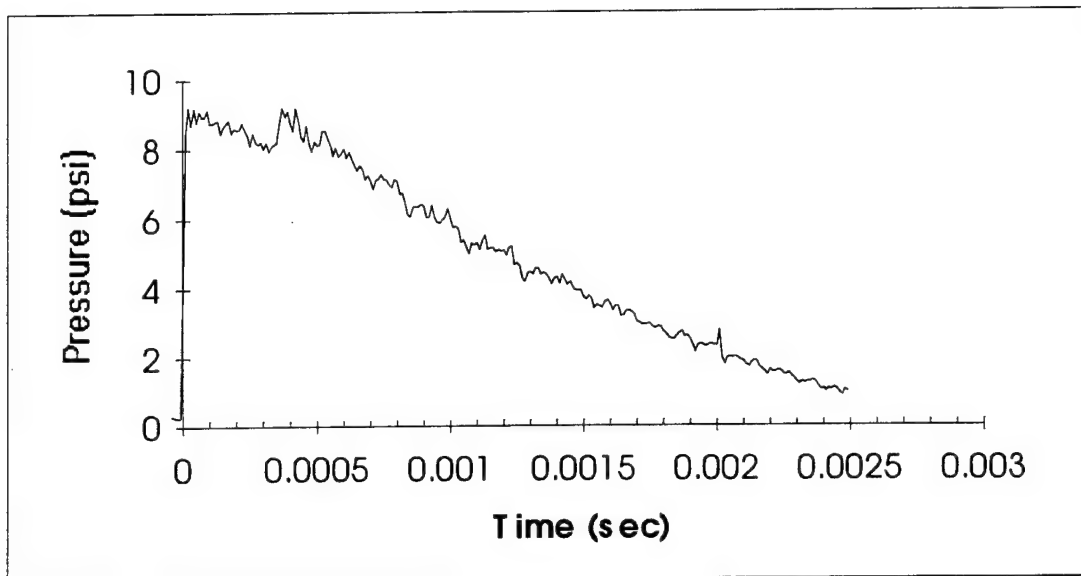


Figure 37. Pressure Time History for Test 5 (top) full duration (bottom) 1.0 msec duration

In summary, higher strength shock waves displace the liquid jet faster than the lower strength waves. This was found to be independent of wave type. However, higher strength shock displaced the jet so rapidly that the jet did not respond to the decelerating gas flow. In lower strength shocks, the jet displaced more slowly, allowing it to decelerate in the decaying gas flow.

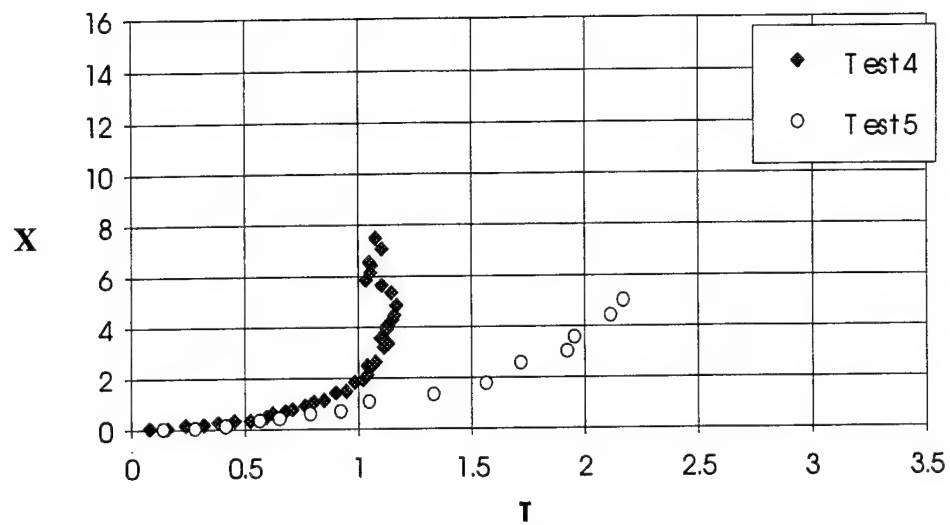
5.4.2 Effect of Jet Diameter

Tests 3 and 4 were compared with each other to study the effect of jet displacement with a change in jet diameter. Tests 3 and 4 were both a 38% N-wave of 2.3 ms wave duration (Figures 22 and 26). However, Test 3 was conducted with a 1.04 mm and Test 4 was with a 1.41 mm jet diameter. A comparison of the jet breakup sequence for Tests 3 and 4 in Figures 18 and 19, respectively, illustrates that the larger jet diameter causes a slower displacement rate, and therefore a longer observation time (by 400 μ s). During this additional time the jet decelerated more. Figure 44 shows the displacement plot for Tests 3 and 4. The additional decrease of pressure in Test 4 contributed to a lower value of T due to the lower velocity and density of the gas flow. The values of X and T decrease with larger diameter jets. Therefore, the smaller diameter jet (1.04 mm) in Test 3 would result in a larger value of X and T. This explains the "stretching" of the plot for Test 3. In experiments with square waves the similar observation was found. In the displacement plots for Tests 6 and 8 (Appendix B) it is shown that the smaller jet diameter will displace from the injector quicker than a larger diameter jet. However, in these experiments there is no decay in gas flow velocity.

In summary, the larger the jet diameter, the more resistant it is to displacement. As a result, larger diameter jets, in a decaying gas flow, respond more to this negative acceleration than smaller diameter jets.

5.5 Surface Wave Formation

Before the passage of a shock, the liquid jet is a steady, circular, coherent column. After passage of the shock and the onset of a high momentum gas flow, axial waves develop along the surface of the jet column and propagate along the plume with increasing amplitude. The plume curves downstream, depending on the liquid/gas dynamic pressure ratio (due to the aerodynamic drag) and eventually fractures at the trough of a high-amplitude wave. Aerodynamic forces quickly decompose the liquid fragment. The spray then becomes atomized within a short distance.



Test	Wave Type	Strength (%)	Duration (ms)	Diameter (mm)
4	N	37	2.3	1.41
5	N	62	2.3	1.41

Figure 38. Dimensionless downstream displacement of a liquid jet for Test 4 and Test 5.

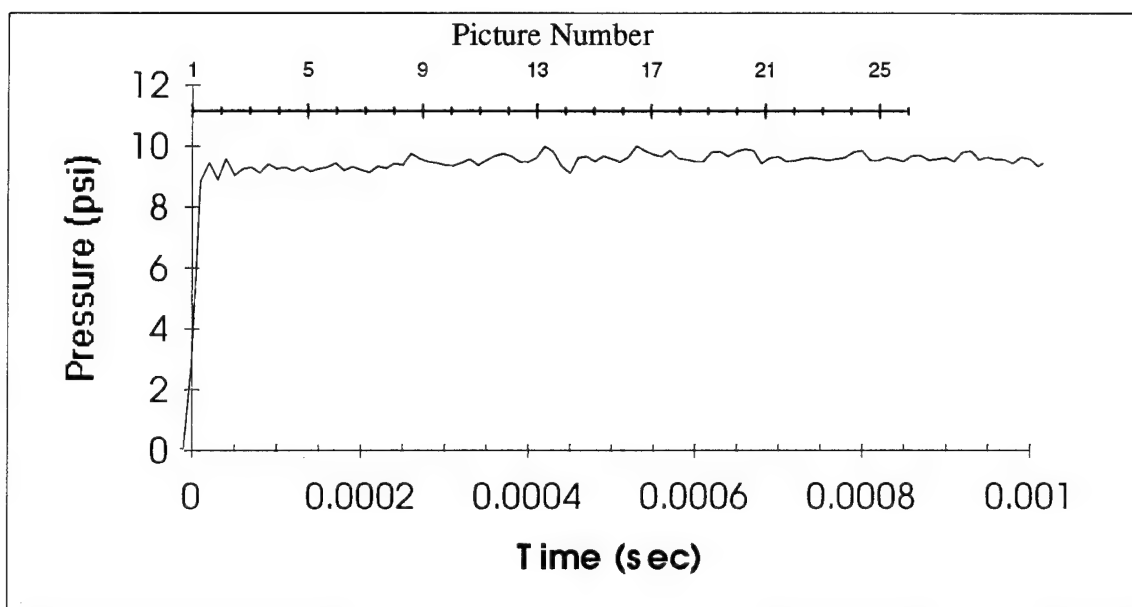
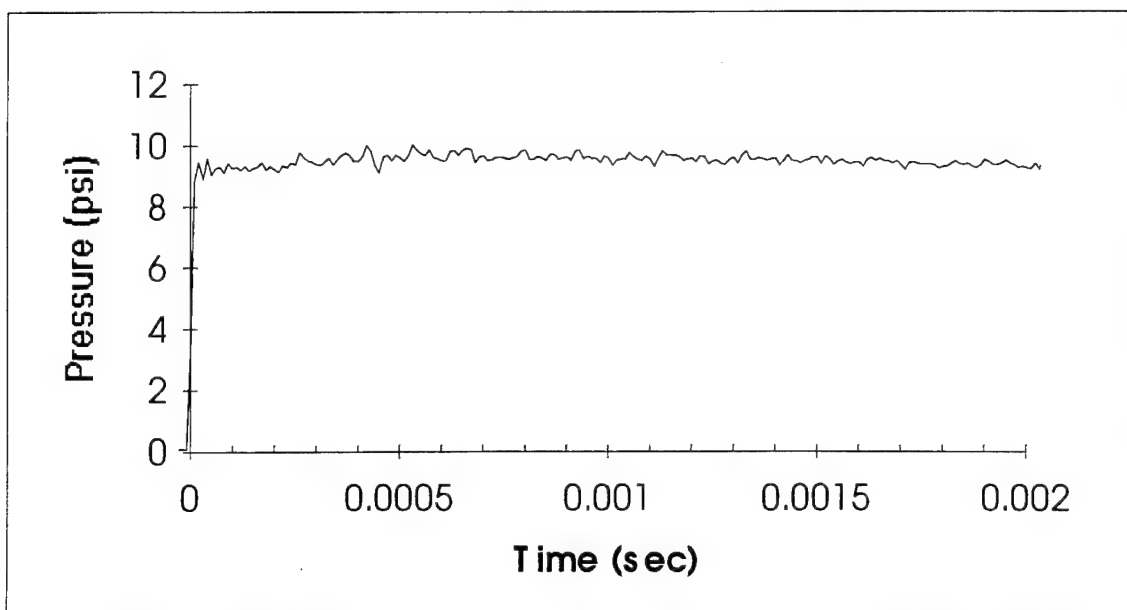
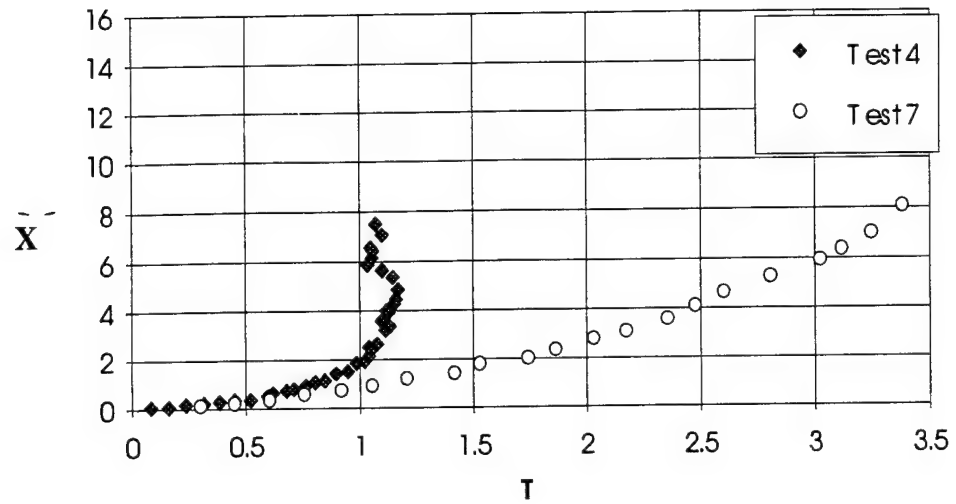


Figure 39. Pressure Time History for Test 7 (top) full duration (bottom) 1.0 msec duration



Test	Wave Type	Strength (%)	Duration (ms)	Diameter (mm)
4	N	37	2.3	1.41
7	S	65	infinite	1.41

Figure 40. Dimensionless downstream displacement of a liquid jet for Test 4 and Test 7.

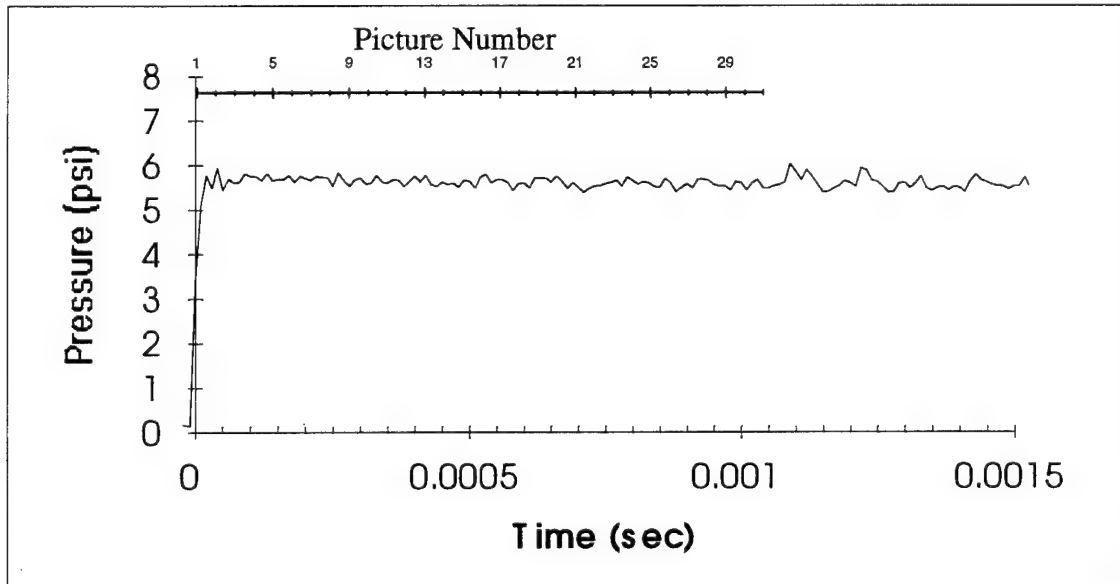
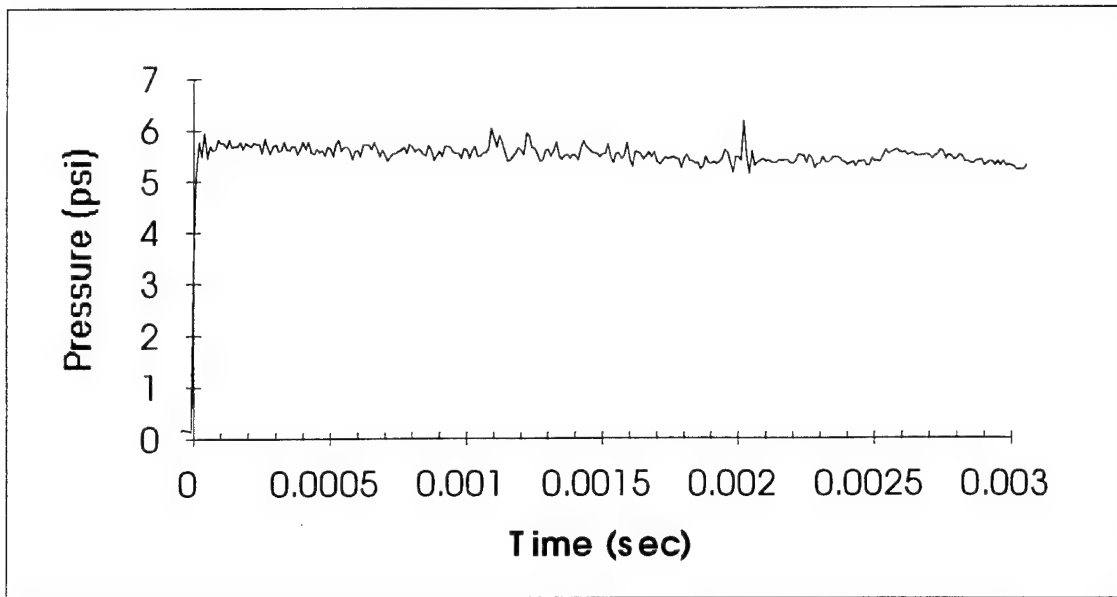


Figure 41. Pressure Time History for Test 8 (top) full duration (bottom) 1.5 msec duration

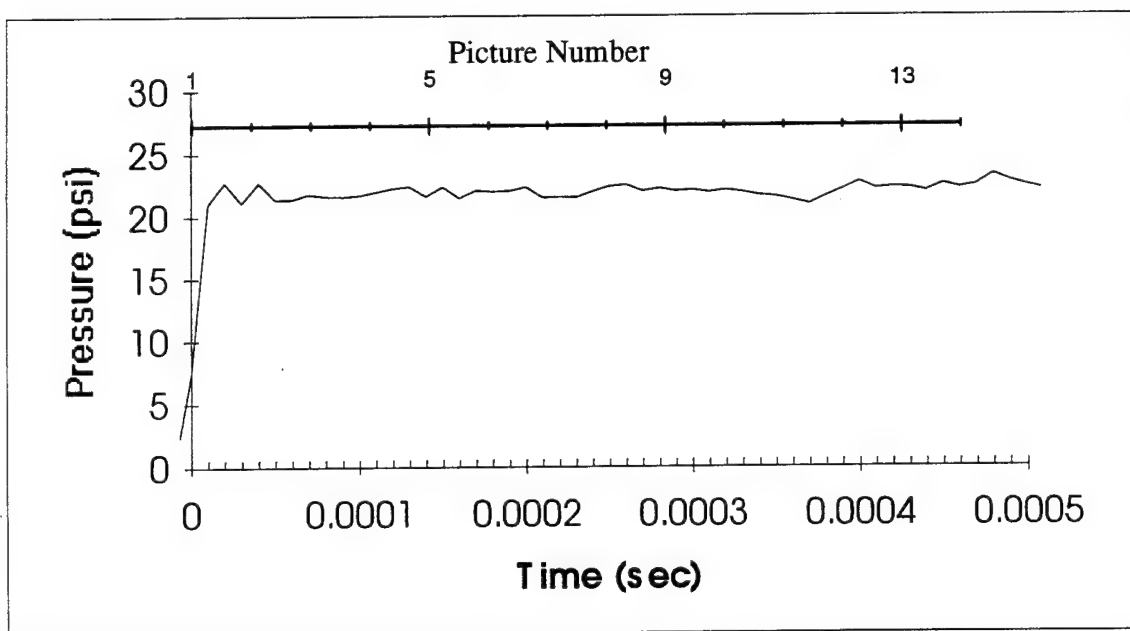
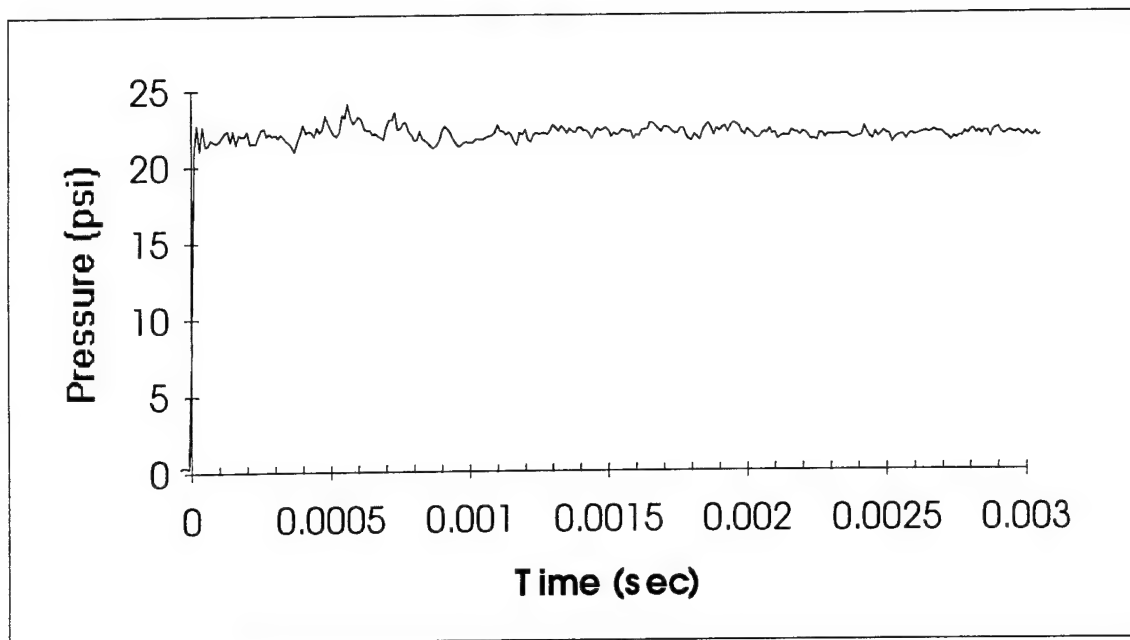
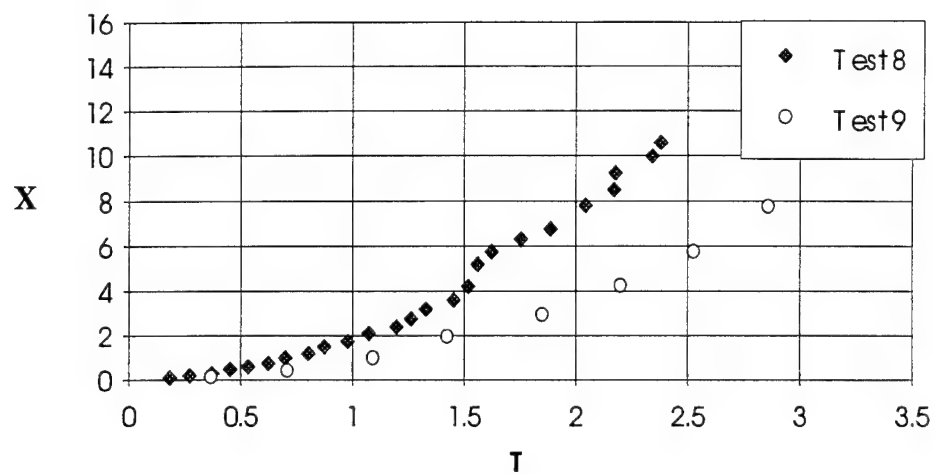
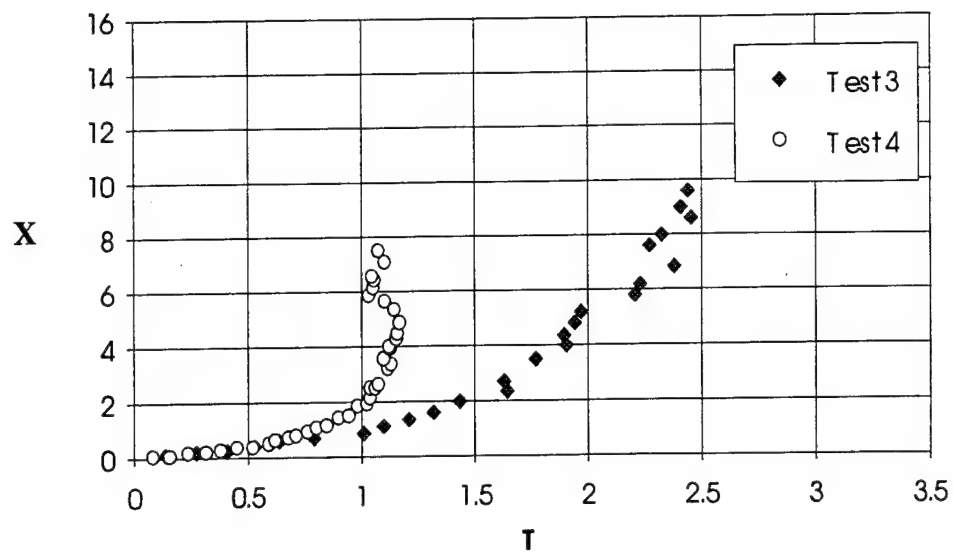


Figure 42 . Pressure Time History for Test 9 (top) full duration (bottom) 0.5 msec duration



Test	Wave Type	Strength (%)	Duration (ms)	Diameter (mm)
8	S	39	infinite	1.04
9	S	254	infinite	1.04

Figure 43. Dimensionless downstream displacement of a liquid jet for Test 8 and Test 9.



Test	Wave Type	Strength (%)	Duration (ms)	Diameter (mm)
3	N	38	2.3	1.04
4	N	38	2.3	1.41

Figure 44. Dimensionless downstream displacement of a liquid jet for Test 3 and Test 4.

The wavelength and maximum amplitude of the surface waves observed for all the tests conducted are documented in Table 4. A plot of surface wave amplitude as a function of liquid/gas dynamic pressure ratio for Tests 4, 5, 6, and 9 is shown in Figure 45. The surface wave amplitudes for Tests 4, 5, 6, and 9 were measured from the jet breakup images in Figures 19, 20, 11, and 14, respectively. The plot illustrates that, with an increase in dynamic pressure ratio, the amplitude of the surface waves reduces, for $q < 0.002$. These results are similar to those found by Schetz and Padhye (1977) who conducted studies at lower gas momentum flows. They also found that the wavelength of surface waves also reduces with increasing dynamic pressure ratio. However, no solid evidence for this was found in this present investigation.

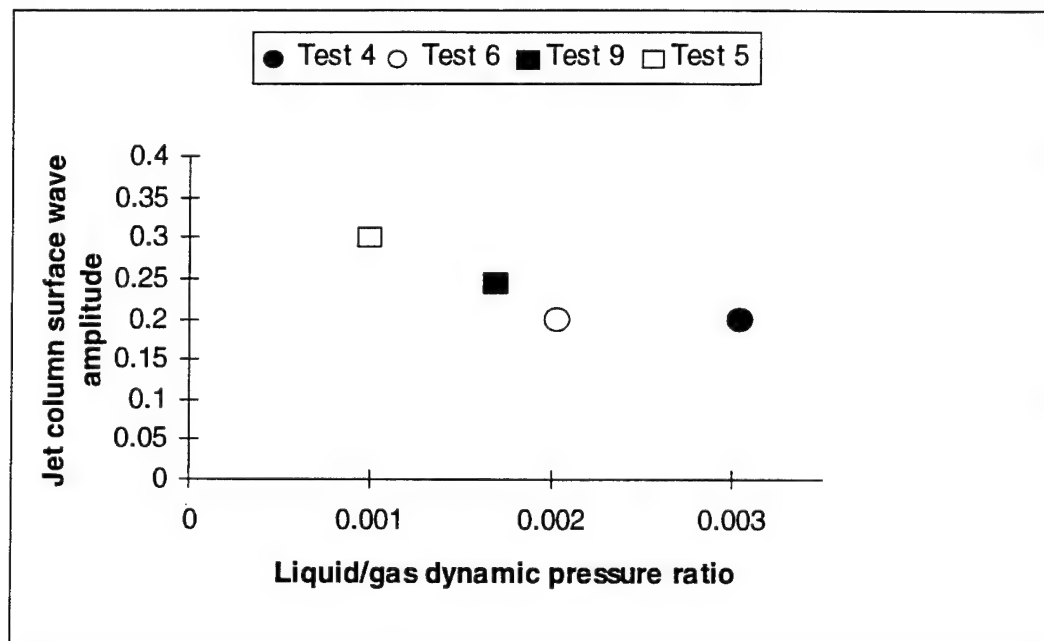


Figure 45. Jet surface wave amplitude vs liquid/gas dynamic pressure ratio.

6.0 SUMMARY, AND CONCLUSIONS

6.1 Summary

A fast-response imaging and diagnostic technique has been utilized to investigate the primary mechanism of breakup of a liquid jet behind a pressure pulse as it pertains to the evolution and development of combustion instability in liquid rocket engines. The study utilized high speed cinematography to delineate the primary atomization of a liquid jet under subcritical conditions. A test matrix was followed that explores operating conditions which best match SSME operating conditions. Time-sequenced still images verified good shock repeatability.

The results show that the flow behind a shock wave moving transverse to the liquid jet causes disintegration to occur simultaneously at all points along its length. The liquid initially responds to the high speed gas flow due to the external pressure distribution surrounding the cylindrical jet. The flow around the jet acts like flow around a solid cylinder. The jet then flattens and, at the edges of the flattened jet, drops and ligaments are torn off by the combined action of the tangential stress and surface tension.

From the images, the following measurements were made: the time required for jet breakup, jet displacement from the injector, and the droplet diameter.

Two wave types were explored: A square wave induced breakup, and an N-wave induced breakup. In addition, variation in the following parameters was explored:

- Shock wave strength
- Jet diameter

6.1.1 Square Wave Induced Breakup

The square wave produced a relatively constant pressure (hence a constant gas velocity) during the time frame the images were captured. Images indicate that ligament formation occurs only after the jet has distorted to an ellipsoidal shape. As the jet continues to deform, droplets are stripped away from the outer edge of the liquid core. Once the jet has flattened to a liquid sheet, displacement from the injector occurs. Surface waves are formed along the sheet which induce subsequent breakup further downstream. During the entire ligament/sheet formation process, drops are stripped away and are entrained in the gas flow. The average sizes of drops for Tests 1 and 2 were 30 to 50 μm .

The jet displacement behind the square wave was nondimensionalized as a function of $T = \frac{t V_g}{D_j} \sqrt{\frac{\rho_g}{\rho_j}}$. Comparison of this result with Reinecke's (1978) dimensionless jet displacement data, for low gas momentum flows (Test 8), reveals no similarity to the parabolic least-square regression ($X=0.8T^2$) obtained from their results. The difference is attributed to the fact that Reinecke's data used a general value of 7.0 for K, in Eq. 2.3, for Weber number greater than 600. However, Test 8 had a value of 4.5 for K and Weber number of 700. Although, each test in the present study resulted in a different displacement plot, the plots for Tests 6, 7, and 9 are generally similar to the parabolic least-square regression, indicating better agreement at higher Weber numbers.

From the nondimensional value of jet breakup up, typical values of K and T for Weber numbers above 600 are 6.40 and 5.40, respectively. These values are similar to those found by Reinecke ($K = 7.0$ and $T_j = 5.85$) for Weber numbers above 500.

The effect of jet diameter on displacement was also analyzed. It was found that smaller diameter jets accelerate with the gas flow much quicker than the larger diameter jets. Furthermore, this rapid displacement decreases the observation time for smaller

diameter jets. Hence, the displacement of the jet could be measured only before the gas flow velocity had an opportunity to decay. In some cases, the gas velocity for such experiments was somewhat similar to those for equal strength square waves. Larger jet diameters had a higher resistance to the gas flow. Therefore, the displacement rate was smaller and, by the time the last image was captured, the jet experienced the decelerating gas flow.

The surface wave formation on the liquid jet surface was analyzed as well. It was found that with an increase in liquid/gas dynamic pressure ratio (q), the surface wave amplitude decreased. This result is similar to that found by Schetz and Padhye (1977). They observed that with an increase in q , the amplitude and wavelength of surface waves were reduced. There was no evidence of wavelength reduction with increasing q in this investigation, which evaluated higher gas momentum flows.

The general atomization characteristics of the jet were observed qualitatively. It was apparent that high Weber and Reynolds number gas flows produced finer droplets in the atomization process. A good example of this is illustrated in the breakup sequence for the 254% wave (Figure 14). The value of the Weber and Reynolds number for this test are an one order of magnitude lower than that found in the SSME. This indicates that in actual SSME rocket conditions, jet breakup occurs faster than that depicted in Figure 14.

6.1.2 N-Wave Induced Breakup

The breakup images indicate that the atomization controlling step is identical to that behind the step wave. The same physics applies to both step and N-wave induced breakup. For the 34% wave it was shown that ligaments strip away from the outer edge of the deformed liquid and drops are later produced and entrained in the gas flow. The bulk liquid experienced displacement from the injector after the liquid flattened to a thin sheet. The 57% wave illustrated a much faster atomization rate than the 34% wave. In the case of ligament and sheet formation and also jet displacement, the 57% wave required half the time the 34% wave required to accomplish the processes. This was also shown in the drift rate between these two cases.

The result of the nondimensional displacement of the liquid jet reveals that the liquid jet, depending on the observation time, decelerates with the decaying gas velocity and density. The displacement plots for N-waves generally show a steeper slope than the square wave results. This is attributed to the fact that the value of T is declining with time, due to the decreasing gas velocity and density. Hence, a steeper slope is generated. Qualitative analysis from the jet breakup sequence of images for the N-wave and square wave experiments delineate this lower rate of displacement for the N-wave.

The analysis on the effect of jet diameter on displacement for N-wave experiments shows similarity with the results obtained for the square wave experiments; in that smaller diameter jets accelerate with the gas flow much quicker than the larger diameter jets.

The atomization of the jet was similar to that found for the square waves. Finer droplets were generated in high Weber and Reynolds number gas flows. In actual rocket engine conditions, the Weber and Reynolds number are much higher than the values in this investigation. This implies that jet breakup occurs very rapidly - much like that found in Figure 38. In these extreme conditions, the jet may shatter before the deceleration of the gas flow is realized behind an N-wave. The issue then becomes "how do the drops that are formed from the jet core react under a decelerating flow field?"

6.1.3 Drop Size Measurements

Drop diameters were measured for Test 1 and 2 by analyzing the still images. For Tests 3-9 the images were enlarged by a factor of 70 and drop sizes were measured with a scale. The droplet diameter determination obtained here has validity only as a determination of the sizes of initial droplets for each test. For two different injector diameters it was found that the average drop size decreased with airstream velocity. The larger diameter jet (1.41 mm) produced the larger drop sizes (on the order of 50 μm). The smallest detected drops (15 μm) were found for the case where the gas velocity was 300 m/s and the jet diameter was 1.04 mm.

6.2 Conclusions

- N-waves decelerate jet displacement and the jet breakup time - unless very rapid breakup occurs.
- Faster atomization rates and jet displacements occurred behind a step wave.
- Jet displacement rate increases with shock wave strength.
- Smaller diameter jets displace faster from the injector than larger diameter jets.
- Surface wave amplitude decreases with increasing liquid/gas dynamic pressure ratio.
- Drop size decreases with increasing shock wave strength.
- Drop size increases with liquid jet diameter.
- Shock interaction with the primary atomization process produces a substantial change to the breakup mechanism and serves, as a result, a principal candidate for the promotion and acceleration of rocket engine instability

6.3 Recommendations for Future Work

Although these experiments provide insight on the breakup of a liquid jet, several steps can be taken to improve the understanding. The following is a list of recommendations for future work:

- Conduct experiments at elevated pressures in the driven section of the shock tube.
- Liquids with lower surface tension and viscosity should be used to more accurately simulate liquid oxygen. This will also increase the Weber number and Reynolds number to levels closer to SSME values.

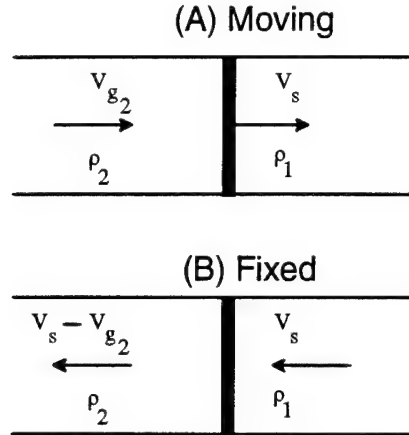
- Supercritical simulant liquids should be used to evaluate the breakup process of a liquid jet in a supercritical environment. This can be done by injecting the liquid at supercritical pressures but subcritical temperatures into the shock tube which is at supercritical pressure and temperature. The jet will then experience supercritical heating as it penetrates into the bore of the shock tube.
- Experiments covering the entire test matrix would provide the most useful information. Specifically, experiments that cover the entire range of the important fluid parameters.
- A laser sheet in the plane of the jet axis can capture images of the breakup at the focus plane of the camera. Thus, drops that are formed can easily be seen on the image plane. Shadowgraphs will capture images of drops that are and are not in focus, making drop size analysis less difficult.
- Scanning of the image and the implementation of an image analysis software will improve the analysis of the breakup and drop formation - provided that the resolution of the scan can resolve the smallest droplets.

7.0 REFERENCES

- Buffum, F.G., Williams, F.A., "Liquid Jet Oscillation in Transverse Acoustic Fields," AIAA Paper 67-473. AIAA 3rd Propulsion Joint Specialist Conference, Washington, D.C. (July 17-21, 1967).
- Clark, B.J. "Propellant Vaporization as a Criterion for Rocket Engine Design: Experimental Effect of Combustor Length, Throat Diameter, Injection Velocity, and Pressure on Rocket Combustion Efficiency," NASA TN D-258, 1960.
- Clark, B.J., "Breakup of a Liquid Jet in a Transverse Flow of Gas," NASA TN D-2424, 1964.
- Cox, G.B. (1990) "The Liquid Stability Mechanisms Program," 27th JANNAF Combustion Meeting, Warren Air Force Base, Cheyenne, WY, Nov. 1990, CPIA-573, Vol.2, pp. 51-68.
- Harrje, D.T. and Reardon, eds. (1972) "Liquid Propellant Rocket Combustion Instability," NASA SP-194, US Government Printing Office, Washington, DC, 1972.
- Heidmann, M.F., and Groeneweg, J.F., "Dynamic Response of Liquid Jet Breakup," AIAA Journal, vol. 6, No. 10, 1968 pp. 2033-2035.
- Huynh, C., Ghafourian, A., Mahalingham, S., and Daily, J.W., "Dynamic Behavior of Atomizing Jets in Liquid Rocket Engines," WSS-CI 92-16.
- Jensen, R.J., "A Summary of the JANNAF Workshop on Liquid Rocket Engine Combustion Driven Instability Mechanisms," 26th JANNAF Combustion Meeting, Pasadena, California, October 1989, CPIA-529, Vol.2, pp. 273-288.
- John, J.E.A., 1984, "Gas Dynamics," Allyn and Bacon.
- Kush, E. and Schetz, J., "Liquid Jet Injection Into a Supersonic Flow," AIAA Paper 72-1180, New Orleans, La., Nov. 1972.
- Lamb, H. 1925 "The Dynamical Theory of Sound," Dover
- Levine, R.S., "Experimental Status of High Frequency Liquid Rocket Combustion Instability," Tenth Symposium (International) on Combustion, William and Wilkins 1965, pp. 1083-1099.
- Morrell, G., "Rate of Liquid Jet Breakup by a Transverse Shock Wave," NASA TP3-63, 1963.
- Morrell, G., "Critical Conditions for Drop and Jet Shattering," NASA TN D-677, 1961.
- Reichenback, R. and Horn, K., "Investigation of Injectant Properties on Jet Penetration in a Supersonic Stream," AIAA Journal, Vol. 9, March 1971, pp. 469-472.
- Reinecke, W.G., "Drop Breakup and Liquid Jet Penetration," AIAA Journal Vol. 16, No.6, March 1978.
- Schetz, J. A., and Padhye, A., "Penetration and Breakup of Liquids in Subsonic Airstreams," AIAA Journal Vol. 15, No. 10, October 1977.
- Sitkei, G., "Contribution to the Theory of Jet Atomization," NASA TT F-129, 1963.
- Sutton, G., "Rocket Propulsion Elements," 1986.
- Temkin, S., and Mehta, H.K., "Droplet Drag in an Accelerating and Decelerating Flow," Journal of Fluid Mechanics (1982), Vol. 116, pp. 297-313.

Appendix A: Test Matrix Calculations

1. Select a LOX simulant with similar surface tension and viscosity.
2. Select a range of shock strengths (P_2/P_1).
3. For each shock strength value calculate gas flow velocity behind the shock, the shock velocity, gas density ratio across the shock, and the diaphragm pressure ratio using the equation of motion for a normal shock moving into a gas at rest (John, 1984)



The equation of motion for a normal shock moving rightward into a gas at rest (Figure A) is written. To reduce the problem to one of steady flow, the shock is fixed (Figure B).

It follows from standard shock relations that the gas velocity behind the shock is

$$V_{g2} = \frac{a_1 \left(\frac{p_2}{p_1} - 1 \right)}{\gamma \sqrt{1 + \frac{\gamma + 1}{2\gamma} \left(\frac{p_2}{p_1} - 1 \right)}} \quad \text{A.1}$$

The shock velocity, V_s , is solved for using the expression in A.1.:

$$V_s = \frac{V_{g2}}{4} (\gamma + 1) \pm \sqrt{\frac{V_{g2}^2 (\gamma + 1)^2}{16} + a_1^2} \quad \text{A.2}$$

It follows that the density ratio across the shock is:

$$\frac{\rho_2}{\rho_1} = \frac{V_s}{V_s - V_{g2}} \quad \text{A.3}$$

The diaphragm pressure ratio is calculated, considering the speed of sound in the driver section and the driven section of the shock tube is the same. Setting $V_{g2} = V_{g3}$ and $p_2 = p_3$, the result is:

$$\frac{p_4}{p_1} = \frac{p_2}{p_1} \left[1 - \frac{\gamma - 1}{2\gamma} \frac{\left(\frac{p_2}{p_1} - 1 \right)}{\sqrt{1 + \frac{\gamma + 1}{2\gamma} \left(\frac{p_2}{p_1} - 1 \right)}} \right]^{\frac{-2\gamma}{\gamma - 1}} \quad \text{A.4}$$

4. By equating the We equation with the range of We values present in the LRE we determine, for each shock strength, a range of initial gas density in the driven section. Since there is a low to high range of We and V_{g2} and σ_l are fixed values for a single shock strength value and simulant, respectively, a low to high range of ρ_2 is calculated. This is denoted on the spreadsheet as 'D1(low)' and 'D1(hi)'. Using the gas density ratio calculated in step 3 the gas density in the driven section of the shock tube, ρ_1 , is calculated.

$$Weber = \frac{\rho_2 V_2^2 D}{\sigma_l} = 5.96 \times 10^4 \rightarrow 5.64 \times 10^6$$

$$\rho_1 = \frac{\sigma_l}{V_2^2 D} \left(5.96 \times 10^4 \rightarrow 5.64 \times 10^6 \right) \cdot \frac{1}{\left(\frac{\rho_2}{\rho_1} \right)}$$

5. Using the ideal gas law equation the pressure required to obtain ρ_1 in the driven section is then obtained. Again, due to the low to high range of gas densities a range of low to high driven section pressures are also obtained.

$$p_1 = \frac{\rho_1}{RT}$$

6. In step 3 the diaphragm pressure ratio, (p_4/p_1) , was calculated for each shock strength value. Now that p_1 is known from the previous step, p_4 is calculated from the ratio value. A low to high range of p_4 is also obtained. $p_4 = p_1 \left(\frac{p_4}{p_1} \right)$

7. The gaseous Reynolds Number (Re) can be calculated using the gas properties obtained in the spreadsheet. In these experiments air is used as the shock tube gas. A low to high range of Re is obtained due to its dependence on ρ_{g2} .

$$Re = \frac{\rho_2 V_2 D}{\mu_2} = 1.16 \times 10^5 \rightarrow 1.46 \times 10^6$$

Behind the shock wave there is a temperature rise in the gas. This temperature variation causes a change in the gas viscosity. Therefore, the viscosity term is a function of shock strength.

8. The liquid/chamber-gas density ratio is calculated using the density of the gas in front of the shock wave (the initial driven section density ρ_1). Assuming the liquid density is constant the only variance in the ratio is due to range of ρ_1 .

$$\text{Liquid / Chamber Density Ratio} = \frac{\rho_l}{\rho_1}$$

Let τ = liq/gas density ratio $\frac{\rho_l}{\rho_1}$. Assuming liquid density is constant for every test condition, then:

$$\tau_{\text{low}} = \rho_l/\rho_{g1\text{high}} \text{ and } \tau_{\text{high}} = \rho_l/\rho_{g1\text{low}}$$

9. In this LRE the dynamic pressure ratio ranges from 0.07 to 6.64. The equation for liquid/gas dynamic pressure ratio is given as: $[\rho_l V_l^2 / \rho_{g2} V_{g2}^2]$. Knowing the liquid density, gas properties, and the range of dynamic pressure ratio values, we calculate a range of low to high jet velocity, V_l , that would result in matching the liquid injection condition to simulate LRE conditions. It is found that the lowest value of jet velocity occurs when the 0.0374 is used as the dynamic pressure ratio and $\rho_{g2\text{low}}$ is used as the gas density. Similarly, the highest value of V_l is calculated using the extreme value of the above parameters.

$$q = \frac{\rho_{\text{liq}} V_{\text{liq}}^2}{\rho_{g2} V_{g2}^2}$$

therefore,

$$V_{\text{liq,low}}^{\text{high}} = \sqrt{\frac{1}{\rho_{\text{liq}}} (q_{\text{low}}^{\text{high}}) \left(\frac{D_2}{D_1} D_{1\text{low}}^{\text{high}} \right) V_{g2}^2}$$

10. Calculate the viscosity ratio: $[v_l/v_{g2}]$. Since, $v = \mu/\rho$, the viscosity ratio can be expressed as $v_l/v_{g2} = [\mu_l \rho_{g2} / \mu_g \rho_l]$. Therefore, due to dependence on the range of ρ_{g2} , there will also be a low to high range of liquid/gas viscosity ratio.
11. The liquid Reynolds Number ($Re = \rho_l V_l / \mu_l$) is also calculated. Again due to a low and high range of liquid velocity, a range of Reynolds number would have to be calculated.

Examples of a test matrix spreadsheet are shown in Table A.1 - A.4.

Table A.1. Test Matrix Spreadsheet for Methanol

[illegible]

Table A.2. Methanol Test Matrix Spreadsheet for Various Jet Diameters

If Given Section (P) is 1 Atmosphere									
Density $\rho = 1.181 \text{ kg/m}^3$									
Liquid = Methanol (1 mm at 1 m/s)									
P/P1	V _g (m/s)	W _g (m/s)	T _g (K)	#2	U ₂ /U ₁	P/P1	P4 (Pa)	D2 (kg/m ³)	Jet Diameter =
									1 mm
1.1	23.72	360.52	1.03	1.88E-05	1.07	1.21	17.81	1.30	3.23E-01
1.15	34.90	367.57	1.04	1.90E-05	1.10	1.33	19.50	1.36	7.32E+01
✓ 1.2	45.67	374.48	1.05	1.91E-05	1.14	1.45	21.27	1.42	1.31E+02
1.25	56.07	381.27	1.07	1.93E-05	1.17	1.57	23.14	1.48	2.05E+02
1.3	66.13	387.94	1.08	1.94E-05	1.21	1.71	25.10	1.54	2.97E+02
1.35	75.87	394.50	1.09	1.96E-05	1.24	1.85	27.16	1.59	4.06E+02
✓ 1.4	85.31	400.95	1.10	1.97E-05	1.27	1.99	29.32	1.65	5.32E+02
1.45	94.48	407.30	1.11	1.99E-05	1.30	2.15	31.58	1.71	6.76E+02
1.5	103.39	413.55	1.13	2.00E-05	1.33	2.31	33.94	1.77	8.38E+02
1.55	112.06	419.71	1.14	2.01E-05	1.36	2.48	36.41	1.83	1.02E+03
1.6	120.50	425.77	1.15	2.03E-05	1.39	2.65	38.99	1.89	1.21E+03
✓ 1.65	128.74	431.76	1.16	2.04E-05	1.42	2.84	41.68	1.95	1.43E+03
1.7	136.77	437.66	1.17	2.05E-05	1.45	3.03	44.48	2.01	1.66E+03
1.75	144.61	443.44	1.18	2.06E-05	1.48	3.22	47.40	2.07	1.91E+03
1.8	152.28	449.23	1.19	2.08E-05	1.51	3.43	50.43	2.13	2.18E+03
1.85	159.78	454.90	1.20	2.09E-05	1.54	3.65	53.59	2.18	2.47E+03
1.9	167.12	460.51	1.21	2.10E-05	1.57	3.87	56.88	2.24	2.77E+03
1.95	174.31	466.05	1.22	2.11E-05	1.60	4.10	60.29	2.30	3.10E+03
2	181.35	471.52	1.23	2.13E-05	1.63	4.34	63.83	2.36	3.44E+03
2.1	195.04	482.28	1.25	2.15E-05	1.68	4.85	71.32	2.48	4.17E+03
2.2	208.23	492.80	1.27	2.17E-05	1.73	5.40	79.37	2.60	4.98E+03
2.3	220.96	503.10	1.29	2.20E-05	1.78	5.99	88.00	2.72	5.87E+03
2.4	233.27	513.20	1.31	2.22E-05	1.83	6.62	97.25	2.83	6.82E+03
2.5	245.20	523.10	1.33	2.24E-05	1.88	7.29	107.14	2.95	7.85E+03
✓ 2.6	256.78	532.82	1.35	2.27E-05	1.93	8.01	117.70	3.07	8.94E+03
2.7	268.03	542.36	1.37	2.29E-05	1.98	8.77	128.96	3.19	1.01E+04
2.8	278.97	551.74	1.38	2.31E-05	2.02	9.59	140.96	3.31	1.14E+04
2.9	289.63	560.97	1.40	2.33E-05	2.07	10.46	153.73	3.42	1.27E+04
3	300.02	570.04	1.42	2.36E-05	2.11	11.38	167.30	3.54	1.41E+04
3.1	310.16	578.97	1.44	2.38E-05	2.15	12.36	181.71	3.66	1.56E+04
✓ 3.2	320.07	587.76	1.46	2.40E-05	2.20	13.40	197.00	3.78	1.71E+04
3.3	329.76	596.43	1.48	2.42E-05	2.24	14.50	213.20	3.90	1.88E+04
3.4	339.24	604.97	1.49	2.44E-05	2.28	15.67	230.36	4.02	2.04E+04
3.5	348.52	613.39	1.51	2.47E-05	2.32	16.91	248.51	4.13	2.22E+04
3.6	357.62	621.70	1.53	2.49E-05	2.35	18.21	267.72	4.25	2.41E+04
✓ 3.7	366.54	629.90	1.55	2.51E-05	2.39	19.59	288.01	4.37	2.60E+04
3.8	375.29	637.99	1.56	2.53E-05	2.43	21.05	309.43	4.49	2.80E+04
3.9	383.88	645.98	1.58	2.55E-05	2.46	22.59	332.04	4.61	3.00E+04
4	392.33	653.88	1.60	2.57E-05	2.50	24.21	355.90	4.72	3.22E+04

Table A.3. Test Matrix Spreadsheet for Freon-22

[illegible]

If Driven Section (PI) is 74.7 pfa																																																																																																																																																																																																																																																																																																																																																																																				
Density = 14.02456 kg/m ³																																																																																																																																																																																																																																																																																																																																																																																				
Liquid = Freon-22 (1 m/s)																																																																																																																																																																																																																																																																																																																																																																																				
P/P1	V ₂ (m/s)	V ₁ (m/s)	T/P1 (K)	P/P1	Q2 (kg/m ³)	Jet Diameter =	1 mm	2 mm	3 mm	4.72 mm	10 mm	15 mm	20 mm	30 mm	40 mm	50 mm	60 mm	70 mm	80 mm	90 mm	100 mm	110 mm	120 mm	130 mm	140 mm	150 mm	160 mm	170 mm	180 mm	190 mm	200 mm	210 mm	220 mm	230 mm	240 mm	250 mm	260 mm	270 mm	280 mm	290 mm	300 mm	310 mm	320 mm	330 mm	340 mm	350 mm	360 mm	370 mm	380 mm	390 mm	400 mm	410 mm	420 mm	430 mm	440 mm	450 mm	460 mm	470 mm	480 mm	490 mm	500 mm	510 mm	520 mm	530 mm	540 mm	550 mm	560 mm	570 mm	580 mm	590 mm	600 mm	610 mm	620 mm	630 mm	640 mm	650 mm	660 mm	670 mm	680 mm	690 mm	700 mm	710 mm	720 mm	730 mm	740 mm	750 mm	760 mm	770 mm	780 mm	790 mm	800 mm	810 mm	820 mm	830 mm	840 mm	850 mm	860 mm	870 mm	880 mm	890 mm	900 mm	910 mm	920 mm	930 mm	940 mm	950 mm	960 mm	970 mm	980 mm	990 mm	1000 mm	1010 mm	1020 mm	1030 mm	1040 mm	1050 mm	1060 mm	1070 mm	1080 mm	1090 mm	1100 mm	1110 mm	1120 mm	1130 mm	1140 mm	1150 mm	1160 mm	1170 mm	1180 mm	1190 mm	1200 mm	1210 mm	1220 mm	1230 mm	1240 mm	1250 mm	1260 mm	1270 mm	1280 mm	1290 mm	1300 mm	1310 mm	1320 mm	1330 mm	1340 mm	1350 mm	1360 mm	1370 mm	1380 mm	1390 mm	1400 mm	1410 mm	1420 mm	1430 mm	1440 mm	1450 mm	1460 mm	1470 mm	1480 mm	1490 mm	1500 mm	1510 mm	1520 mm	1530 mm	1540 mm	1550 mm	1560 mm	1570 mm	1580 mm	1590 mm	1600 mm	1610 mm	1620 mm	1630 mm	1640 mm	1650 mm	1660 mm	1670 mm	1680 mm	1690 mm	1700 mm	1710 mm	1720 mm	1730 mm	1740 mm	1750 mm	1760 mm	1770 mm	1780 mm	1790 mm	1800 mm	1810 mm	1820 mm	1830 mm	1840 mm	1850 mm	1860 mm	1870 mm	1880 mm	1890 mm	1900 mm	1910 mm	1920 mm	1930 mm	1940 mm	1950 mm	1960 mm	1970 mm	1980 mm	1990 mm	2000 mm	2010 mm	2020 mm	2030 mm	2040 mm	2050 mm	2060 mm	2070 mm	2080 mm	2090 mm	2100 mm	2110 mm	2120 mm	2130 mm	2140 mm	2150 mm	2160 mm	2170 mm	2180 mm	2190 mm	2200 mm	2210 mm	2220 mm	2230 mm	2240 mm	2250 mm	2260 mm	2270 mm	2280 mm	2290 mm	2300 mm	2310 mm	2320 mm	2330 mm	2340 mm	2350 mm	2360 mm	2370 mm	2380 mm	2390 mm	2400 mm	2410 mm	2420 mm	2430 mm	2440 mm	2450 mm	2460 mm	2470 mm	2480 mm	2490 mm	2500 mm	2510 mm	2520 mm	2530 mm	2540 mm	2550 mm	2560 mm	2570 mm	2580 mm	2590 mm	2600 mm	2610 mm	2620 mm	2630 mm	2640 mm	2650 mm	2660 mm	2670 mm	2680 mm	2690 mm	2700 mm	2710 mm	2720 mm	2730 mm	2740 mm	2750 mm	2760 mm	2770 mm	2780 mm	2790 mm	2800 mm	2810 mm	2820 mm	2830 mm	2840 mm	2850 mm	2860 mm	2870 mm	2880 mm	2890 mm	2900 mm	2910 mm	2920 mm	2930 mm	2940 mm	2950 mm	2960 mm	2970 mm	2980 mm	2990 mm	3000 mm	3010 mm	3020 mm	3030 mm	3040 mm	3050 mm	3060 mm	3070 mm	3080 mm	3090 mm	3100 mm	3110 mm	3120 mm	3130 mm	3140 mm	3150 mm	3160 mm	3170 mm	3180 mm	3190 mm	3200 mm	3210 mm	3220 mm	3230 mm	3240 mm	3250 mm	3260 mm	3270 mm	3280 mm	3290 mm	3300 mm	3310 mm	3320 mm	3330 mm	3340 mm	3350 mm	3360 mm	3370 mm	3380 mm	3390 mm	3400 mm	3410 mm	3420 mm	3430 mm	3440 mm	3450 mm	3460 mm	3470 mm	3480 mm	3490 mm	3500 mm	3510 mm	3520 mm	3530 mm	3540 mm	3550 mm	3560 mm	3570 mm	3580 mm	3590 mm	3600 mm	3610 mm

Appendix B: Jet Displacement Plots

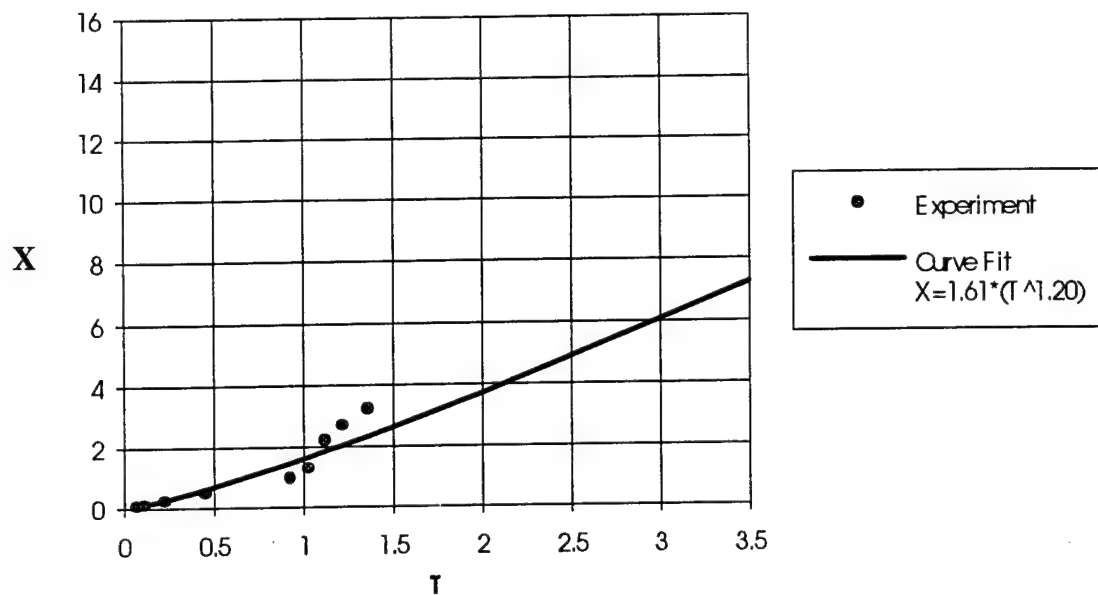


Figure B.1. Dimensionless downstream displacement of a liquid jet for Test 1

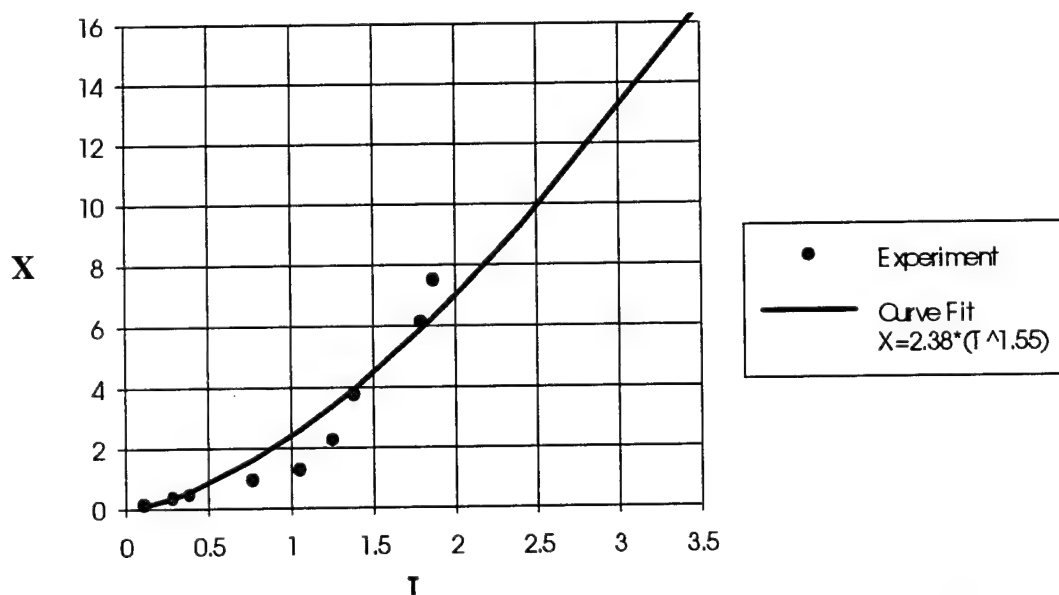


Figure B.2. Dimensionless downstream displacement of a liquid jet for Test 2.

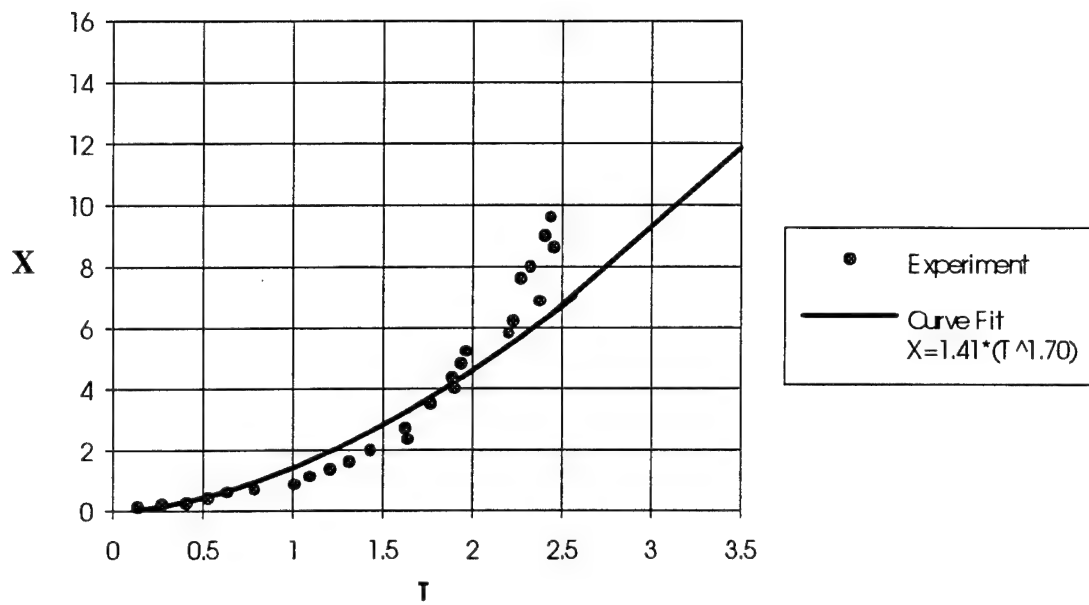


Figure B.3. Dimensionless downstream displacement of a liquid jet for Test 3.

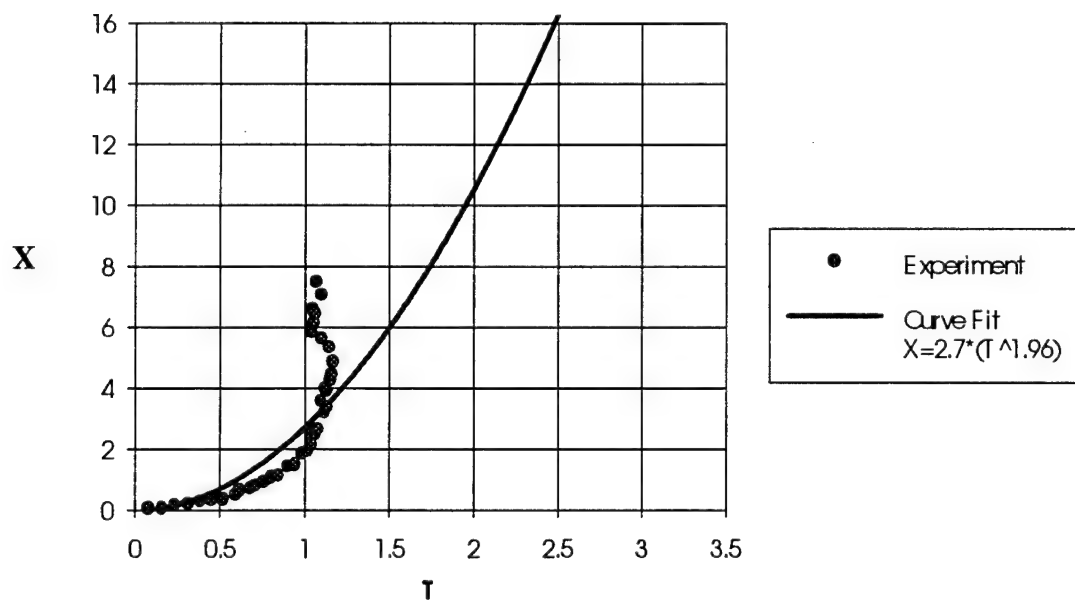


Figure B.4. Dimensionless downstream displacement of a liquid jet for Test 4.

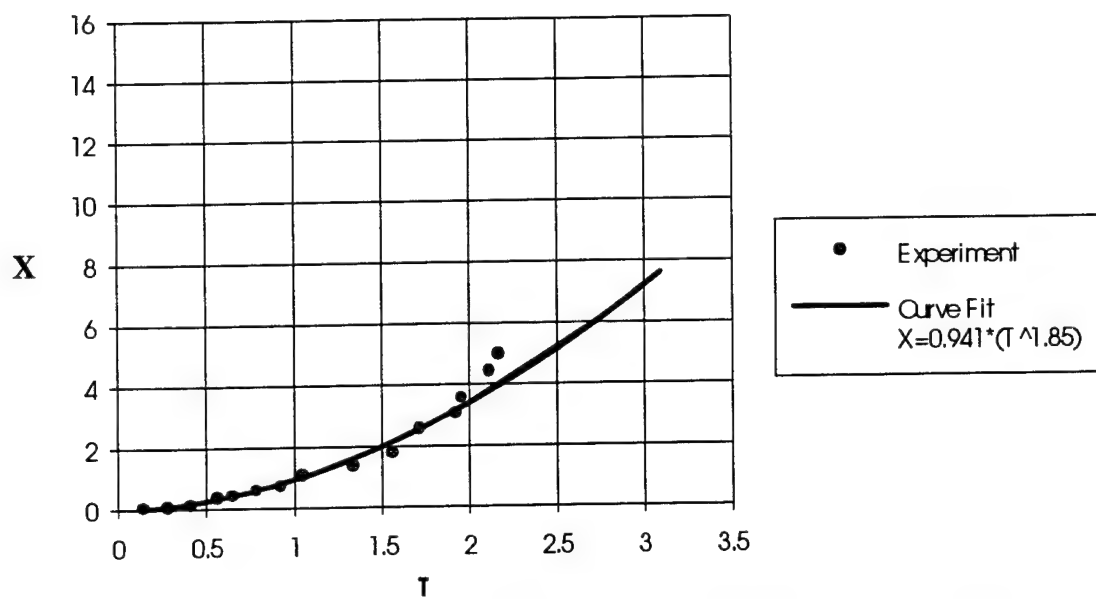


Figure B.5. Dimensionless downstream displacement of a liquid jet for Test 5.

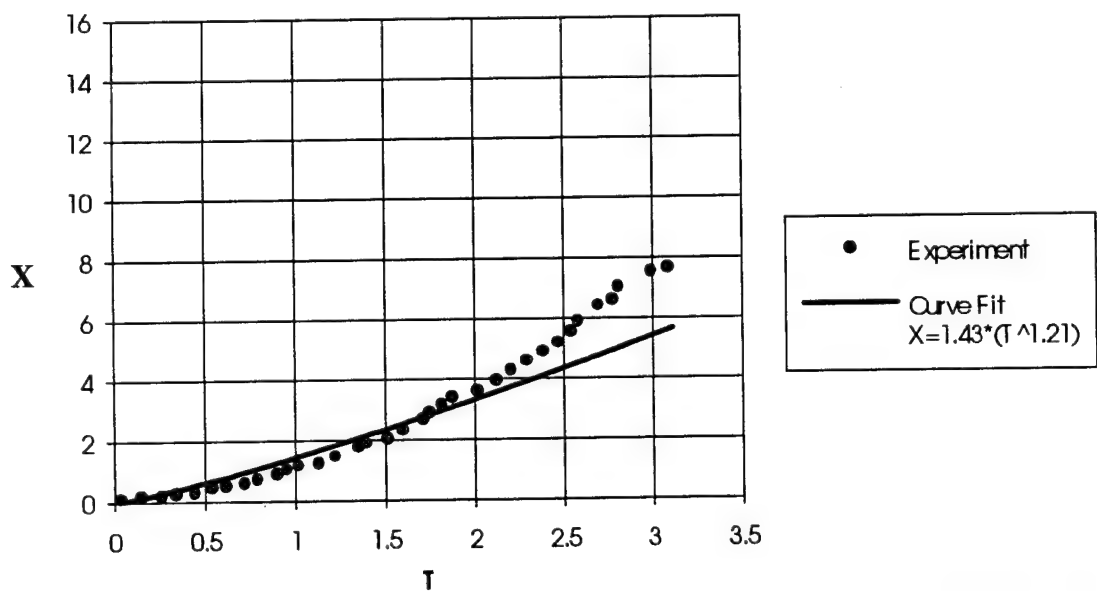
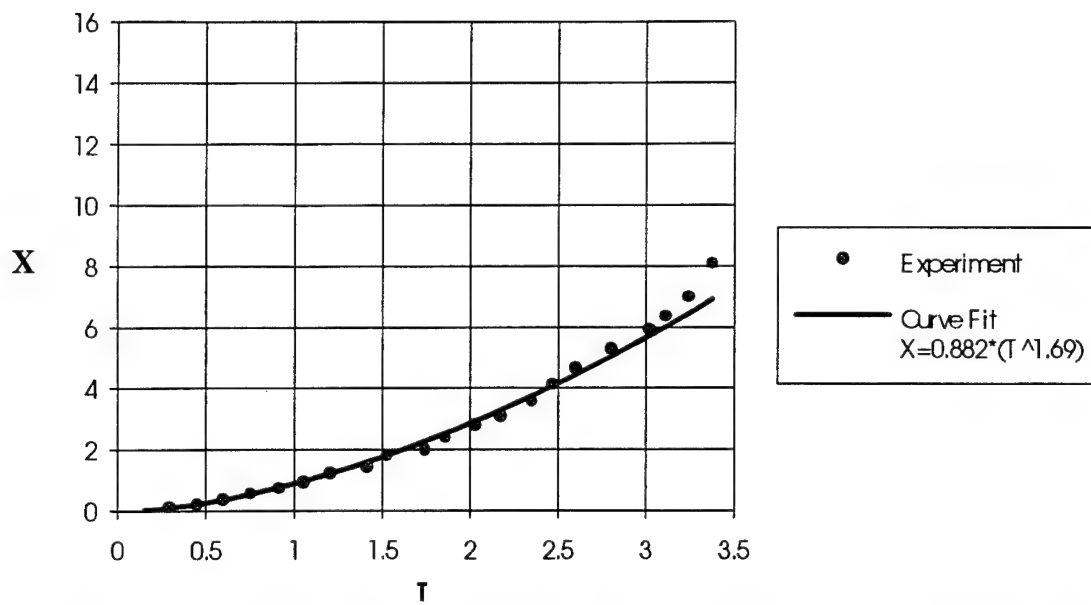
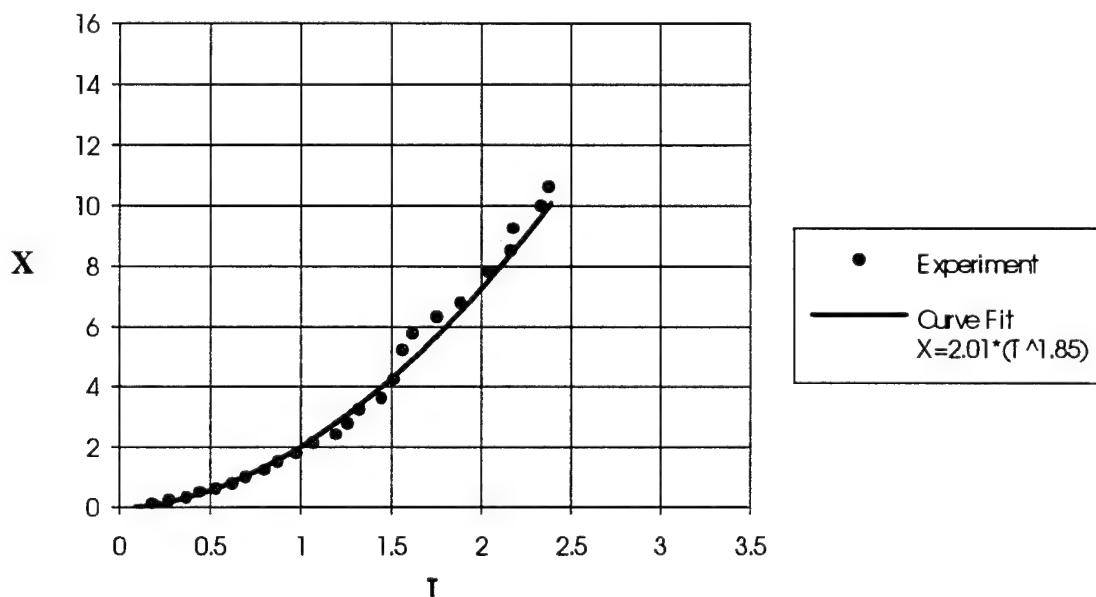


Figure B.6. Dimensionless downstream displacement of a liquid jet for Test 6.



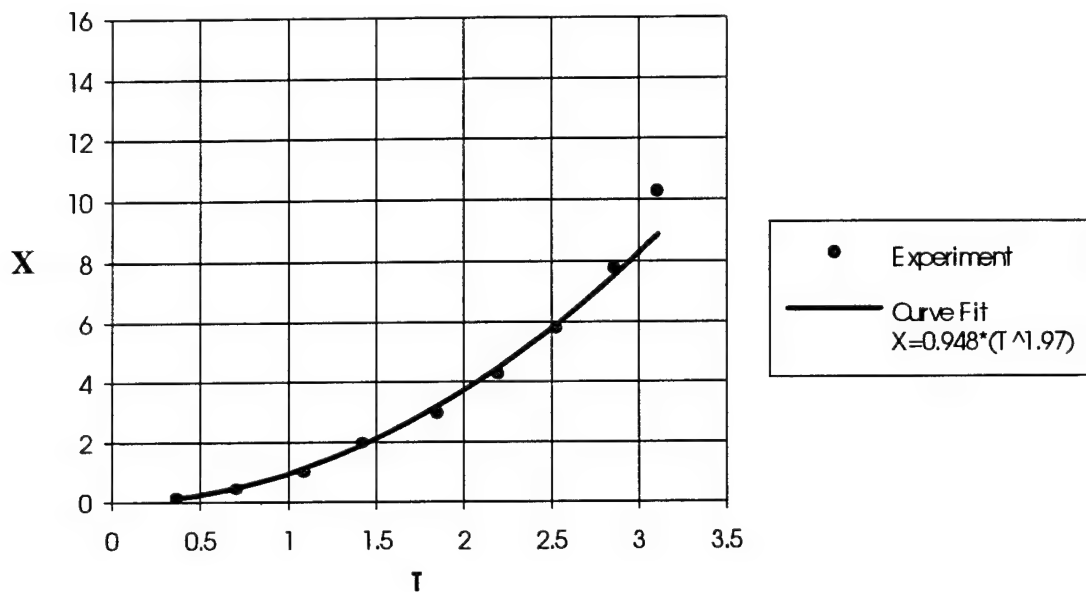
Test	Wave Type	Strength (%)	Duration (ms)	Diameter (mm)
7	S	65	infinite	1.41

Figure B.7. Dimensionless downstream displacement of a liquid jet for Test 7.



Test	Wave Type	Strength (%)	Duration (ms)	Diameter (mm)
8	S	38	infinite	1.04

Figure B.8. Dimensionless downstream displacement of a liquid jet for Test 8.



Test	Wave Type	Strength (%)	Duration (ms)	Diameter (mm)
9	S	254	infinite	1.04

Figure B.9. Dimensionless downstream displacement of a liquid jet for Test 9.

Appendix C: Weber - Reynolds Number Time History Plot

The Weber - Reynolds number time history for each test has been plotted in Figures C.1 - C.9. The following equations were used in determining these values:

Weber Number:
$$We = \frac{\rho_g V_g^2 D_j}{\sigma}$$

Reynolds Number:
$$Re = \frac{\rho_g V_g D_j}{\mu_g}$$

The gas velocity, V_g , and density, ρ_g , were obtained from the pressure time history plot and the standard shock tube relations.

The Weber Number characterizes the surface-tension effect. It is the ratio of the dynamic force of the gas to the surface-tension of the liquid. The Reynolds number is the ratio of the inertial force to the viscous forces of the gas.

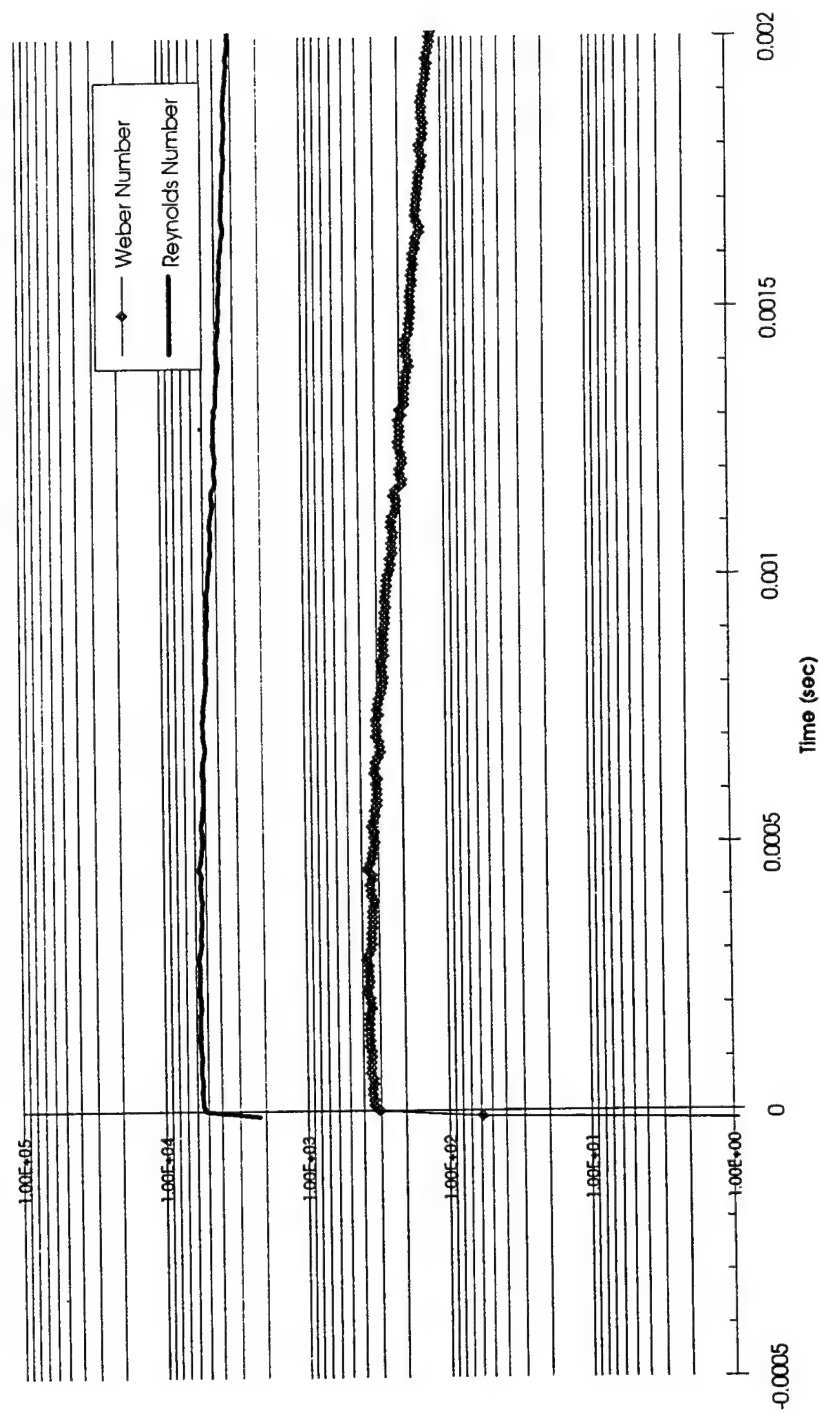


Figure C.1. Gaseous Weber and Reynolds Number Time History for Test 1

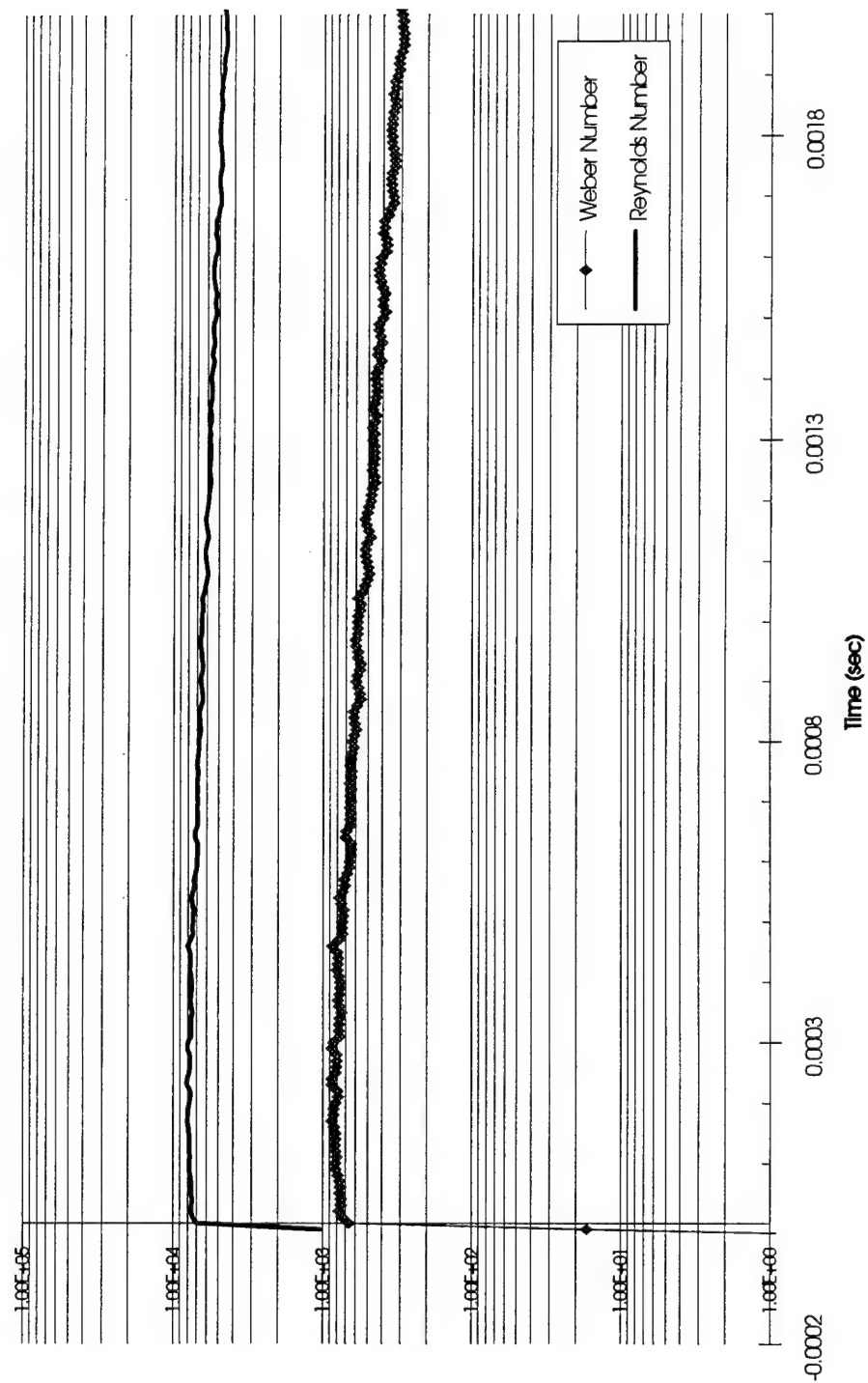


Figure C.2. Gaseous Weber and Reynolds Number Time History for Test 2

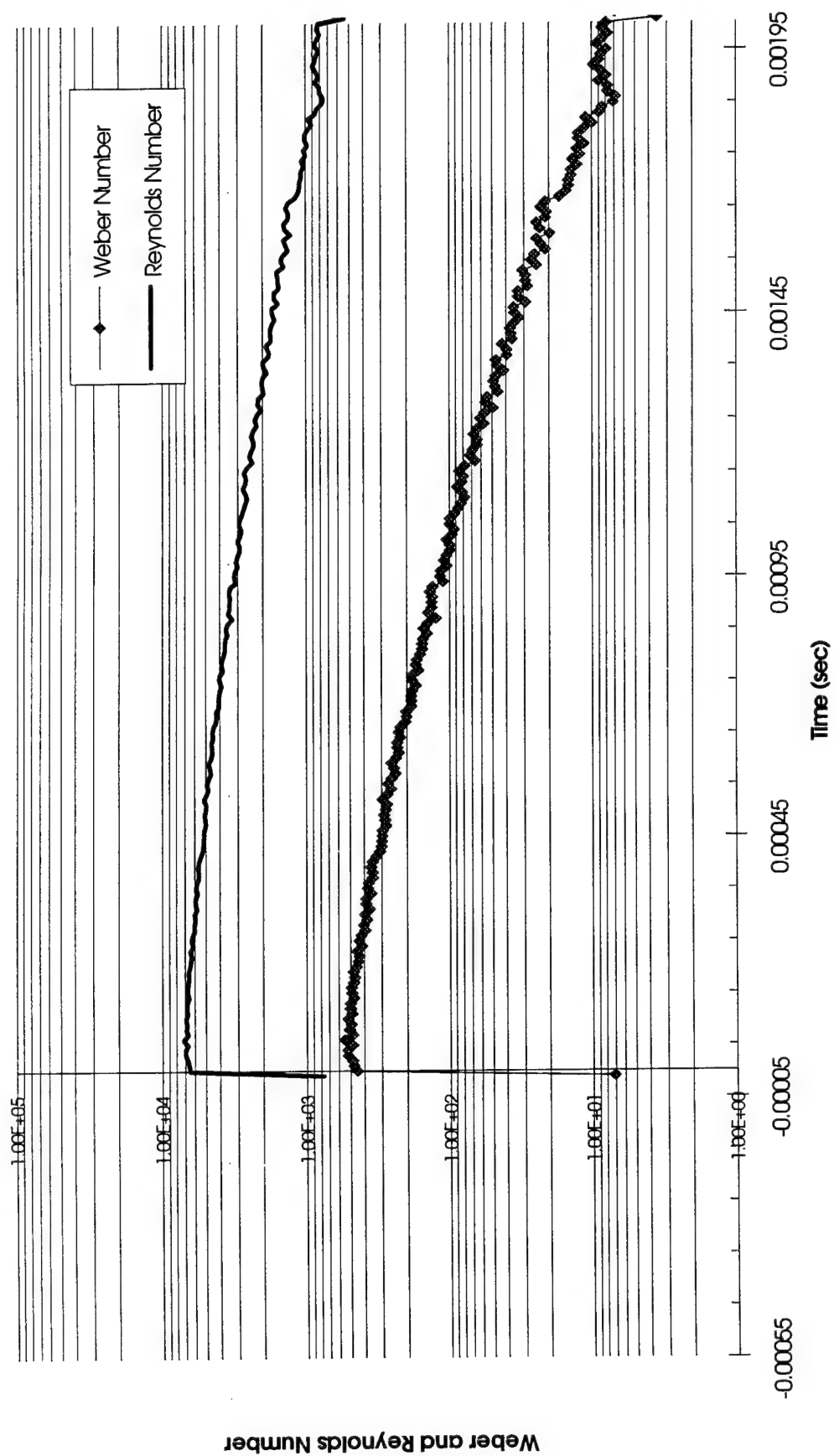


Figure C.3. Weber and Reynold Number Time History for Test 3

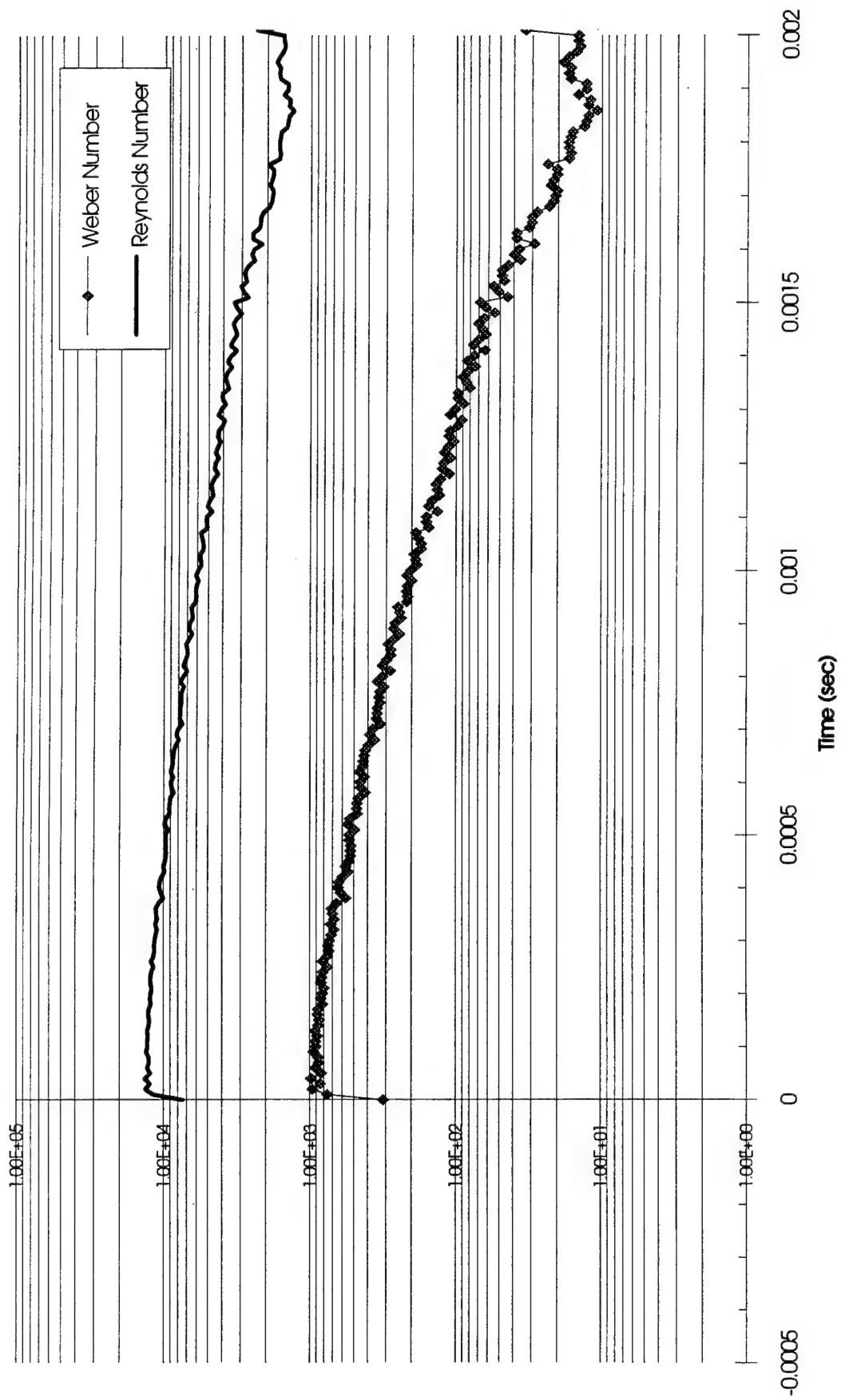


Figure C.4. Weber and Reynold Number Time History for Test 4

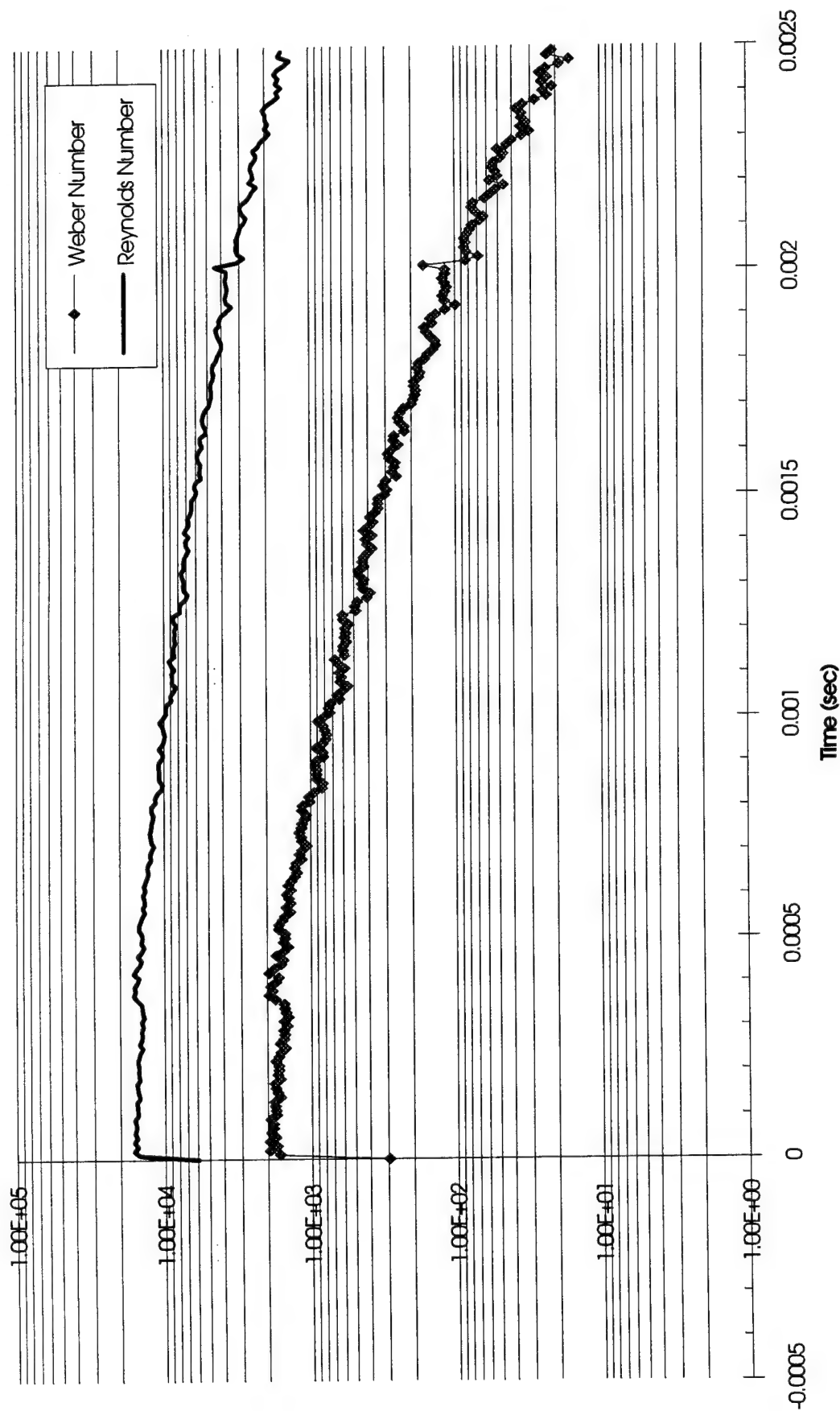


Figure C.5. Weber and Reynolds Number Time History for Test 5

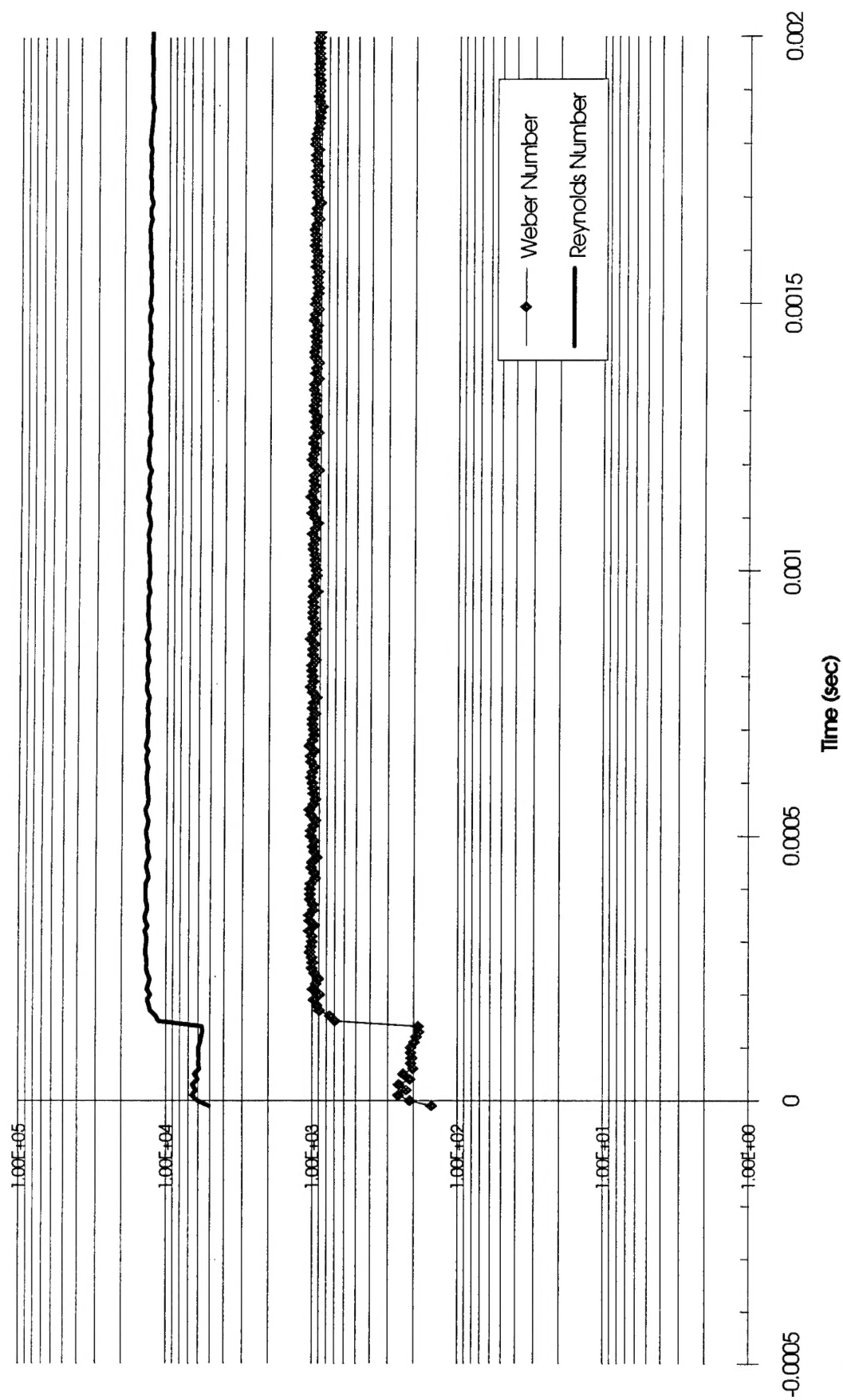


Figure C.6. Weber and Reynold Number Time History for Test 6

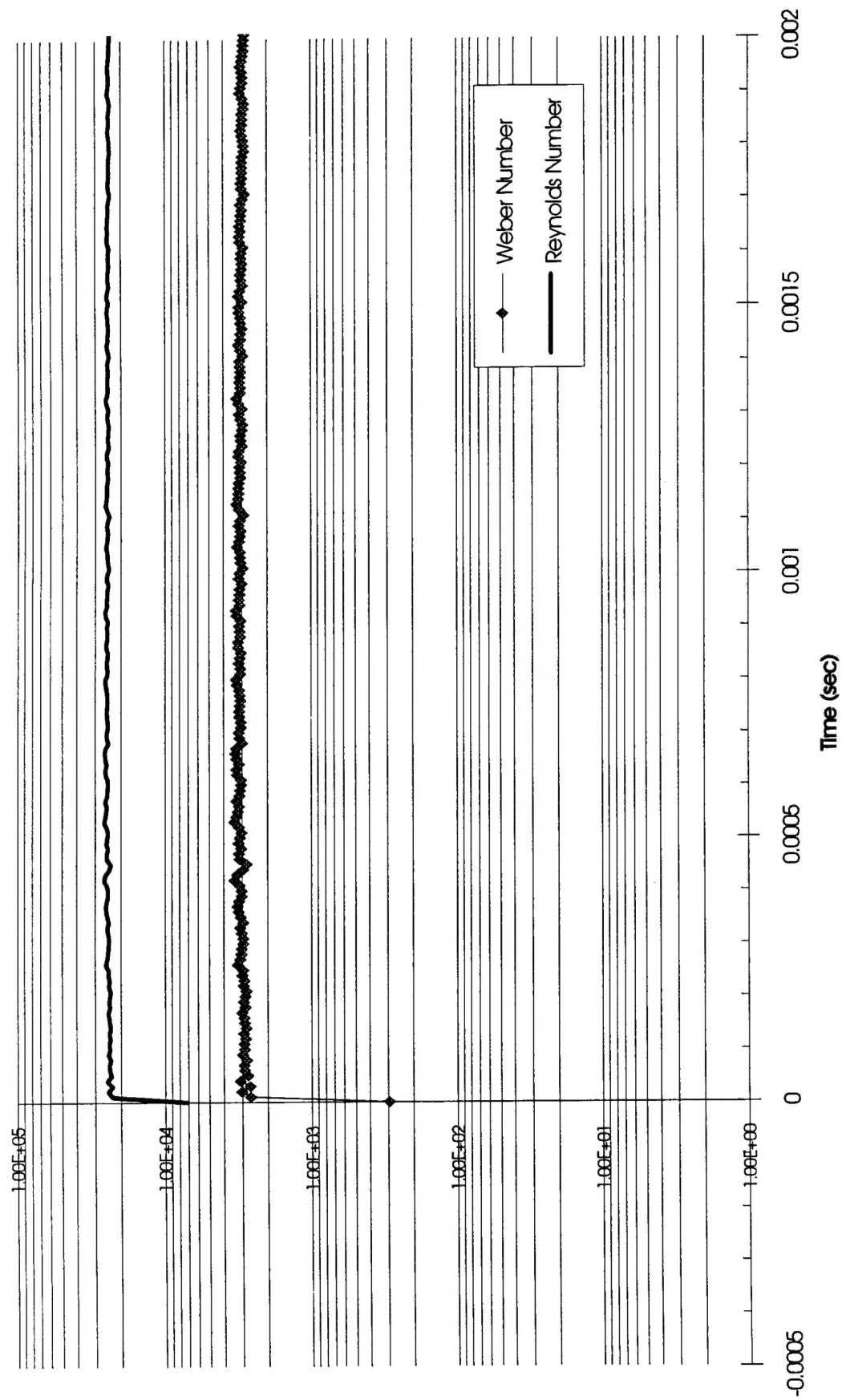


Figure C.7. Weber and Reynold Number Time History for Test 7



Figure C.8. Weber and Reynold Number Time History for Test 8

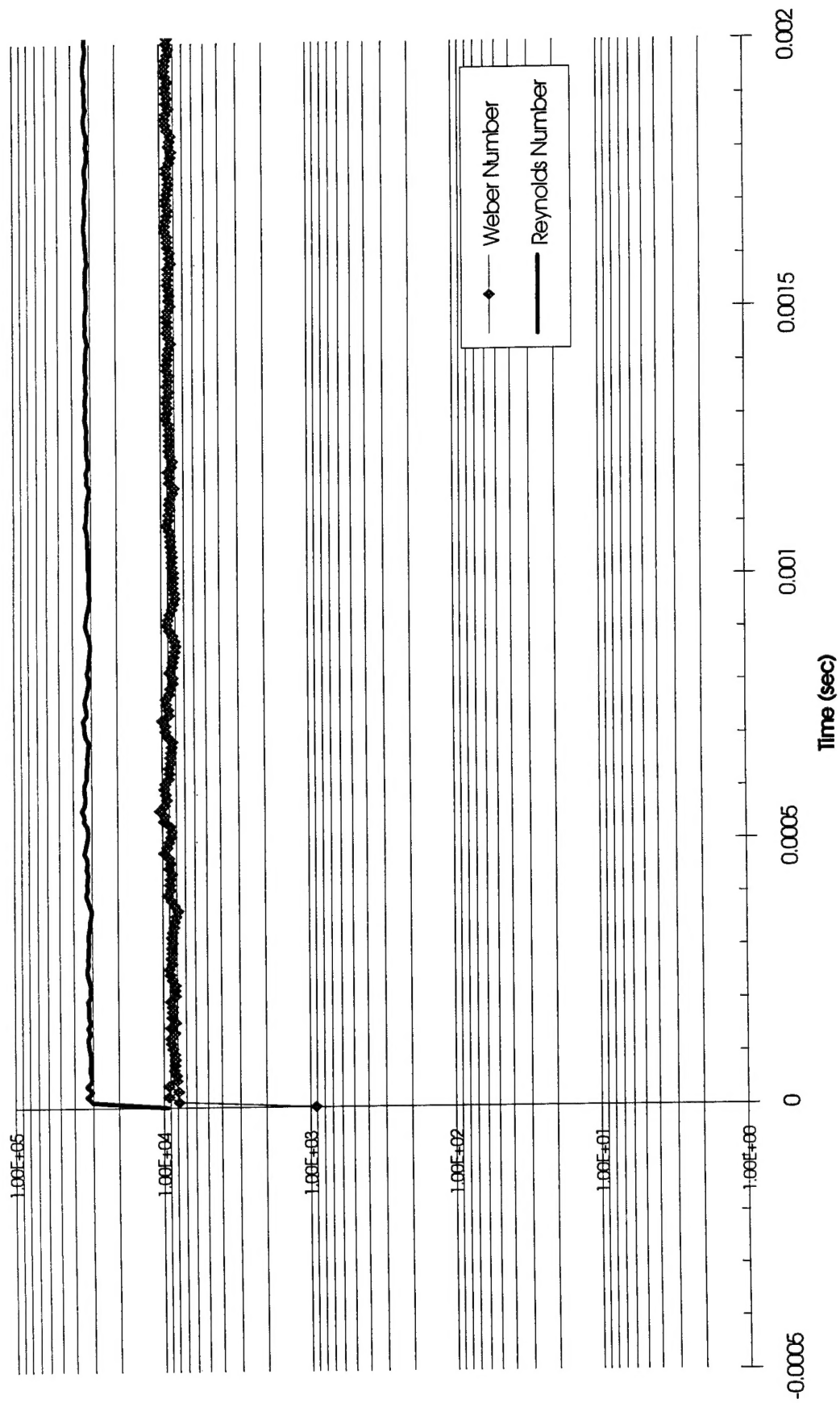


Figure C.9. Weber and Reynold Number Time History for Test 9